Neutrino-Electron Scattering in MINERνA for Constraining the NuMI Neutrino Flux

by

Jaewon Park

Submitted in Partial Fulfillment of the

Requirements for the Degree of

Doctor of Philosophy

Supervised by

Professor Kevin McFarland

Department of Physics and Astronomy

Arts, Sciences and Engineering

School of Arts and Sciences

University of Rochester

Rochester, New York

2013

Biographical Sketch

The author was born in Seoul, Korea. He attended Korea University at Seoul, and graduated with a Bachelor of Science degree in physics. He received a Master of Science degree from Korea University in 2003. He began doctoral studies in elementary particle physics at the University of Rochester in 2004. He received a master of arts from the University of Rochester in 2006. He started his research in MINERvA experiment under the supervision of Prof. Kevin McFarland. He has been involved in various stages of the experiment: detector R&D, construction, data taking, calibration, event reconstruction and data analysis.

Abstract

Neutrino-electron elastic scattering is used as a reference process to constrain the neutrino flux at the Main Injector (NuMI) beam observed by the MINERvA experiment. Prediction of the neutrino flux at accelerator experiments from other methods has a large uncertainty, and this uncertainty degrades measurements of neutrino oscillations and neutrino cross-sections. Neutrino-electron elastic scattering is a rare process, but its cross-section is precisely known. With a sample corresponding to 3.5×10^{20} protons on target in the NuMI low-energy neutrino beam, a sample of 120 $\nu e^- \rightarrow \nu e^-$ candidate events were observed with a predicted background of ≈ 30 events. This results in a flux constraint with 13% fractional precision, which is comparable to the uncertainty in other prediction methods. This technique will be more precise in MINERvA's upcoming higher statistics run in the NuMI medium energy beam and could be valuable for planned neutrino oscillation experiments.

Contributors and Funding Sources

Data for the studies in this thesis were gathered through the collective work of the MINERvA collaboration. Specific leading contributions to the calibration work described in Chapter 2 were performed by Brandon Eberly, Chris Marshall, Aaron McGowan, Aaron Mislivec and Clifford Simon. Key contributions to the reconstruction algorithms described in Chapter 4 were provided by Dr. Garbiel Perdue, Prof. David Schmitz and Ben Ziemer. The flux prediction, described in Chapter 3 and to which this result is compared in Chapter 6, was primarily performed by Leonidas Aliaga, Prof. Michael Kordosky and Dr. Melissa Jerkins. All other work not cited in the thesis was done by the student independently supervised on behalf of the University of Rochester and the MINERvA collaboration by Dr. Debroah Harris, Prof. Manly, Dr. Jorge Morfín, Prof. McFarland and Prof. Vittorio Paolone.

Dedicated to my wife, Hyejin Lim

Contents

List of Tables

List of Figures

Chapter 1

Introduction

1.1 Brief History

The neutrino was first proposed by Pauli to explain the electron energy spectrum of β-decay in 1930[1]. The electrically neutral and nearly massless particle was hypothesized to conserve energy and momentum in β-decay while interacting little with matter, rendering it almost *invisible*. Fermi made a theory for the β-decay process in analogy with electromagnetic interaction in 1932. In his theory, four fermions interact at a point without a propagator. At the energy of β decay, the propagator effect can be ignored. The existence of the neutrino was confirmed experimentally by Cowan and his colleagues using inverse β-decay in 1956 [**?**, **?**]. As the name implies, inverse β-decay, $\bar{\nu}_e p \rightarrow e^+ n$, is the reverse reaction of β-decay. Since the cross section of the weak interaction is very small, the experiment required a high intensity neutrino flux. Cowan and his colleagues used a nuclear reactor for the neutrino source. In order to detect the reaction, they used cadmium chloride ($CdCl_2$)

---

[1] Pauli originally called the particle the neutron, but later Fermi renamed it the neutrino.

in water, sandwiched between liquid scintillator detectors. In the measurement, the positron from the inverse β-decay reaction annihilates with an electron, producing a pair of back-to-back gammas. Since the positron annihilation is prompt, the gamma signal is detected quickly. The neutron formed in the reaction takes longer to be captured by cadmium. This delayed time coincidence was used to extract the rare inverse β-decay events from the background noise. The measured cross-section was consistent with Fermi's prediction.
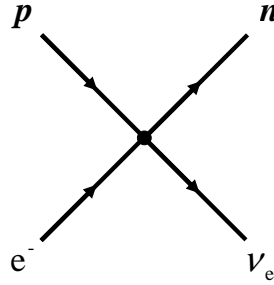
An important characteristic of the weak interaction is parity violation. In 1956, Lee and Yang worked to solve the so-called $\tau - \theta$ problem [**?**]. The problem was that two particles, known as the τ and θ, appeared to be identical but decayed in different parity modes. To conserve parity in the weak interaction, the τ and θ needed to be different particles. Otherwise, if they were identical particles with different decay modes, the weak interaction must violate parity. Lee and Yang searched for evidence of parity conservation for the weak interaction. They found much evidence of parity conservation for the electromagnetic and strong interactions but uncovered no experiments that tested parity conservation for the weak interaction. After Lee and Yang proposed several possible ways to test parity conservation in the weak interaction, Wu devised an experiment and observed parity violation in the weak interaction using the β-decay of polarized nuclei in 1957 [**?**]. In this experiment, Cobalt-60 decays into nickel-60 by beta decay, $^{60}_{27}\text{Co} \rightarrow {}^{60}_{28}\text{Ni} + \text{e}^- + \bar{\nu}_{\text{e}}$, while the spin of the cobalt-60 nucleus is aligned by an external magnetic field. An asymmetric angular distribution of the emitted electrons about the cobalt-60 spin direction was observed. In a parity transformation, the spin flips in the opposite direction, while the magnetic field orientation is unchanged, leading Wu to conclude from the observed asymmetric electron emission that parity is violated in the weak interaction.

In fact, the parity violation is maximal, i.e., all neutrinos are left-handed and all anti-neutrinos are right-handed. To accommodate parity violation, the theory of the weak interaction was modified, leading to what is known as V-A theory.

The anti-neutrino was found to be different from the neutrino. For example, the reaction, $\nu + n \to p + e^-$ was known to occur. If the anti-neutrino were identical to the neutrino, $\bar{\nu} + n \to p + e^-$ should happen as well. Davis and Harmer searched for such a reaction without success [?]. Additionally, having distinct neutrino and anti-neutrino states fit well with lepton number conservation. The observation that the process, $\mu \to e + \gamma$, does not exist indicates that the muon lepton number is a conserved quantity. If this is true, it follows naturally that the neutrino that is associated with a muon is distinct from the one that is associated with the electron.

In 1962, Lederman and his colleagues conducted an experiment to see if the anti-neutrinos created in association with muons in pion decay can interact and produce a positron. They found that this does not happen, i.e., the reaction $\bar{\nu}_\mu + p \to e^+ + n$ does not occur [?]. These muon neutrinos were seen to interact and produce only muons, implying that muon neutrinos and electron neutrinos are distinct.

In the 1960s, Salam, Glashow, and Weinberg proposed a unified theory of the electromagnetic and weak interactions. One key aspect of this electroweak theory is the existence of the so-called neutral current interaction. In 1973 the neutral current process $\bar{\nu}_\mu + e \to \bar{\nu}_\mu + e$ was observed by the Gargarmelle bubble chamber experiment[?]. Direct observations of the $W^\pm$, and Z^0 bosons, which are exchanged during charged current and neutral current interactions, respectively, were made in 1983 by the UA1 and UA2 experiments [?, ?, ?, ?] at SPS proton-antiproton collider.

Figure 1.1: β-decay point-interaction

1.2   Neutrino Interaction

All hadrons and leptons take part in the weak interaction but the effects are often hidden by overwhelming electromagnetic or strong interactions. Weak interactions are revealed when the electromagnetic or strong interactions are forbidden by a conservation law. β-decay was the first weak interaction studied. Fermi developed a theory to explain β-decay in a fashion analogous to the theory of the electromagnetic interaction. He proposed a different, weaker, coupling constant than that in electromagnetism. Fermi's theory was structurally similar to electromagnetism but lacked a momentum transfer dependence, meaning the theory involves a point interaction of four fermions as shown Fig. 1.1. Additionally, Fermi's theory allows the exchange of fermion charges, which is the origin of the term *charged current* interaction. The interaction amplitude for Fermi's point-interaction is given by Eqn. 1.1,

$$M = G_F \left(\bar{u}_p \gamma^\mu u_n \right) \left(\bar{u}_e \gamma_\mu u_\nu \right), \tag{1.1}$$

where G_F is Fermi constant, γ^μ is gamma matrix, and $u_p, u_n, u_e,$ and u_ν are wavefunctions for proton, neutron, electron and neutrino, respectively.

Fermi's theory did not explain parity violation. Modifications in his theory

	Symbol	Form	Effect under parity transformation
Scalar	S	$\bar{\psi}\psi$	$+P$
Pseudoscalar	P	$\bar{\psi}\gamma^5\psi$	$-P$
Vector	V	$\bar{\psi}\gamma^\mu\psi$	$+P$
Axial Vector	A	$\bar{\psi}\gamma^5\gamma^\mu\psi$	$-P$
Tensor	T	$\bar{\psi}\sigma^{\mu\nu}\psi$	
Vector - Axial vector	$V-A$	$\bar{\psi}\gamma^\mu(1-\gamma^5)\psi$	Maximal parity violation

$$\tag{1.4}$$

Table 1.1: Bilinear quantities and symbols

to accommodate the observed parity violation in the weak interaction led to the development of V-A theory. In V-A theory, Right-hand and left-hand projection operators are given by

$$P_R = \frac{1}{2}(1+\gamma^5) \tag{1.2}$$

$$P_L = \frac{1}{2}(1-\gamma^5). \tag{1.3}$$

Only left-handed neutrinos can take part in weak interactions. If a left-hand projection operation, $\frac{1}{2}(1-\gamma^5)$ is added in Eqn. 1.1, it becomes Eqn. 1.5. With this, the vertex factor γ^μ becomes $\gamma^\mu(1-\gamma^5)$. This, in fact, means that vector becomes vector minus axial vector (V-A). Table 1.4 shows various bilinear quantities and properties under parity transformation. The half-half mixture of odd parity vector and even-parity axial vector makes the V-A form violate parity maximally,

$$\mathcal{M}(p \rightarrow ne^+\nu_e) = \frac{G_F}{\sqrt{2}} \left[\bar{u}_n\gamma^\mu(1-\gamma^5)u_p \right] \left[\bar{u}_{\nu_e}\gamma^\mu(1-\gamma^5)u_e \right]. \tag{1.5}$$
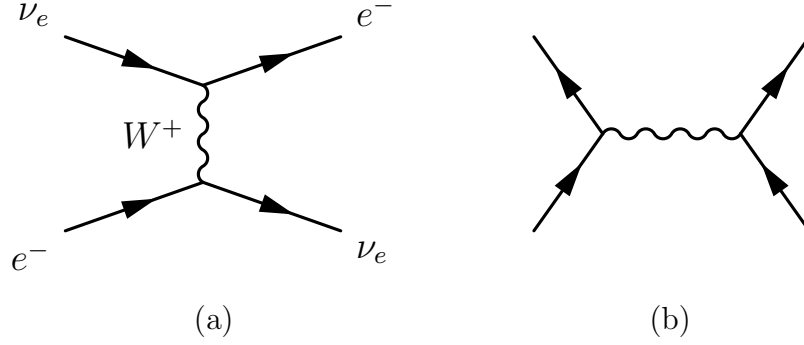
Figure 1.2: Electron neutrino – electron scattering diagrams, (a) $\nu_e e^- \to \nu_e e^-$, (b) $\bar{\nu}_e e^- \to \bar{\nu}_e e^-$

1.2.1   Helicity Structure

The interaction amplitude for $\nu_e e^- \to \nu_e e^-$ shown in Fig. 1.2 is given by

$$\mathcal{M}(\nu_\mu e^- \to \nu_\mu e^-) = \frac{G_F}{\sqrt{2}} \left[\bar{u}_{\nu_e}\gamma^\mu(1-\gamma^5)u_e\right]\left[\bar{u}_e\gamma_\mu(1-\gamma^5)u_{\nu_e}\right]. \tag{1.6}$$
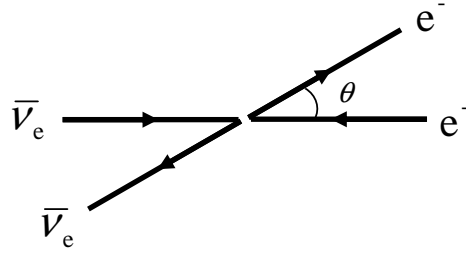
Integrating over spin states of the initial state and the final state results in

$$\frac{1}{2}\sum_{\text{spins}}|\mathcal{M}|^2 = 16G_F^2 s^2 \tag{1.7}$$

where s is one of Mandelstam variables $(s, t, \text{and } u)$. The angular distribution is isotropic.

$\bar{\nu}_e e^- \to \bar{\nu}_e e^-$ is a crossed reaction of $\nu_e e^- \to \nu_e e^-$. We can calculate the amplitude by replacing kinematic variable s with t,

$$\frac{1}{2}\sum_{\text{spins}}|\mathcal{M}(\bar{\nu}_e e^- \to \bar{\nu}_e e^-)|^2 = 4G_F^2 s^2(1-\cos\theta)^2 \tag{1.8}$$

Figure 1.3: Scattering angle θ of $\bar{\nu}_e e^- \to \bar{\nu}_e e^-$

where θ is defined as Fig. 1.3.

Eqn. 1.8 indicates that when θ is zero, the scattering amplitude goes to zero. This can be explained by a helicity argument. The anti-neutrino spin direction is the same as the propagation direction (right-handed), while the electron spin is opposite the propagation direction (left-handed), because the weak interaction couples only left-handed particles or right-handed anti-particles. Spin directions are the same; so the total spin is $+1$. Since the total spin direction will flip before and after scattering, spin is not conserved. Thus, back-to-back scattering is disfavored because of the helicity.

Another observation that is consistent with the V-A helicity structure of the weak interaction is that the total cross section for $\bar{\nu}_e e$ scattering is one third of $\nu_e e$ cross section,

$$\sigma(\bar{\nu}_e e^-) = \frac{1}{3}\sigma(\nu_e e^-).$$ (1.9)

1.2.2 Neutrino-Quark Scattering

Neutrino-quark scattering is similar to neutrino-lepton scattering in the high energy limit. Fig 1.4 shows the weak charged current interaction vertex with quarks. The
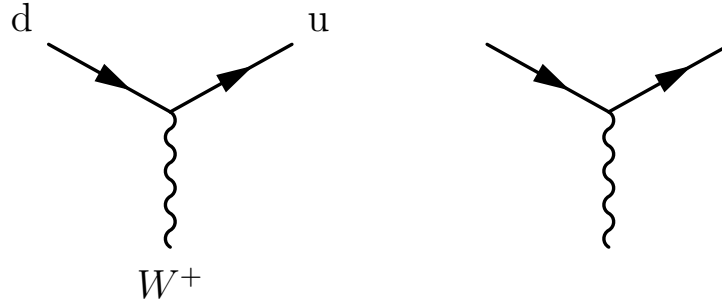
Figure 1.4: Charged current interactions with quarks

V-A structure of the weak interaction is also exhibited in neutrino-quark scattering,

$$J_q^\mu = \bar{u}_u \gamma^\mu (1 - \gamma^5) u_d \tag{1.10}$$

where J_q^μ is the charge-raising quark current. As in Eqn. 1.9, the cross section ratio of anti-neutrino quark scattering to neutrino quark scattering is one-third due to the helicity of the (anti-)neutrino,

$$\sigma(\bar{\nu}q) = \frac{1}{3}\sigma(\nu q). \tag{1.11}$$

Unlike what appears to happen in neutrino-lepton scattering, neutrino-quark scattering does not conserve quark number. During a charged current interaction with leptons, the lepton numbers, such as electron number or muon number, are conserved. When a neutrino is created, a pair of leptons from the same lepton family is always produced. On the other hand, weak interactions in the hadronic sector can transform particles from one family to another family. For example, strangeness is not conserved in the weak interaction. In order to explain non-conservation of strangeness, it is hypothesized that the charged current couples "rotated" quark states. Just like a weak interaction couples (ν_e, e^-) pair, it couples (u, d') or (c, s').

The mixing between families is parameterized by the Cabibbo angle (θ_c) as shown in Eqn. 1.12,

$$\begin{pmatrix} d' \\ s' \end{pmatrix} = \begin{pmatrix} \cos\theta_c & \sin\theta_c \\ -\sin\theta_c & \cos\theta_c \end{pmatrix} \begin{pmatrix} d \\ s \end{pmatrix}. \tag{1.12}$$

In this way, it is thought the weak interaction couples a (u, s) pair to the leptons in $K^+(u\bar{s}) \to \mu^+\nu_\mu$ in addition to the usual (u, d) pair coupling in $\pi^+(u\bar{d}) \to \mu^+ + \nu_\mu$. The small mixing angle ($\theta_c \approx 13°$) makes (u, s) coupling much smaller than (u, d) coupling. The Cabibbo angle formalism that describes two-family mixing in the quark sector is a subset of the more general three family quark mixing described by the 3×3 Cabibbo-Kobayashi-Maskawa (CKM) matrix.

1.2.3 Electro-Weak Theory

Initially the weak interaction looked like a different phenomenon from the electromagnetic interaction. The interaction strength is much smaller than that for the electromagnetic interaction, and that weakness is one of the defining characteristics for the weak interaction. But as the understanding of the weak interaction deepened, people wondered if one theory could explain both sets of phenomena. After all, a similar unification of electricity with magnetism was a major advance in our understanding of what seemed to be two separate phenomena, and that unification led to predictions and characterizations of important new physical things, such as light. Similarly, the unification of electromagnetic and weak interactions was more than aesthetics; it predicted the existence of the neutral current interaction and the heavy vector bosons ($W^\pm$ and Z^0) that mediate weak interactions. All of these things were all found experimentally later. The unifying framework for the electromagnetic and

weak interactions is called the electroweak interaction.

Before electroweak unification, the charged current interaction was the only known type of weak interaction. A charged current weak interaction either raises or lowers the electric charge of a particle through the interaction. In the case of a charged current interaction, the force is mediated by a charged vector bosons, $W^{\pm}$. Charge raising and lowering can be described in terms of a doublet made up of a charged lepton and its corresponding neutrino,

$$\chi_L = \begin{pmatrix} \nu_e \\ e^- \end{pmatrix}_L, \tag{1.13}$$

where L indicates left-handed.

The charge-raising and lowering currents are written as

$$J_\mu^+ = \bar{\chi}_L \gamma_\mu \tau_+ \chi_L = \bar{\nu}_L \gamma_\mu e_L \tag{1.14}$$

$$J_\mu^- = \bar{\chi}_L \gamma_\mu \tau_- \chi_L = \bar{e}_L \gamma_\mu \nu_L \tag{1.15}$$

where $\tau_{\pm}$ is defined as following

$$\tau_+ = \begin{pmatrix} 0 & 1 \\ 0 & 0 \end{pmatrix}, \qquad \tau_- = \begin{pmatrix} 0 & 0 \\ 1 & 0 \end{pmatrix}. \tag{1.16}$$

This resembles the SU(2) structure of a spin 1/2 system except for a missing third component. The so-called weak isospin current is given by

$$J_\mu^i = \bar{\chi}_L \gamma_\mu \frac{1}{2} \tau_i \chi_L \tag{1.17}$$

where the τ_i represent Pauli matrices. Charge raising or lowering current can be expressed in terms of J^1_μ and J^2_μ

$$J^\pm_\mu = J^1_\mu \pm i J^2_\mu. \tag{1.18}$$

The weak isospin triplet forms an $SU(2)$ group. The third component, J^3_μ, appeared to be a neutral current, possibly connected to neutral current weak interactions, but it has only a left-handed component. The inclusion of the electromagnetic interaction is done by adding an additional symmetry. Weak hypercharge is a generator of $U(1)_Y$ and is defined by

$$j^Y_\mu = 2(j^{\text{em}}_\mu - J^3_\mu). \tag{1.19}$$

The electroweak interaction is described by a symmetry group, $SU(2)_L \otimes U(1)_Y$.

The interaction itself occurs through an exchange of vector bosons. As the electromagnetic interaction is described by an electromagnetic current coupling to a vector potential, the electroweak interaction is described by the coupling of an electroweak current to vector boson fields

$$- ig \left(J^i \right)^\mu W^i_\mu - i\frac{g'}{2} \left(j^Y \right)^\mu B_\mu. \tag{1.20}$$

The vector bosons for charged current interactions are a mix of W^1 and W^2

$$W^\pm_\mu = \frac{1}{\sqrt{2}} \left(W^1_\mu \mp i W^2_\mu \right). \tag{1.21}$$

The mixing of W^3 and B produces the vector bosons for the electromagnetic and

weak neutral current interactions

$$A_\mu = B_\mu \cos\theta_W + W_\mu^3 \sin\theta_W \tag{1.22}$$

$$Z_\mu = -B_\mu \sin\theta_W + W_\mu^3 \cos\theta_W, \tag{1.23}$$

where θ_W is the weak mixing angle. If Eqn. 1.23 is plugged in Eqn. 1.20, the W^3 and B terms will be expressed in terms o $j_\mu^{\text{em}} A^\mu$ and $J_\mu^{\text{NC}} Z^\mu$. Since the electromagnetic vector field, A, couples only to charged leptons, if coefficients are solved for satisfying that condition, it leads to

$$g\sin\theta_W = g'\cos\theta_W = e. \tag{1.24}$$

The neutral current terms become $J_\mu^{\text{NC}} Z^\mu$, where J^{NC} is defined as

$$J_\mu^{\text{NC}} = J_\mu^3 - \sin^2\theta_W j_\mu^{\text{em}}. \tag{1.25}$$

In effective current-current interactions, i.e. low q^2, the propagator factor becomes $1/M_W^2$ or $1/M_Z^2$. From electroweak unification, the neutral current has an additional $1/\cos\theta_W$ as compared to the charged current. The relative strength between the charged current and neutral current, except for the $1/\cos^2\theta_W$ and propagator factor, is found to be the same experimentally. Then we obtain the W and Z mass relation, which is given by the weak mixing angle

$$M_W^2 = M_Z^2 \cos^2\theta_W. \tag{1.26}$$

Weak mixing only explains how the B_μ and W_μ^3 are mixed to make Z_μ and A_μ

(a)   (b)
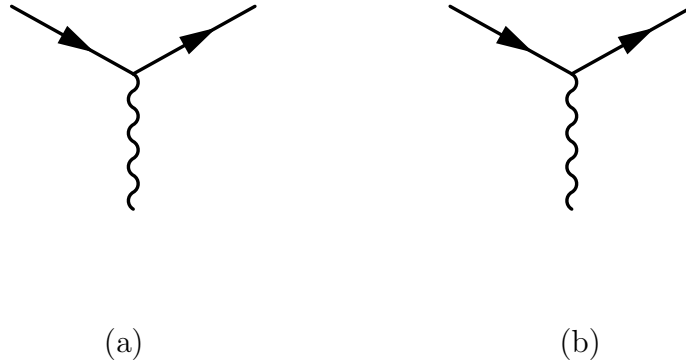
Figure 1.5: (a) Charged current interaction, (b) Neutral current interaction

(photon). It does not explain why the Z and W vector bosons are massive, while the photon is massless. Such asymmetric behavior is understood through the introdution of the Higgs field and spontaneous symmetry breaking.

1.2.4   Neutral Current Interactions

The neutral current does not change the charge of lepton while the charged current changes the charge of lepton as shown in Fig 1.5. Neutral current interactions are mediated by the Z^0 vector boson. Just as with the charged current interaction, the neutral current interaction can involve both leptons and quarks. In the t-channel, the incoming fermion is identical with the outgoing fermion in neutral current interactions. The vertex factor is given by

$$\frac{g_z}{2}\gamma^\mu(c_V^f - c_A^f\gamma^5), \tag{1.27}$$

where the vector (c_V^f) and axial-vector (c_A^f) factors depend on the fermion. Vertex factors are summarized in Table 1.2.

The neutral current factor originates from electroweak unification. The vertex

Fermion	c_V^f	c_A^f
ν_e, ν_μ, ν_τ	$\frac{1}{2}$	$\frac{1}{2}$
e^-, μ^-, τ^-	$-\frac{1}{2} + 2\sin^2\theta_W$	$-\frac{1}{2}$
u, c, t	$\frac{1}{2} - \frac{4}{3}\sin^2\theta_W$	$\frac{1}{2}$
d, s, b	$-\frac{1}{2} + \frac{2}{3}\sin^2\theta_W$	$-\frac{1}{2}$

(1.28)

Table 1.2: Neutral current factors

factors are from

$$c_V^f = T_f^3 - 2\sin^2\theta_W Q_f \tag{1.29}$$

$$c_A^f = T_f^3 \tag{1.30}$$

where T_f^2 the third component of weak isospin and Q_f is the charge of fermion f, their values are summarized in Table 1.3.

Fermion	Q_f	$(T_f^3)_L$
u, c, t	$\frac{2}{3}$	$\frac{1}{2}$
d, s, b	$-\frac{1}{3}$	$-\frac{1}{2}$
ν_e, ν_μ, ν_τ	0	0
e, μ, τ	-1	1
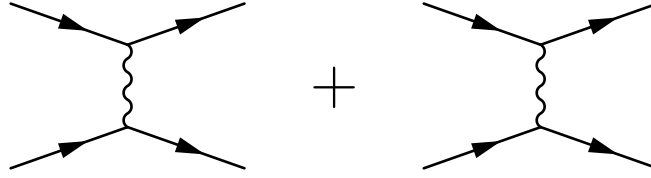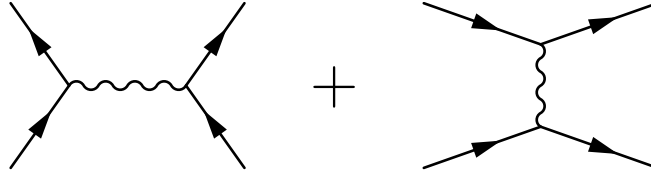
Table 1.3: Charges and weak isospins of fermions

Because neutral current interactions in the t-channel produce an invisible lepton final state, they are difficult to reconstruct experimentally. One exception is neutrino-electron scattering, which produces an electron final state. In fact, this was the first reaction that confirmed the neutral current interaction. It will be discussed more in the following section. In the s-channel, the Z vector boson can decay into a lepton - anti-lepton pair. In particular, the Drell-Yan process in hadron scattering permits the study of Z vector boson coupling to quarks and anti-quarks.

1.3 Neutrino-Electron Elastic Scattering

The process of neutrino-electron elastic scattering is understood well theoretically. The cross section is accurately known at the 1% level since it is a purely leptonic process. In this process, a neutrino scatters off on an atomic electron resulting in a neutrino and an electron in final state. The production of a single electron is the detectable signature in an experiment. One challenge of measuring the neutrino-electron scattering is that it has a very tiny cross section. Because center of mass energy is proportional to the target rest mass and the electron mass is ≈2000 times smaller than a nucleon mass, the neutrino-electron scattering cross section is ≈ 2000 times smaller than that for neutrino-nucleon scattering. The tiny cross section means that it is more difficult to separate the interesting interactions from the large number of background events. For the same reason, the momentum transfer is also very small, which makes the recoil electron very forward with respect to incident neutrino direction. The very forward angle of the electron provides a strong handle for separating the signal from the large background. Since the cross section of the reaction is well known, a measurement of the neutrino-electron rate can provide a measure of the neutrino flux.

All neutrino (and anti-neutrino) flavors undergo scattering with electrons. That is to say, all the processes $\nu_x e^- \to \nu_x e^-$ and $\bar{\nu}_x e^- \to \bar{\nu}_x e^-$ where $x = e, \mu$, and τ, can take place. Since the neutrino beam in the experiment discussed in this thesis is primarily a ν_μ beam with $\approx 1\%$ ν_e contamination, only $\nu_\mu e^- \to \nu_\mu e$ and $\nu_e e^- \to \nu_e e$ will be discussed. Muon neutrino and anti muon neutrino electron scattering ($\nu_\mu e^- \to \nu_\mu e^-$ and $\bar{\nu}_\mu e^- \to \bar{\nu}_\mu e^-$) can take part only in pure neutral current interaction via an exchange of Z boson as shown in Fig 1.6. The electron

Figure 1.6: Left: $\nu_\mu e$ scattering, Right: $\bar{\nu}_\mu e$ scattering

Figure 1.7: $\nu_e e$ scattering

Figure 1.8: $\bar{\nu}_e e$ scattering

neutrino and the anti-electron neutrino ($\nu_e e^- \rightarrow \nu_e e^-$ and $\bar{\nu}_e e^- \rightarrow \bar{\nu}_e e$) both exhibit scattering from electrons via neutral current and charged current interactions. The interaction amplitude will have both contributions and the corresponding interference term. The interference term can be ignored in the energy range of interest for this thesis ($\approx$1 - 10 GeV). Also, since the momentum transfer is much smaller than the mass of the propagator, the propagator effect can be ignored.
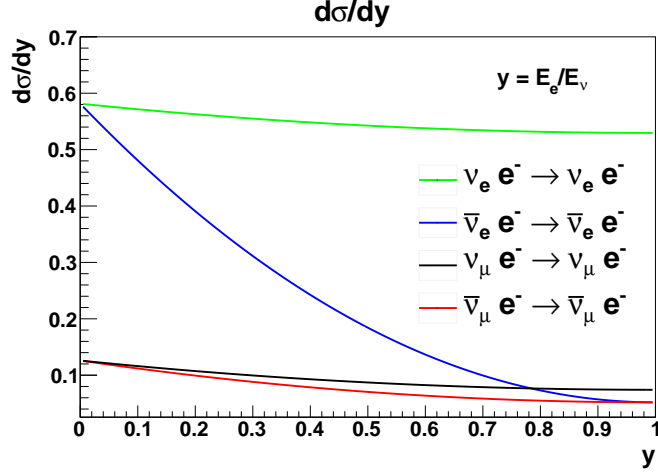
Figure 1.9: $\left(\frac{d\sigma}{dy}\right) / \left(\frac{G_F^2 s}{\pi}\right)$ is plotted for each neutrino flavor

Tree-level neutrino-electron scattering differential cross sections [**?**] are as follows:

$$\frac{d\sigma(\nu_\mu e \to \nu_\mu e)}{dy} = \frac{G_F^2 s}{\pi} \left[\left(\frac{1}{2} - \sin^2 \theta_W \right)^2 + \sin^4 \theta_W (1-y)^2 \right] \tag{1.31}$$

$$\frac{d\sigma(\bar{\nu}_\mu e \to \bar{\nu}_\mu e)}{dy} = \frac{G_F^2 s}{\pi} \left[\left(\frac{1}{2} - \sin^2 \theta_W \right)^2 (1-y)^2 + \sin^4 \theta_W \right] \tag{1.32}$$

$$\frac{d\sigma(\nu_e e \to \nu_e e)}{dy} = \frac{G_F^2 s}{\pi} \left[\left(\frac{1}{2} + \sin^2 \theta_W \right)^2 + \sin^4 \theta_W (1-y)^2 \right] \tag{1.33}$$

$$\frac{d\sigma(\bar{\nu}_e e \to \bar{\nu}_e e)}{dy} = \frac{G_F^2 s}{\pi} \left[\left(\frac{1}{2} + \sin^2 \theta_W \right)^2 (1-y)^2 + \sin^4 \theta_W \right] \tag{1.34}$$

where y is inelasticity, and $s \approx 2m_e E_\nu$. Both the Fermi constant and the weak mixing angle are accurately known. $\left(\frac{d\sigma}{dy}\right) / \left(\frac{G_F^2 s}{\pi}\right)$ is plotted for each neutrino flavor in Fig. 1.9.

The total cross section is obtained by integrating over y,

$$\sigma(\nu_\mu e \rightarrow \nu_\mu e) = \frac{2G_F^2 m_e E_\nu}{\pi} \left[\left(\frac{1}{2} - \sin^2 \theta_W \right)^2 + \frac{1}{3} \sin^4 \theta_W \right] \tag{1.35}$$

$$\sigma(\bar{\nu}_\mu e \rightarrow \bar{\nu}_\mu e) = \frac{2G_F^2 m_e E_\nu}{\pi} \left[\frac{1}{3} \left(\frac{1}{2} - \sin^2 \theta_W \right)^2 + \sin^4 \theta_W \right] \tag{1.36}$$

$$\sigma(\nu_e e \rightarrow \nu_e e) = \frac{2G_F^2 m_e E_\nu}{\pi} \left[\left(\frac{1}{2} + \sin^2 \theta_W \right)^2 + \frac{1}{3} \sin^4 \theta_W \right] \tag{1.37}$$

$$\sigma(\bar{\nu}_e e \rightarrow \bar{\nu}_e e) = \frac{2G_F^2 m_e E_\nu}{\pi} \left[\frac{1}{3} \left(\frac{1}{2} + \sin^2 \theta_W \right)^2 + \sin^4 \theta_W \right]. \tag{1.38}$$

Cross sections have only different constant factors in terms of weak mixing angle. Relative cross section size is shown in Table 1.4. $\sin^2 \theta_W = 0.2277$ is used for the calculation, which is GENIE [**?**]'s default value. $\nu_e e^-$ and $\bar{\nu}_e e^-$ scattering have larger cross section than $\nu_\mu e^-$ and $\bar{\nu}_\mu e^-$ because they have additional charged current contribution.

Reaction	$\sigma/(2G_F^2 m_e E_\nu/\pi)$	**Value** $(\sin^2 \theta_W = 0.2277)$	**Relative to** $\nu_\mu e \rightarrow \nu_\mu e$
$\nu_\mu e \rightarrow \nu_\mu e$	$\left(\frac{1}{2} - \sin^2 \theta_W \right)^2 + \frac{1}{3} \sin^4 \theta_W$	0.0914	1
$\bar{\nu}_\mu e \rightarrow \bar{\nu}_\mu e$	$\frac{1}{3} \left(\frac{1}{2} - \sin^2 \theta_W \right)^2 + \sin^4 \theta_W$	0.0766	0.837
$\nu_e e \rightarrow \nu_e e$	$\left(\frac{1}{2} + \sin^2 \theta_W \right)^2 + \frac{1}{3} \sin^4 \theta_W$	0.547	5.98
$\bar{\nu}_e e \rightarrow \bar{\nu}_e e$	$\frac{1}{3} \left(\frac{1}{2} + \sin^2 \theta_W \right)^2 + \sin^4 \theta_W$	0.228	2.5

Table 1.4: Relative sizes of total cross section for νe^- scattering

1.4 Neutrino Oscillations

Neutrinos are generated in association with a corresponding lepton as in $\pi^\pm$ decay $(\pi^+ \rightarrow \mu^+ + \nu_\mu$ and $\pi^- \rightarrow \mu^- + \bar{\nu}_\mu)$ and β-decay $(n \rightarrow p + e^- + \bar{\nu}_e)$. Consequently, the flavor of the produced neutrino is known for a given process. Then,

when the neutrino undergoes a charged current interaction, it produces a charged lepton, which reveals the flavor of the neutrino at the time of interaction. After traveling a short distance, the measured flavor of the neutrino is the same as the generated neutrino flavor. In fact, the neutrino flavor was considered a conserved quantity until Super Kamiokande [**?**] and other experiments [**?**, **?**] observed neutrino oscillations. A neutrino oscillates if it is created with a certain neutrino flavor and transforms into another neutrino flavor after traveling some (usually long) distance. Neutrino flavor is not a conserved quantity. In the Standard model, the neutrino is a massless particle. It is known experimentally that the neutrino is massless or nearly massless. The current upper limit on the mass of the electron anti-neutrino is about 2 eV from direct neutrino mass measurement experiments [**?**, **?**] using tritium beta decay. The existence of neutrino oscillations implies a non-zero neutrino mass. It necessitates a modification of the Standard model. Just the fact of non-zero mass or the existence of neutrino mixing is not enough to confirm a correct theoretical description for oscillations. In order to understand neutrino oscillations more fully, it is necessary to measure with high precision several parameters governing oscillations. The experimental effort responding to this challenge has been growing in recent years.

In analogy to the then known oscillation of K_L and K_S, Bruno Pontecorvo [**?**] suggested that neutrino oscillations can happen if neutrinos have non-zero masses and neutrino mass eigenstates are not identical with flavor eigenstates. The standard three flavor neutino mixing is described by a Pontecorvo-Maki-Nakagawa-Sakata (PMNS) matrix [**?**].

The basic idea of neutrino oscillations can be demonstrated with the simpler two flavor oscillation. Flavor eigenstates are rotated states relative to the mass

eigenstates. This rotation is given by a unitary matrix with one rotation angle parameter as shown in Eqn. 1.39,

$$
\begin{pmatrix} \nu_\alpha \\ \nu_\beta \end{pmatrix} = \begin{pmatrix} \cos\theta & \sin\theta \\ -\sin\theta & \cos\theta \end{pmatrix} \begin{pmatrix} \nu_1 \\ \nu_2 \end{pmatrix}.
\tag{1.39}
$$

In this picture, the time evolution of two energy eigenstates are described by

$$
|\nu_1(t)\rangle = e^{i(\vec{p_1}\cdot\vec{x} - E_1 t)}|\nu_1\rangle
\tag{1.40}
$$

$$
|\nu_2(t)\rangle = e^{i(\vec{p_2}\cdot\vec{x} - E_2 t)}|\nu_2\rangle.
\tag{1.41}
$$

In general, a neutrino beam is generated with certain flavor, ν_α, which is a super-position of the two mass eigenstates

$$
\nu_\alpha(t)\rangle = \cos\theta e^{i(\vec{p_1}\cdot\vec{x} - E_1 t)}|\nu_1\rangle + \sin\theta e^{i(\vec{p_2}\cdot\vec{x} - E_2 t)}|\nu_2\rangle.
\tag{1.42}
$$

When the ν_α propagates in space, the two mass eigenstates interfere and this interference results in the oscillation of the probability that a particle with initial flavor ν_α remains flavor ν_α after propagation.

The ν_α survival probability is calculated as follows:

$$
\begin{aligned}
P(\nu_\alpha \to \nu_\alpha) &= |\langle\nu_\alpha|\nu_\alpha(t)\rangle|^2 \tag{1.43}\\
&= 1 - \sin^2 2\theta \sin^2\left[\frac{(E_1 - E_2)t}{2} - \frac{(\vec{p_1} - \vec{p_2})\cdot\vec{x}}{2}\right]. \tag{1.44}
\end{aligned}
$$

If the same momentum is assumed, i.e., $p_1 = p_2$, the phase difference term, $(E_1 - E_2)/2$, characterizes the oscillation period. The mixing angle determines the oscillation amplitude in the form of $\sin^2 2\theta$. Even for MeV neutrinos, the neutrino is

highly relativistic because of its tiny mass. So the energy can be expanded in terms of m/p

$$E_1 = \sqrt{m_1^2 + p^2} \approx p + \frac{m_1^2}{2p} \tag{1.45}$$

$$E_2 = \sqrt{m_2^2 + p^2} \approx p + \frac{m_2^2}{2p} \tag{1.46}$$

$$E_1 - E_2 \approx \frac{m_1^2 - m_2^2}{2p} \approx \frac{m_1^2 - m_2^2}{2E}. \tag{1.47}$$

If Eqn. 1.47 is plugged in Eqn. 1.44,

$$P(\nu_\alpha \to \nu_\alpha) = 1 - \sin^2 2\theta \sin^2 \left[\frac{(m_1^2 - m_2^2)t}{4E} \right] \tag{1.48}$$

where t is replaced by travel distance, L. After units are included, the survival probability is

$$P(\nu_\alpha \to \nu_\alpha) = 1 - \sin^2 2\theta_{12} \sin^2 \left(1.267 \Delta m_{12}^2 \frac{L}{E} \right) \tag{1.49}$$

where θ_{12} is the mixing angle, $\Delta m_{12}^2 = m_1^2 - m_2^2$, L is distance, and E is neutrino energy. Eqn. 1.49 shows that the survival probability will oscillate. This oscillation is a result of the $\nu_\alpha \to \nu_\beta$ transition and vice versa. The survival probability oscillates between maximum 1 and minimum $1 - \sin^2 \theta_{12}$. For maximum mixing ($\theta_{12} = \pi/2$), the oscillation modulation will be maximum. If the mixing angle is small, the oscillation modulation becomes small and it is more difficult to see the effect of oscillations. The oscillation occurs as a function of L/E rather than depending on L and E separately. If the energy is fixed, the oscillations will happen as a function

of travel distance. First generation neutrino oscillation experiments are designed to look for the oscillation minimum, and are often called disappearance experiments. The first minimum happens at $1.267\Delta m_{12}^2 \frac{L}{E} = \frac{\pi}{2}$ or equivalently $\frac{L}{E} = \frac{\pi}{2 \times 1.267\Delta m_{12}^2}$. When $P(\nu_\alpha)$ is minimum, $P(\nu_\beta)$ is maximum. The probability of the neutrino appearing as flavor ν_β is simply $1 - P(\nu_\alpha)$. Experiments that measure the appearance of transformed neutrinos, such as ν_β in a beam of initial state ν_α neutrinos, are called appearance experiments. The frequency of oscillation is determined by the mass squared difference, $\Delta m_{12}^2 = m_1^2 - m_2^2$. A basic oscillation measurement as per Eqn. 1.49 only gives the mass squared difference, and it does not determine whether $\Delta m_{12}^2 > 0$ or $\Delta m_{12}^2 < 0$. Also, note that if $m_1 = m_2$, there are no oscillations. In other words, the mass eigenstates have to be non-degenerate in order for neutrino oscillation to occur. In either a disappearance or an appearance oscillation experiment, the oscillation modulation determines the mixing angle, and the oscillation maximum or minimum position, in terms of L/E, determines the mass squared difference.

So far, this discussion assumes neutrinos are propagating in vacuum. Neutrino oscillations in matter are somewhat different from those in vacuum. There is a so-called matter effect, or Mikheyev-Smirnov-Wolfenstein (MSW) effect. When a neutrino travels through matter, it experiences a potential due to coherent forward scattering. All neutrinos have coherent scattering by neutral current reaction as shown in Fig. 1.10 (b). Electron neutrinos have an additional contribution from neutrino-electron charged current scattering as shown in Fig. 1.10(a). Due to this additional contribution, electron neutrinos feel a different potential than other flavors of neutrinos. The additional potential experienced by electron neutrinos is

(a) (b)

Figure 1.10: Coherent forward scattering. (a) ν_e charged current interaction, (b) Neutral current interaction for all flavors

given by

$$V = \sqrt{2}G_F N_e \qquad (1.50)$$

where G_F is the Fermi constant and N_e is electron density in matter.

Consequently, oscillations in matter are modified by a flavor dependent potential. Modified oscillations can be expressed as oscillation with an effective mass squared difference and an effective mixing angle

$$\Delta m_{\text{eff}}^2 = \sqrt{(\Delta m^2 \cos 2\theta - 2EV)^2 + (\Delta m^2 \sin 2\theta)^2} \qquad (1.51)$$

$$\sin 2\theta_{\text{eff}} = \frac{\sin 2\theta}{\sqrt{\left(\cos 2\theta - \frac{2EV}{\Delta m^2}\right)^2 + \sin^2 2\theta,}} \qquad (1.52)$$

where V is the matter potential in Eqn. 1.50. The matter effect has a significant impact on solar neutrino oscillation when a neutrino travels through the Sun and the Earth.

Three flavor oscillations are described by a PMNS matrix. In this case, three

flavor eigenstates are related to mass eigenstates by a unitary matrix

$$
\begin{pmatrix} \nu_e \\ \nu_\mu \\ \nu_\tau \end{pmatrix} = \begin{pmatrix} U_{e1} & U_{e2} & U_{e3} \\ U_{\mu 1} & U_{\mu 2} & U_{\mu 3} \\ U_{\tau 1} & U_{\tau 2} & U_{\tau 3} \end{pmatrix} \begin{pmatrix} \nu_1 \\ \nu_2 \\ \nu_3 \end{pmatrix}.
\tag{1.53}
$$

A popular parameterization for three neutrino mixing is shown in Eqn. 1.54. It has three mixing angles and one CP-violation angle[2]

$$
U = \begin{pmatrix} 1 & 0 & 0 \\ 0 & c_{23} & s_{23} \\ 0 & -s_{23} & c_{23} \end{pmatrix} \begin{pmatrix} c_{13} & 0 & e^{i\delta} s_{13} \\ 0 & 0 & 0 \\ -e^{-i\delta} s_{13} & 0 & c_{13} \end{pmatrix} \begin{pmatrix} c_{12} & s_{12} & 0 \\ -s_{12} & c_{12} & 0 \\ 0 & 0 & 0 \end{pmatrix}.
\tag{1.54}
$$

where $c_{ij} = \cos\theta_{ij}$ and $s_{ij} = \sin\theta_{ij}$.

The PMNS matrix is reminiscent of the CKM matrix. Generally, at least three flavors are necessary to have CP-violation. If three flavor neutrino oscillations is the correct model for neutrino oscillation phenomena, then the measured three mixing angles $(\theta_{12}, \theta_{23}, \theta_{13})$ should satisfy the unitary condition and the three mass squared differences are not independent

$$
\Delta m_{21}^2 + \Delta m_{32}^2 = \Delta m_{31}^2.
\tag{1.55}
$$

Currently, there is a mass hierarchy problem in neutrino physics. From solar and atmospheric neutrino oscillations, it is known that $|\Delta m_{21}^2| \ll |\Delta m_{31}^2| \sim |\Delta m_{32}^2|$. This gives two possibilities: the normal hierarchy ($m_1 < m_2 \ll m_3$) and the inverted hierarchy ($m_3 \ll m_1 < m_2$). Neutrino oscillations in vacuum are not sensitive to

---

[2]Assuming neutrinos are Dirac particles

the sign of m_{31}^2. But the matter effect does provide sensitivity to the m_{31}^2 sign. The $\cos 2\theta - \frac{2EV}{\Delta m^2}$ term in Eqn. 1.51 is sensitive to the sign of m_{31}^2. In the presence of the matter effect, the effective mass squared difference will vary depending on the sign of m_{31}^2.

1.4.1 Measurements of Neutrino Oscillation

Neutrinos come from various sources: atmospheric, solar, accelerator, nuclear reactor, and supernova. Since the neutrino interaction cross section is very small, a large detector volume and long periods of collecting data are necessary, in general, to get sufficient statistics to make meaningful measurements. Also, detectors are usually located underground in order to reduce the cosmic ray background.

Davis used a radiochemical method to detect solar neutrinos [?]. In Davis' experiment, when a neutrino was absorbed by a chlorine nucleus, inverse beta decay $(\nu_e + {}^{37}\text{Cl} \rightarrow e^- + {}^{37}\text{Ar})$ produced a radioactive ${}^{37}\text{Ar}$ nucleus. The ${}^{37}\text{Ar}$ was separated chemically, and the amount of ${}^{37}\text{Ar}$ was determined from the radioactivity. The detector for Davis' experiment contained 615 tons of tetrachloroethylene (C_2Cl_4) and was located 1480 m underground at the Homestake mine. Only one third of predicted solar neutrino flux was measured by Davis. This was known as the solar neutrino problem and was also the first hint of neutrino oscillations. Later, SNO (Sudbury Neutrino Observatory) resolved the issue by not only measuring the electron neutrino flux from the sun, but also the flux from transformed or oscillated neutrinos (muon and tau neutrinos) [?]. SNO measured an electron neutrino flux consistent with Davis' measurements and a total flux ($\nu_e, \nu_\mu,$ and ν_τ) that agreed with the predicted solar neutrino flux. Thus, SNO proved that solar neutrinos oscillate without relying on the solar neutrino flux model. A reactor neutrino experiment, Kam-

LAND, confirmed the results from SNO by measuring the disappearance of electron anti-neutrinos produced in a number of reactors as a function of distance [**?**]. A global fit on neutrino oscillation parameters indicates that only a large mixing angle (LMA) [**?**] solution is consistent with combined result of oscillation experiments.

Atmospheric neutrinos are generated from cosmic rays colliding with nuclei in the upper atmosphere. The neutrino flux arising from the decay chain of $\pi^\pm$ produced in the collisions is expected to satisfy $(\nu_\mu + \bar{\nu}_\mu)/(\nu_e + \bar{\nu}_e) \sim 2$ [**?**]. Super Kamiokande (SK) is a large water Cherenkov detector, located 1000 m underground. The vast water tank of the detector is surrounded by PMTs to measure Cherenkov light. In the experiment, a charged current neutrino interaction produces a charged lepton with nearly the same direction as the incoming neutrino. The neutrino direction, as well as its energy, can be determined from the observed Cherenkov ring in the PMT array. Atmospheric neutrinos reach SK from all directions, including the opposite side of the Earth. The zenith angle of the incoming neutrino determines the distance that the neutrino has traveled to SK from the point where it is produced in an atmospheric particle shower. SK observed a muon neutrino flux deficiency with a zenith angle dependence while, simultaneously, observing the electron neutrino flux to be consistent with the unoscillated flux prediction [**?**]. The observed deficiency in upward-going muon neutrinos indicates that muon neutrinos oscillate to other flavor neutrinos (in this case, thought to be the tau neutrino) while traveling the long distance through the Earth to reach SK. The same $\nu_\mu - \nu_\tau$ oscillation (so-called atmospheric neutrino oscillation) was observed in the KEK to Kamioka (K2K) and, later, the MINOS accelerator neutrino oscillation experiments [**?**][**?**]. K2K used same SK detector with an accelerator neutrino beam. In this case the neutrinos traveled 250 km to reach SK. MINOS has a longer baseline and a higher neutrino

Experiment	Neutrino source	Dominant oscillation	L (km)	$\langle E \rangle$	$\approx L/E$ (km/GeV)
Super Kamiokande	Atmospheric	$\nu_\mu \rightarrow \nu_\tau$	≈ 10000	5 GeV	2000
SNO	Solar	$\nu_e \rightarrow \nu_\mu$	1.5×10^8	1 MeV	1×10^9
KamLAND	Reactor	$\bar{\nu}_e \rightarrow \bar{\nu}_\mu$	180	4 MeV	45000
Daya Bay	Reactor	$\bar{\nu}_e \rightarrow \bar{\nu}_\tau$	≈ 2	4 MeV	500
K2K	Accelerator	$\nu_\mu \rightarrow \nu_\tau$	250	1 GeV	250
T2K	Accelerator	$\nu_\mu \rightarrow \nu_\tau$	295	0.7 GeV	400
MINOS	Accelerator	$\nu_\mu \rightarrow \nu_\tau$	735	3 GeV	250

Table 1.5: Neutrino oscillation experiments

energy so that L/E is similar to K2K. Many major neutrino oscillation experiments are summarized in Table 1.5. Neutrino oscillations were firmly established by the experiments described above, and two neutrino mixing angles, θ_{12} and θ_{23}, were measured. θ_{31} was an unknown parameter until Daya Bay measured it using reactor neutrinos [?]. The Daya Bay result was confirmed by RENO [?]. Daya Bay's $\bar{\nu}_e$ disappearance measurement at short baseline (~ 2 km) is shown in Fig. 1.12. The observed θ_{31} was found to be on the high end of the range allowed by previous measurements, meaning that future searches for CP violation in the neutrino sector are practical.

Various oscillation experiments are working to improve our knowledge of the oscillation parameters. Recent muon disappearance oscillation results from MINOS and T2K are shown in Fig. 1.11. Table 1.6 shows neutrino oscillation parameters from the global fit using various neutrino oscillation experiment measurements.

With the observation of neutrino oscillations, the next goals are to resolve the mass hierarchy problem and θ_{23} degeneracy (see below) and search for leptonic CP-violation. Probing these questions necessitates precision measurements of the oscillation parameters.
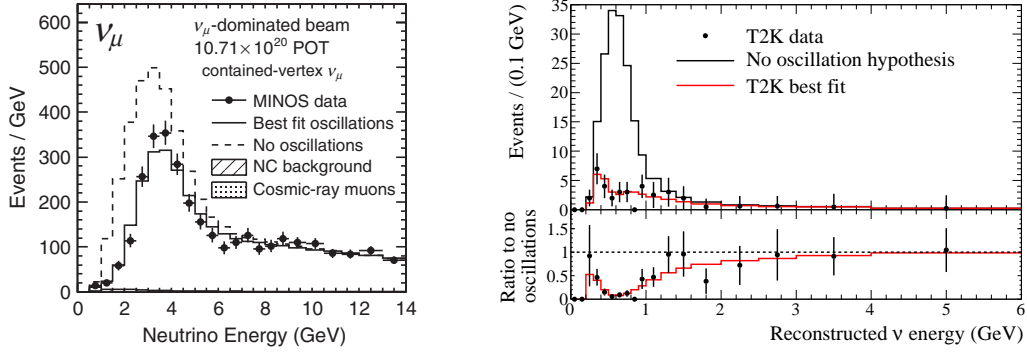
Figure 1.11: Left: MINOS ν_μ disappearance (Figure taken from [?]), Right: T2K ν_μ disappearance (Figure taken from [?])
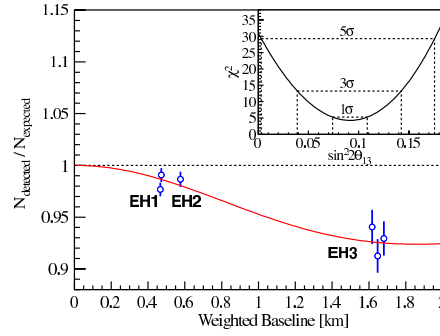
Figure 1.12: Daya Bay $\bar{\nu}_e$ disappearance (Figure taken from [?])

Parameter	best-fit $(\pm 1\sigma)$
$m_{21}^2(10^{-5}\text{eV}^2)$	$7.58^{+0.22}_{-0.26}$
$\lvert m_{32}^2\rvert(10^{-3}\text{eV}^2)$	$2.35^{+0.12}_{-0.09}$
$\sin^2\theta_{12}$	$0.306^{+0.018}_{-0.015}$
$\sin^2\theta_{23}$	$0.42^{+0.08}_{-0.03}$
$\sin^2\theta_{13}$	0.0251 ± 0.0034

Table 1.6: Oscillation parameters from the global fit. (2012 PDG values [?])

Determining mass hierarchy is important to get the correct picture of neutrino mixing. The mass hierarchy has an impact on neutrinoless double beta decay [**?**]. The current best θ_{23} measurement is from ν_μ disappearance, whose amplitude is given by $\sin^2 2\theta_{23}$, where the value is about 0.9. So, θ_{23} is close to $\pi/4$, which means ν_2 and ν_3 mixing is nearly maximal. But with the current error on the measurement, it is not certain whether or not the value of θ_{23} is exactly $\pi/4$. If the mixing is maximal, it would indicate a certain symmetry in neutrino mixing. If it is not maximal, θ_{23} has a degeneracy because $\theta_{23} = \pi/4 \pm \alpha$ gives the same $\sin^2 2\theta_{23}$. Such a degeneracy can be resolved in a ν_e appearance experiment, where the appearance probability has a $\sin^2 \theta_{23}$ dependence

$$\mathrm{P}(\nu_\mu \rightarrow \nu_e) \approx \sin^2 \theta_{23} \sin^2 2\theta_{13} \sin^2 \left(1.267\Delta m^2_{13}\frac{L}{E}\right). \tag{1.56}$$

CP violation in the lepton sector is of great interest. CP violation has been observed in the quark sector and it is important to see if it exists in the lepton sector as well. CP violation in the lepton sector might lead to a possible explanation for the matter-antimatter asymmetry in the universe [**?**]. CP, T, and CPT transformations in ν_μ–ν_e oscillation are shown in Fig. 1.13. CP violation is equivalent to T violation when CPT conservation is assumed. CP violation in the vacuum is given by

$$|P(\nu_\alpha \rightarrow \nu_\beta) - P(\bar{\nu}_\alpha \rightarrow \bar{\nu}_\beta)| \propto \sin\delta. \tag{1.57}$$

Observation of CP violation will be much harder if the CP violation angle, δ, is small.

The use of higher intensity beams and bigger detectors with longer periods of data taking will provide increased statistics that can be used for neutrino oscillation
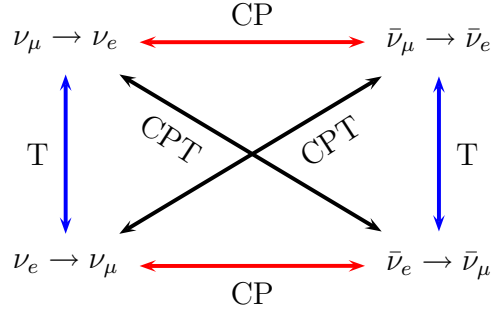
Figure 1.13: CP, T, and CPT transformation

measurements. With the increased statistics, systematic uncertainties become driving factors on uncertainties on measurement of oscillation parameters. The major systematic uncertainties in these experiments are the knowledge of the neutrino flux, cross-sections, and understanding the background reactions.

1.4.2 Neutrino Cross-sections

In long baseline neutrino oscillation experiments, a 0.5–10 GeV muon neutrino beam is used typically. In order to measure neutrino oscillations, the neutrino flux (and energy spectrum) is measured at large distance away from the neutrino beam source. For a disappearance experiment, for example, the measured flux will be less than the expected unoscillated flux. In order to measure the flux, the neutrinos have to interact with the matter that makes up the detector. The interactions are mainly neutrino-nucleon interaction. The cross section landscape is complex, as different reactions play a role depending on neutrino energy. Fig. 1.14 shows the charged current total cross-section along with the contribution from different processes. At high energies, deep inelastic scattering (DIS) is the dominant process. Fortunately, the DIS process cross section is well known, as it is essentially neutrino-quark (parton)
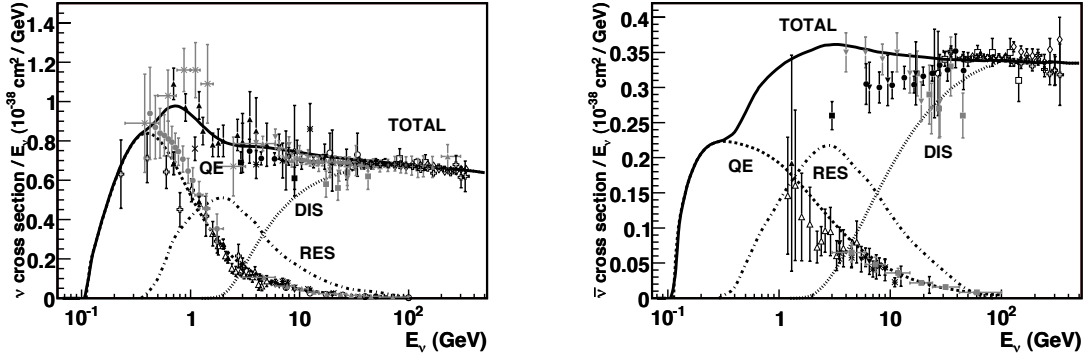
Figure 1.14: Charged current total cross-section with different process constributions (QE: Quasi-elastic, RES: resonance, DIS: deep inelastic scattering). Left: neutrino, Right: anti-neutrino. Solid line indicates NUANCE (event generator) prediction. Figure taken from [**?**]

scattering. Measurements of neutrino DIS has helped provide insight into the quark structure inside the nucleon. DIS interactions are often complex because many particles besides the muon track are usually present. Still, the DIS kinematics are well described by a muon and a recoiling system of hadrons.

At low energy, around 1 GeV, the dominant process is charged current quasi-elastic (CCQE) scattering, shown in Fig. 1.15. In CCQE interactions, the incident neutrino energy can be reconstructed from the muon using the 2-body kinematics of elastic scattering. This is the technique used in SK to reconstruct the neutrino energy. The recoil proton energy is below the Cherenkov threshold[3].

The transition region between low and high energy regimes discussed above is complex, as the processes of CCQE, resonance reaction, coherent pion production, and DIS all occur. Most of the cross-section data in this energy region is from old bubble chamber experiments in the 70's, and the cross sections are poorly measured.

Another complication in all of these energy regimes is the fact that in most of

---

[3]1.4 GeV for proton. Cherenkov threshold is given by $\beta > \frac{1}{n}$ where n is refractive index.
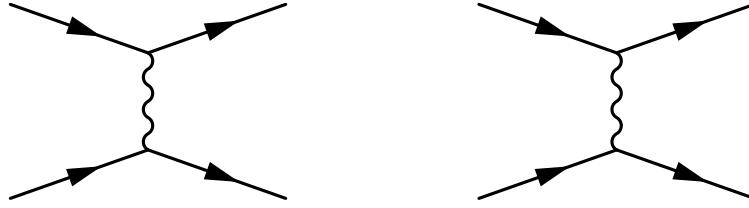
Figure 1.15: ν_μ CCQE reactions, Left: $\nu_\mu + n \rightarrow \mu^- + p$ scattering, Right: $\bar{\nu}_\mu + p \rightarrow \mu^+ + n$ scattering

the experiments, interactions occur on nuclei and nuclear effects are important. In addition the nuclear target dependence of the cross-section is important. Final state interactions (FSI) inside the nucleus can alter the final state. For example, the recoil proton in CCQE may interact with nuclear medium in the nucleus and knock out an extra hadron.

The measurement of neutrino-nucleon scattering cross sections in the 1–10 GeV region is the major goal of the MINERvA experiment. Improved cross section measurements and a better understanding of the details of background interactions are expected to reduce systematic errors in oscillation experiments.

1.4.3   Neutrino Flux

Solar and atmospheric neutrinos are available in nature but they are either low in energy or low in intensity or both. Since the neutrino interaction rate is proportional to both neutrino energy and intensity, the event rate in solar and atmospheric oscillation experiments is quite low. Nuclear reactors provide a high intensity source of low energy neutrinos, but the neutrino energy is not controllable.

Accelerator neutrino beams are controllable in both energy and intensity, in

principle. The conventional way to generate an accelerator-based neutrino beam is to strike a target with an energetic proton beam. This produces secondary hadron particles which undergo subsequent decays that produce neutrinos. One of the main decay channels is $p + (\text{target}) \rightarrow \pi^+$, then $\pi^+ \rightarrow \mu^+ + \nu_\mu$. Since the hadrons are produced over a wide range of angles, magnetic horns are used to focus the charged hadrons toward the neutrino detector(s). This focusing increases the neutrino flux. Because the neutrino beam is generated from decays that happen in a sizable decay pipe, the transverse size of the produced neutrino beam is about the same as the decay pipe. The energy spectrum of the produced neutrino beam is quite broad in general. Since neutrinos are electrically neutral, once generated, they are difficult to control or monitor directly. Experimental parameters that adjust the characteristics of the beam are things like the primary proton energy and the current and position of the magnetic horns. The neutrino spectrum has to be predicted by simulation. Generally, the flux prediction has large uncertainties (15-20%) due to poor knowledge of the hadron production.

To improve the knowledge of hadron production in neutrino beams, measurements of hadron production on external targets are used to tune the simulation. MIPP [**?**] and NA49/SHINE [**?**, **?**] are two such external hadron production experiments that were performed for this purpose. T2K [**?**] and MINOS use external data from these experiments to tune hadron production in their beamline simulation. MINERvA also utilizes NA49 data to tune NuMI beamline simulation.

Long baseline oscillation experiments often also use near detectors to measure the flux near the neutrino source. This measured, unoscillated, flux is used to normalize the flux in the far detector. If the detector technologies are different in the near and far detectors, the nuclear dependence of the cross section introduces systematic error

in the flux normalization. Even if the detector technology is identical in the near and far detectors, the flux in the near detector is not identical with the far detector. The near detector sees the neutrino beam angle spread from the sizable decay pipe, while the far detector only sees a point-like source. The neutrino spectrum is different depending on beam angle due to the kinematics of pion decay.

Since muons and kaons present in the secondary hadrons also can decay into electron neutrinos, ν_μ beams typically have about 1% ν_e contamination. This creates an irreducible background for ν_e appearance experiments.

1.4.4 Implication for Oscillation Experiments

Flux constraining measurements using neutrino-electron scattering, described in Section 1.3, can help to reduce the flux systematic uncertainties in the absolute cross-section measurements in the MINERvA experiment. In addition, this technique can be used in future long baseline oscillation experiments to provide an additional, independent constraint on the flux and help the effort to achieve precision measurements of the oscillation parameters.

Chapter 2

MINERvA Experiment

2.1 NuMI Beamline

The NuMI beamline consists of the hadron production target, a horn focusing system, the decay pipe, the hadron absorber, muon shielding, and neutrino beam monitoring [?]. The MINERvA detector is located roughly 1 km from target.

A 120 GeV proton beam from the Main Injector strikes a long, narrow graphite target [?]. Proton nucleus interactions produce unstable secondary particles, such as $\pi^\pm$ and $K^\pm$. Muon neutrinos are produced mainly from decays of $\pi^\pm$.

The charged hadrons, $\pi^\pm$ and $K^\pm$ are focused by a set of magnetic horns. A magnetic horn is a toroid with elliptical inner boundary. The distance between the target and the horns and distance between the two magnetic horns are tunable to select neutrino beams with different peak energies. Focused $\pi^\pm$ and $K^\pm$ travel through a helium-filled decay pipe 675 m in length[1]. π^+ decays primarily to a pair of anti-muon and muon neutrinos. The neutrino beam contains small fraction of ν_e,

---

[1] The $\pi^\pm$ life-time, τ is 2.6 $\times 10^{-8}$ s. Thus the mean travel length before decay is $\gamma c\tau = 558$ m for 10 GeV pions

which is mainly produced by decays of $\mu^{\pm}$, $K^{\pm}$ and K_L^0. At the end of the decay pipe is located a hadron absorber pile. Undecayed and stable hadronic particles are absorbed by a series of metal blocks and concrete blocks. Muons typically penetrate the hadron absorber and are eliminated by roughly 240 m of unexcavated rock after the absorber. When the remaining neutrinos are traveling through the rock before they reach the MINERvA detector in NuMI detector hall, particles are generated from the neutrino interactions in the rock that may also reach the detector. Muons that are generated from the neutrino interactions in this manner make up most of the particles observed in the detector and are called "rock muons".

2.1.1   Main Injector

The Main Injector was added to the Fermilab accelerator complex to provide proton beam to NuMI beamline and other fixed target experiments and to increase anti-proton production for the Tevatron proton-antiproton collider before its shutdown in 2011. The Main Injector is located next to the Tevatron ring as shown in Fig. 2.1.

In order to generate the 120 GeV proton beam in the Main Injector, multiple stages of accelerators are necessary prior to the Main Injector. First, hydrogen ions (H^-) are accelerated in the strong electrostatic field of a Cockcroft-Walton accelerator. Next, the Linac, a linear accelerator, accelerates the H^- to 400 MeV. When the accelerated H^- beam passes through a carbon foil, electrons are stripped off from the H^-. The positively charged hydrogen ions (protons) are injected into the Booster synchrotron, which accelerates the protons to 8 GeV. Proton batches in the Booster are injected to the Main Injector where they circulate counterclockwise.
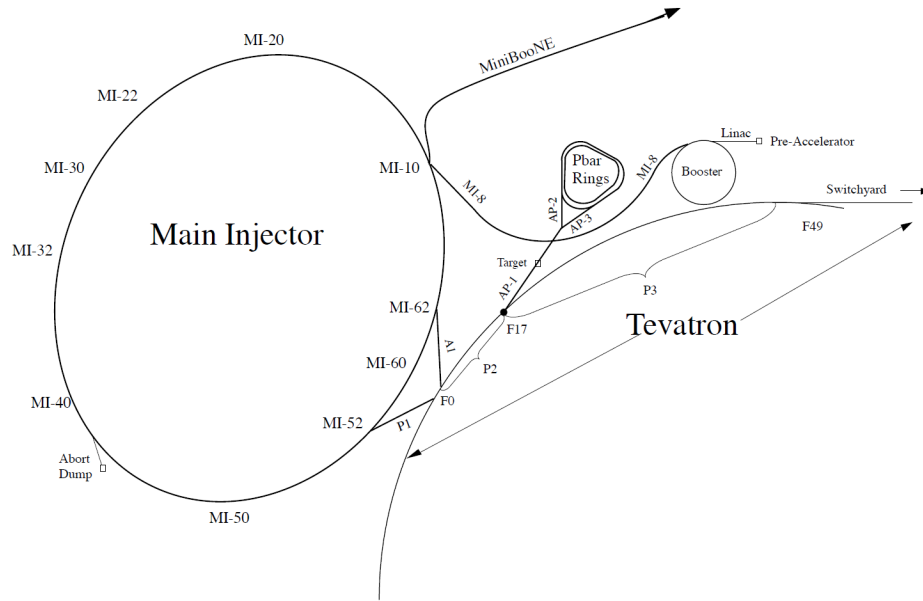
Figure 2.1: Main Injector

One Booster batch consists of 84 bunches[2] which fill the 474.2 m circumference of the Booster [?]. The larger circumference Main Injector can accept nominally 6 batches from the Booster. The Main Injector also provides an accelerated proton beam to the anti-proton production ring for Tevatron use. One of the 6 batches is slip-stacked[3] to provide a more intense beam for anti-proton production with a intensity of 1.5 times that of a normal batch [?]. The same technique is planned to be used for the NuMI beamline in the future [?]. The Main Injector ramps up the beam energy to 120 GeV using a radio frequency (RF) system in $\approx$ 1 second. Then, it sends the beam to the NuMI beamline by fast extraction, which produces 8.6 μsec spill duration. The cycle of injection from the Booster, acceleration and extraction

---

[2]The extraction RF frequency of Booster is 52.81 MHz which determins the spacing between adjacent bunches

[3]Two batches are injected in same batch slot and then merged.
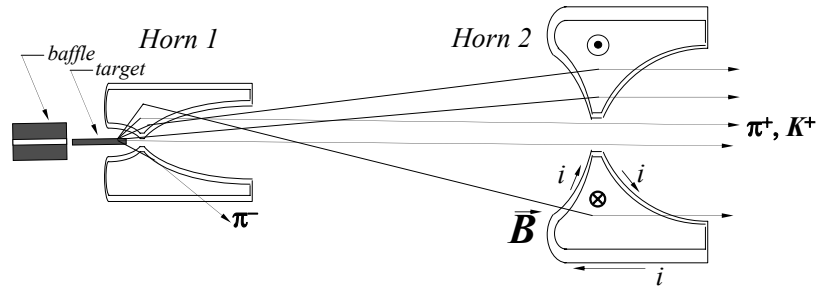
Figure 2.2: NuMI magnetic horns and focusing (not to scale). Forward horn current (FHC) mode focuses positively charged particles. Figure taken from [**?**]

to the NuMI beamline repeats every 1.87 sec[4]. The NuMI beamline was designed to handle up to 4×10^{15} protons per cycle; nominal running mode produces $\approx 3 \times 10^{15}$ protons on target (POT) per cycle.

2.1.2   Target and Horns

The 120 GeV proton spill from the Main Injector hits a graphite target. The target has dimension of $6.4 \times 15 \times 940$ mm^3. It is long enough so that the protons are likely to interact with carbon nuclei. The target is made narrow so that the produced $\pi^{\pm}$ and $K^{\pm}$ can escape out of target sideways without losing much energy. The target is cooled by a water flowing stainless steel pipe surrounding the target.

Produced secondary particles out of the target spread out in random directions. The charged particles are focused by two toroidal magnetic horns, which is analogous to focusing of light using a pair of convex lenses as shown in Fig. 2.2. Secondary particles can be either positively charged or negatively charged, and magnetic horns can focus only one of the signs of electric charge. When the horns are in forward

---

[4]2.2 sec before Tevatron shutdown [**?**] because of extraction to anti-proton source

horn current (FHC) mode, they focus π^+ and K^+ but defocus π^- and K^-. Most focused π^+ produce neutrinos by the decay $\pi^+ \rightarrow \mu^+ + \nu_\mu$. Secondary particles with very small transverse momentum may travel directly to the decay pipe without passing through the magnetic field because they do not require focusing to travel down the beam pipe. The FHC beam is neutrino-dominant, but it also contains anti-neutrinos, especially at high energy. In the reverse horn current (RHC) mode, π^- and K^- are focused which creates an anti-neutrino dominant beam.

The elliptical inner boundary of the horn makes the horn act like a convex lens. The charged particles produced from the target have spread in energy and angle. In a magnetic focusing horn, the focal length of the "lens" depends on the momentum of the particle. Since the target is long, the particle creation locations also vary widely, which introduces spread in the relationship between the angle and the entering position in the horn. Thus, not every particle experiences the same focusing through horn system. The nominal setting for most of our dataset, the low energy (LE) mode, produces a neutrino beam with a peak energy of about 3.5 GeV. By moving the second horn and the target position relative to a fixed first horn, different peak neutrino energies can be selected. Because of the difficulty of moving the second horn, only the target position is changed to tune the beam to higher energies. These non-optimally focused beams are called the pseudo-medium energy (pME or, colloquially in our experiment, just ME) and pseudo-high energy beam (pHE), respectively. Simulated neutrino spectra of the LE and (pseudo)-ME modes are shown in Fig. 2.3.
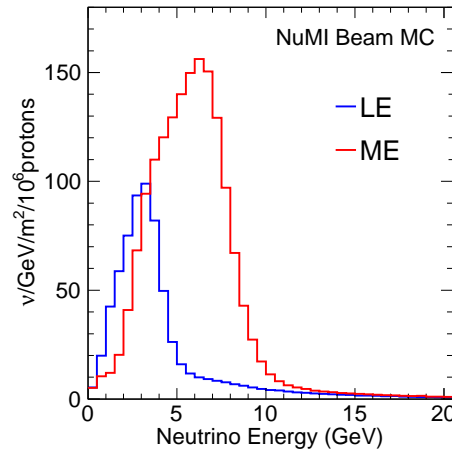
Figure 2.3: FHC-LE and FHC-ME fluxes predicted from the NuMI beamline simulation

2.1.3 Decay Pipe and Hadron Absorber

After the horn focusing, pions and kaons continue to a 675 m long decay pipe. Unstable particles need to fly some distance before they decay. More relativistic (higher energy) particles need a longer distance to decay due to relativistic time dilation. In principle, the longer and wider the decay pipe, the more neutrinos are produced. However, since excavation of the underground tunnel for the decay pipe was costly, the optimal transverse size and the length of the decay pipe were balanced against cost when the experiment was designed. Originally, the interior of the decay pipe was held under vacuum to minimize the loss of pions and kaons from interaction with air. But in 2008, concerns about mechanical integrity of the radiation-damaged decay pipe window led to a decision to fill the decay pipe with helium, which resulted in a slight decrease of neutrino flux due to absorption of pions and kaons.

Any undecayed hadrons and the remnants of the proton beam are stopped by

a hadron absorber at the end of the decay pipe. The hadron absorber consists of blocks of metal and concrete, which contain the hadronic showers that result from the interactions of these particles. The concrete block helps to absorb thermal neutrons. A cooling system in the absorber is necessary since the stopping hadrons carry a significant fraction of the total beam power, which averages over time to roughly 350 kWatts during our run.

2.1.4 Beam Monitors

A hadron monitor is located between the decay pipe and the hadron absorber. It mainly measures the uninteracted proton beam from the target. The hadron monitor consists of a 7×7 array of ionization chambers, which provide the beam profile of the uninteracted proton beam. Thus, beam alignment can be monitored from the hadron monitor. Also the rate of uninteracted protons is monitored as a check for healthy running condition of the target. For example, misalignment of target and the beam would cause an abnormally high rate as absorption of the beam in the target would be reduced.

A pion decay in the decay pipe results in a neutrino and its associated muon. Muons typically penetrate the hadron absorber. The muon flux is reduced to almost zero in ≈ 240 m of unexcavated rock between the hadron absorber and the MINERvA detector. To monitor the muon flux, there are four alcoves cut into this rock where ionization chamber detectors are located. The first three of these were instrumented during the LE run. Muons lose a predictable amount of energy when they traverse the rock between the absorber and the alcoves, almost independent of muon energy itself. Therefore, a certain minimum energy is required for the muon to reach each alcove. The muon energy threshold energies for alcoves 1, 2, and 3

are 5, 12, and 24 GeV, respectively [**?**]. Since a muon is created in a pair with a neutrino and their energies are correlated, the muon monitoring provides useful real-time monitoring of the neutrino flux and, in principle, another way to constrain the neutrino flux, although this technique is limited by the absolute calibration of the muon chambers and backgrounds from electrons kicked out of atoms as the muons traverse the rock near each alcove.

2.2 Minerva Detector

2.2.1 Detector Overview

The MINERvA detector is composed of several sub-detectors: a Nuclear target region, a fully active Tracker and electromagnetic and hadronic calorimeters, the Ecal and Hcal, respectively. All sub-detectors are made by stacking the same scintillator planes with differing passive material serving as either interaction targets or absorbers for calorimetry. Two scintillator planes and associated passive materials form a module, except in the case of the Hcal modules, which have one scintillator plane and one steel absorber. The Nuclear target region, Tracker, Ecal, and Hcal consist of 22, 62, 10, and 20 modules, respectively. Each scintillator plane consists of 127 triangular scintillator strips with a wavelength-shifting fiber embedded. A scintillator strip has 1.7 cm height and 3.3 cm width. The cross section of a scintillator plane is shown Fig. 2.4. Scintillator planes are hexagonal and they are arranged in the detector in three different orientations denoted X, U, and V. Strips in the X-plane are vertical, and particles passing through an X-plane strip indicate the horizontal coordinate at that plane by the identity of the strip or strips. The vertical position at which the particles passes through the strip, however, is not measured
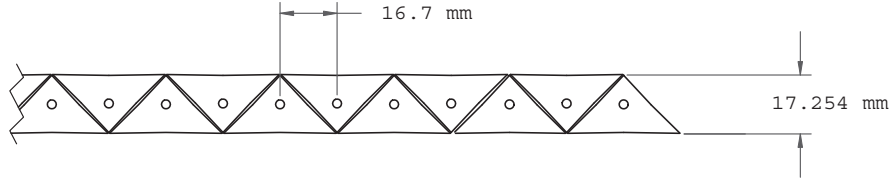
Figure 2.4: The cross section of a scintillator plane. The alternating arrangement of triangular scintillator strips gives better position resolution by light sharing in adjacent strips.

directly in the scintillator. A U-(V-)plane is made from rotating the X-plane by -60 (+60) degrees around the z-axis which is defined as in Fig. 2.5. The three different coordinates, X, U and V, provide three dimensional track reconstruction. Plane orientation in the assembled detector follows a repeating VXUX pattern.

Ecal and Hcal modules are made by sandwiching the scintillator plane with lead and steel absorbers, respectively. Each Tracker plane has a 2 mm thick lead collar to provide electromagnetic calorimetry for side-exiting particles, and this region is called the side-Ecal. An Ecal module is similar to the Tracker module, but each scintillator is covered with a 2 mm lead absorber. The Hcal module has 2.54 cm steel absorber in place of one of planes in a module. In the Nuclear target region, five solid targets and a water target are separated by either 2 or 4 tracking modules. A liquid helium filled cryostate, the Cryotarget, and a veto wall of scintillator with steel shielding are located upstream of the detector. The MINOS near detector [**?**] is downstream of the MINERvA detector and serves as a muon spectrometer for MINERvA. The Outer detector is a barrel hadronic calorimeter, and it also serves as a mechanical support for each module. The radiation lengths, X_0, in the Tracker and Ecal are 42 cm and 5 cm, respectively. The whole length of the Tracker corresponds
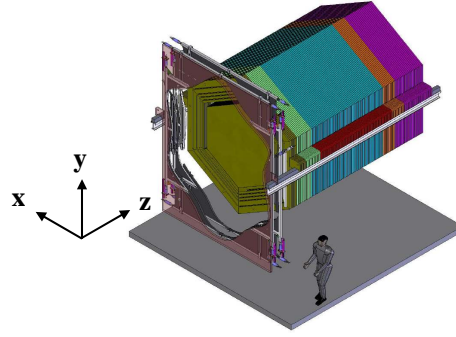
Figure 2.5: The MINERvA coordinate system. The coordinate system is based on detector arrangement. The Positive y-axis is gravitationally up. The NuMI neutrino beam centerline is in the y-z plane and points slightly downward by ≈ 3 degrees with respect to the z-axis.

X-view   **U-view**   **V-view**
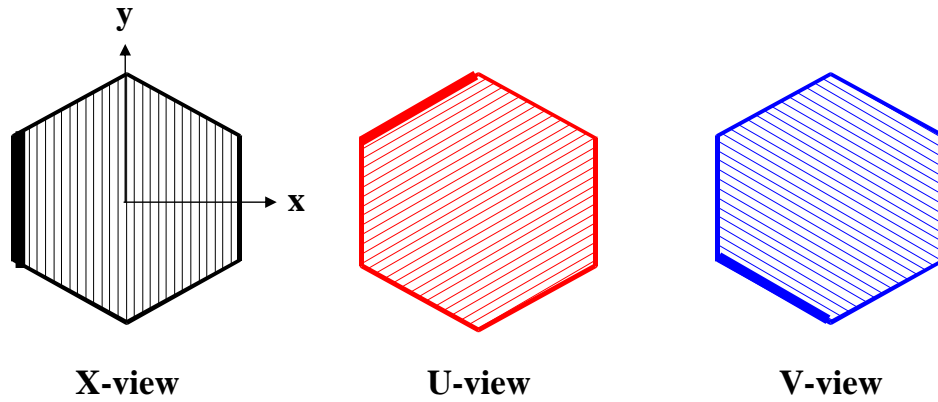
Figure 2.6: Plane orientation as viewed from the positive z-axis. The dark line indicates strip 1.

to $6X_0$ and Ecal is $8X_0$. This work requires that candidate events originate from the Tracker and excludes events originating from the Nuclear target region.

2.2.2 Detector Technology

Extruded scintillator strips with wavelength-shifting (WLS) fiber readout are the basic building blocks of the MINERvA detector. The scintillator strips are extruded from the commercial polystyrene $((C_8H_8)_n)$ pellets with wavelength shifting dopants, 1% PPO and 0.03% POPOP [?] to allow for efficient transmission of scintillation light within the strip. The strip is co-extruded with reflective material, polystyrene with 25% TiO_2 by weight, which makes a thin reflective coating around the strip. The strips are extruded in two shapes, triangular and rectangular in cross-section, each with a hole in the center. A WLS fiber is inserted into the hole and glued in place with optical epoxy, which improves the light transmission from the scintillator to the fiber by about 50%. One end of the WLS fiber is polished and mirrored so that the light transmitted on the fiber can be read out at the other end of the fiber. The WLS fiber absorbs purple light from the scintillator strip and emits longer wavelength, green light. A fraction of the produced green light is trapped in the optical fiber and is transmitted by total internal reflection to a photomultiplier tube (PMT). The WLS fiber transports the light from the scintillator strips to the outer edge of each module. Each WLS fiber is connected to a matching clear optical fiber, which transports the light to the PMT. The clear fiber is more efficient for transporting light over the long distance to the PMT because the attenuation length of the WLS fiber is only about 1.5 m, while in the clear fiber it is about 8 m.

2.2.3 Detector Construction

Plastic scintillator strips were extruded at the FNAL-NICADD Extrusion Facility at Fermilab. The extruded scintillator strips have a slightly irregular shape of the

outer cross-section and the hole which varied within specified tolerances during production. The scintillator strips were made in a few production batches. The shape and dimension of sample strips in each production were checked to see if they meet the specifications.

The assembly procedure of the scintillator plane was designed to ensure the correct strip pitch and plane thickness, which are critical parameters for event reconstruction and for successful assembly of the entire detector. Strip lengths in a hexagonal plane vary with the location of the strips. Strips are placed and glued into a plane, and they are cut together in the shape of a trapezoid using a saw cut. Strips are sandwiched by two lexan films. The lexan skin provides light-tightness and mechanical binding. In order to strengthen the adhesion, additional lexan film is added in the scintillator plane. It runs through the strips like a web, which makes each group of three strips enclosed by lexan films. A plane with epoxy and lexan wrappings is pressed by placing it in a vacuum envelope. Assembly and epoxy gluing of a whole 127 strip plane is not trivial for real plane production because of the large size of the plane compared to human arm length. Therefore, strip assembly and epoxy gluing is done in five pieces, called planks, for each plane. The number of strips in each of the five planks is 24 in the outer planks and 31 in the center plank.

Each WLS fiber was cut for designated length. Both ends of the fiber were polished to ensure a square and optically smooth surface, and one of these ends of each fiber was mirrored by vacuum sputtering deposition of aluminum. The prepared WLS fiber was then inserted into a hole in the scintillator strip. Optical epoxy was injected into a hole of the scintillator strip from the mirror end of the fiber using a machine-pressurized syringe. The non-mirrored end of each fiber, the so-called "read out" end, is mechanically supported by a guide structure and then enclosed

by a light-tight flexible baggie. Eight fibers are grouped into an optical connector at the edge of the baggie. Once the scintillator plane with baggie is complete, the side-Ecal lead absorber is attached to the plane.

Strongbacks were used to move the heavy modules around securely for assembly and transportation. The hexagonal OD is made by welding six trapazoidal pieces. Each steel trapazoid is prepared with scintillator strip slots. The welding is done with six wedges clamped on the strongback to minimize distortion from heat.

Finally two scintillator planes and OD scintillator were assembled together with the OD frame. Once the module is complete, it was scanned by the Module Mapper for fiber attenuation measurement and fast quality assurance checks. Details of the Module Mapper will be described later in this chapter. Each successfully built module was transported to the underground detector hall and hung on the detector stand.

An optical fiber cable transports light from the WLS fiber to PMT boxes. One of these clear fiber cables has eight fibers inside a light-proof tube. A commercially manufactured (Fujikura/DDK) connector was used with pluggable connector at both ends mated in a plastic box. Alumilite polyurethane molding is used to join the tubing to the connector with light-tightness and to support the fibers.

The PMT box rack is located on top of detector to support the PMT boxes. The clear fiber cables provide the optical connection between the outer edge of the OD and bottom of PMT box. The clear fiber cable mapping was devised to minimize the cable length and to simplify the connection of more than 4000 clear fiber cables. The connection map pattern is shown in Fig. 2.7. The entire detector map is shown in Fig. 2.8.

Figure 2.7: Clear fiber cable connection map pattern. One row in the upper table corresponds to one module, and one color box in upper table matches with one PMT in bottom table. Green, blue, orange boxes in upper table represent X, U, and V-planes correspondingly.

2.2.4 Photomultiplier Tube (PMT)

A photomultiplier tube (PMT) is a very highly sensitive photon detection device that is commonly used for particle detector readout. A PMT consists of a photocathode, focusing electrodes, and a series of dynodes, all of which are enclosed in a vacuum glass tube. Photons entering through a PMT glass window hit a photocathode which converts the photon to photoelectrons. Focusing electrodes guide the photoelectrons to photoelectron amplifiers, dynodes. Due to electric potential between focusing electrodes and the first dynode, when the photoelectron hits the first dynode, it knocks off more photoelectrons. This larger number of photoelectrons are focused to the next dynode by electric potential. For MINERvA's PMTs, an overall gain of about 3×10^5 is obtained from 12 stages of dynodes.

A conventional PMT has a single large photocathode window and has no ability to detect the position that the photon strikes on the photocathode. A multi-anode PMT has a dynode structure that preserves the position of the photoelectron from the photocathode, so that the position of the incoming photons through the PMT face can be measured. MINERvA's Hamamatsu R7600-M64[5] PMTs have an 8×8

---

[5]PMT assembly model number: H8804MOD-2
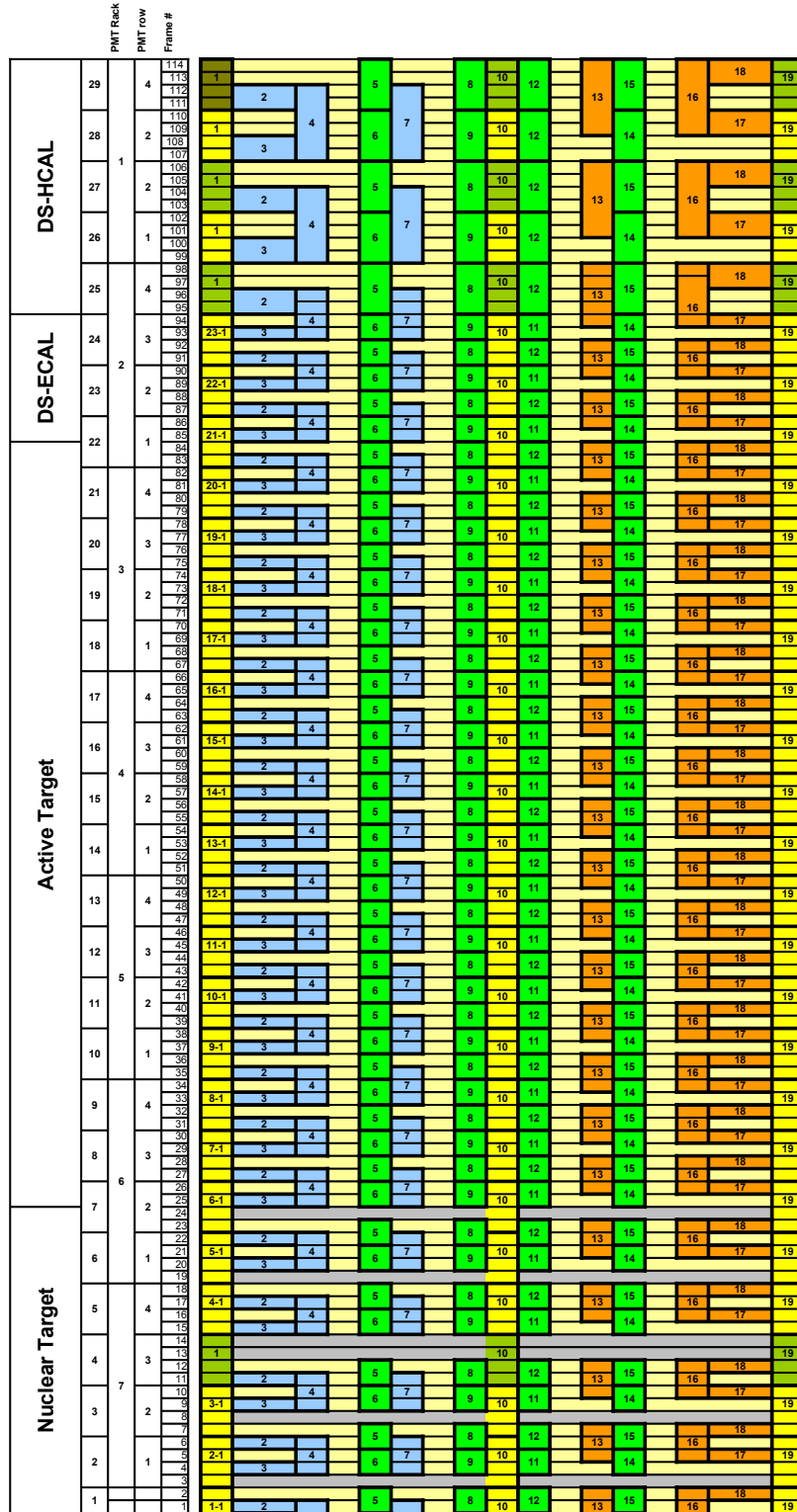
Figure 2.8: Clear fiber cable connection map

multi-anode array for a total of 64 independent channels in a compact unit. The effective area of a pixel is 2×2 mm^2, and pixels are separated by 0.3 mm. MINERvA illuminates each pixel with light from a 1.2 mm diameter optical fiber.

The response in different channels of a multi-anode PMT is not uniform due to variation of photocathode sensitivity and dynode gain. Due to the array structure of the anodes, the PMT has also a few % cross-talk between neighboring pixels.

The photocathode, made with bialkali, gives about 10–25% quantum efficiency to convert a photon to a photoelectron. The sensitive spectral range is 300 to 650 nm with peak sensitivity around 420 nm, which WLS fiber produces. Detection efficiency is a combination of quantum efficiency and collection efficiency. The collection efficiency is the fraction of the photoelectrons from the photocathode captured by the first dynode. The collection efficiency varies 60%–90% depending on dynode types. The R7600-M64 has good collection efficiency [**?**]. MINERvA uses an 800 Volt cathode to anode potential as the nominal PMT high voltage; the maximum allowed voltage is 1000 V. PMT gain has a dependence of ambient temperatue and decreases as the temperature increases at the rate of about $-4\%/$C$^\circ$[**?**].

2.2.5 PMT Box

Each PMT is housed in a light-tight steel box. Steel is chosen to minimize sensitivity to stray magnetic fields from the MINOS near detector. A PMT box is a 11.43 cm diameter, 28 cm long, and 2.36 mm thick steel cylinder. The box also houses fiber routing and PMT electronics. A PMT is mounted on a plastic PMT holder, which is held by 4 metal rods in the box. In order to interface fibers to the PMT with precise alignment, fibers are fixed in a plastic cookie. A fiber weave is used between the cookie and clear fiber cables at the endplate of the PMT box. The weave interleaves

adjacent channels to provide a degree of isolation on the PMT pixel grid for signals originating at neighboring locations in the detector. Each PMT box has a Front End Board (FEB) mounted on a endplate outside and ports for two light injection (LI) fibers.

2.2.6 Data Acquisition System

A TriP-t ASIC based FEB is used to read out the PMT signals [**?**]. Six TriP-t chips on the FEB provide both charge (ADC[6]) and time (TDC[7]) information. Each channel has three gains, separated logarithmically by factors of 10, to span a wide range of amplitudes with only 12-bit ADC. On each FEB, 64 channels × 3 gains are readout by six TriP-t chips as shown in Fig. 2.9. 16 channels with both high gain and medium gain are read out by one TriP-t chip. Two TriP-t chips each read out 32 low gain channels. This arrangement is driven by the availability of discriminators. Each TriP-t chip has 16 discriminators but 32 inputs total. The discriminator only uses the high gain, which is the most sensitive channel. Signal timing is recorded when the discriminator is fired. When high gain channels are read out, medium and low gain channels are read out together to tie medium and low gain hits with high gain hits, so timing is provided for the medium and low gain channels.

About 10 FEBs are controlled by a LVDS[8] link in a daisy chain arrangement. Each chain of FEBs is connected to a Chain Read Out Controller (CROC) which communicates with other VME[9] modules. Each CROC receives timing signals from the CROC Interface Module (CRIM). One CRIM controls up to 8 CROCs. The

---

[6]Analog-to-digital converter
[7]Time-to-digital converter
[8]Low-voltage differential signaling
[9]VMEbus is a computer bus standard, which is described by ANSI/IEEE 1014-1987
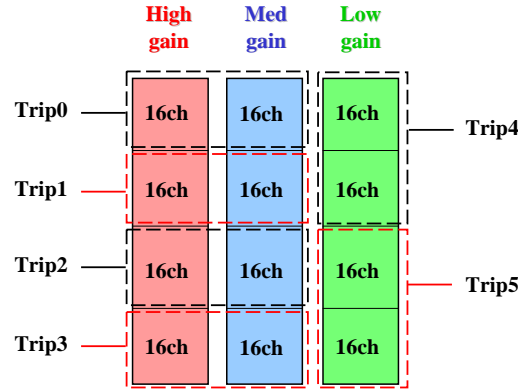
Figure 2.9: Six TriP-t chip readout map on a Front End Board (FEB)

CROCs get a global time from the beamline clock. Because the neutrino interaction rate is low, an event trigger is not necessary. The electronics opens a gate to begin readout when beam spill starts. The duration of beam spill is about 10 μs. If any discriminator is fired, charge on all 32 channels which share a common TriP-t for the low, medium or high gains is integrated over a 150 ns window. After each integration window, the charge is pushed into an analog pipeline along with the timestamps of any hits, and the charge is reset. While pushing hits and resetting, 32 channels are not available for accepting new hits for 188 ns, known as dead time. After the reset, if beam gate is still open, those channels are ready again for the next hits. After the spill is finished, each TriP-t chip unpacks its analog pipeline, digitizes all channels integration windows and transmits the data to CROC.

2.3   Calibration

2.3.1   PMT FEB Gain Calibration

Front End Boards (FEBs) convert charge to digital information with three gains. Because charge is digitized with a finite number of digits, if too much charge is fed into a channel, the ADC saturates. High gain provides good amplification, which allows seeing the one photo-electron peak in ADC, but it only covers a small range of charge. The low gain can cover a wide range of charge, but it has poor resolution at low charge. Three different gains: low, medium, and high gain, are each optimal for a range of charge on each channel.

Each FEB gain was measured in the test stand. Charge is injected for each gain, and ADC value is measured. Several values are measured for range of 0-40 pC charge injection, and an ADC vs. charge curve is fitted for each gain. ADC is mostly linear in charge, but there is some nonlinearity. In order to handle nonlinearity, $f_{\mathrm{ADC}}(Q)$ is modeled with a triple piecewise linear function,

$$\Delta ADC = f_{\mathrm{ADC}}(Q) = \begin{cases} s_1 Q, & \text{if } Q < Q_1 \\ s_2 Q + Q_1, & \text{if } Q_1 < Q < Q_2 \\ s_3 Q + Q_2, & \text{if } Q_1 < Q < Q_{\max} \end{cases} . \qquad (2.1)$$

This kinked triple linear gain response is a feature of the TriP-t chip. This triple linear parameterization is a faithful description of the response over the full range to better than 1% accuracy. Triple linear fits on three gains of one ADC channel are shown in Fig. 2.10.

ADC vs. Charge
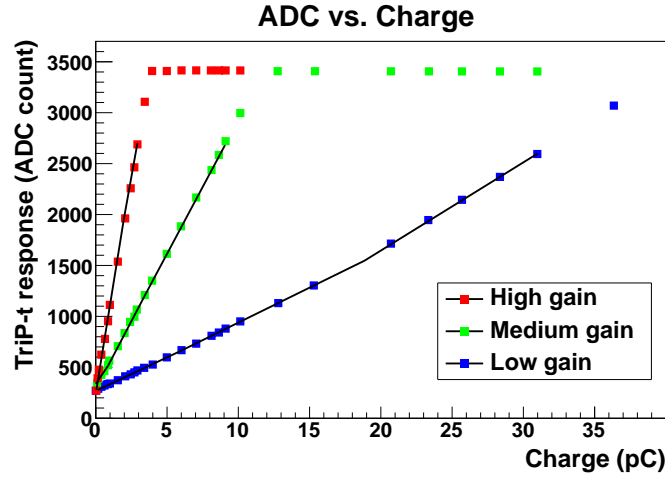
Figure 2.10: Triple linear fits on three gains of a ADC channel

2.3.2 Light Injection

Light injection (LI) is necessary to monitor changes in the gain of the PMT over time. Pulsed green LED light is generated in LI box, and the generated light is transported to each PMT box by a pair of 1 mm optical fibers. A light diffuser attached to each fiber illuminates light on 64 fibers that are mounted on a cookie. The LI box gets a beam spill timing signal from CRIM. LI calibration is performed between beam spills. Injected light is adjusted to produce about 1 photoelectron (PE) in the photocathode. The produced ADC spectrum is a superimposition of the big pedestal peak, which represents the case of no light reaching the PMT, a signal shoulder and a small background from light reaching the PMT from other sources, such as cosmic rays, passing through the scintillator in coincidence with the light injection pulse. The pedestal peak position should be also measured since a signal charge is an ADC value measured relative to a pedestal position. The signal shoulder distribution is described by Poisson statistics of photoelectrons and electronic smearing from the spread of amplified electric signal at each stage, which
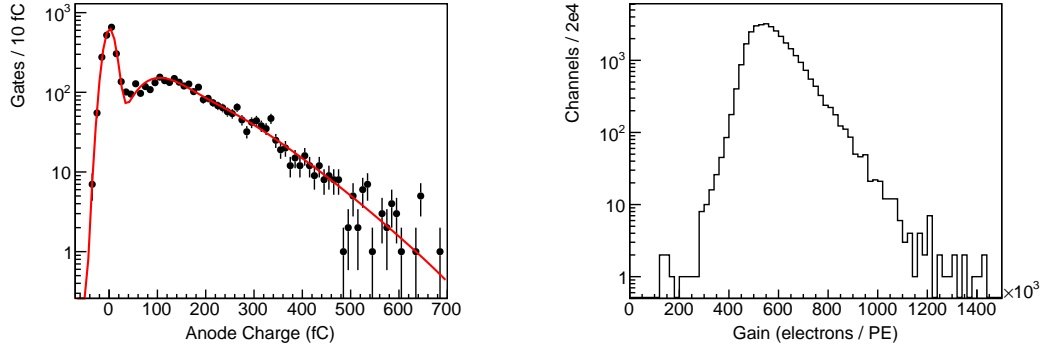
Figure 2.11: Left: One PE fit. Right: Gain variation on channels after tuning PMT HV

is modeled by a Gaussian distribution. A fit model including pedestal, signal, and background is used to match with the LI produced ADC spectrum to extract the gain for one PE. One example fit is shown in Fig. 2.11. The gain measurement provides the conversion factor between ADC counts and PE.

PMT gain varies from one to another depending on how each component like photocathode, focusing electrodes, dynodes, and voltage divider in a PMT are manufactured. The PMT gains can be regularized by adjusting the high voltage. The high voltage in each PMT was adjusted to make average gain of 8 lowest gain pixels same for entire PMTs. A distribution of gains of channels, after the high voltage tuning, is shown in Fig. 2.11.

2.3.3   Module Mapper and Attenuation Calibration

The Module Mapper is a large source scanner for the MINERvA modules. The scan provides quality control of modules and a measurement of the light attenuation of each strip in the module. Various issues like broken fibers, light leaks, and glue
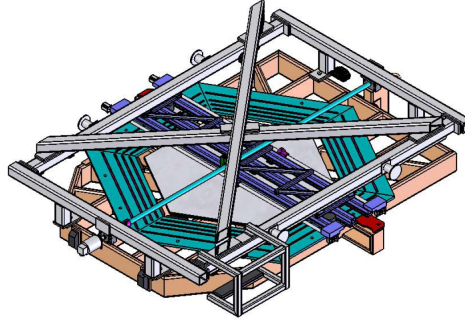
Figure 2.12: Minerva Mapper

problems can be identified before the module is installed. It also provides fast feedback to the scintillator plane fabrication group during module construction. The same PMTs and fiber cables as the full MINERvA detector are used to read out signal from the module. The response of a strip due to the radioactive source is determined from an accumulated ADC distribution after short exposure of a radioactive source. A customized data acquisition system is used to perform the task in synchronization with a motion control driver for the radioactive source.

The measured attenuation of light in an individual scintillator strip is also used to correct light attenuation in later offline calibration. Further corrections to the attenuation curve were implemented after the module construction to handle effects of the side-Ecal lead absorber and strip end.

An engineering drawing of the Module Mapper is shown in Fig. 2.12. The Module Mapper sits on the top of a strongback that holds the module to be scanned. Due to safety issues with heavy moving parts during the operation, the Module Mapper is kept in an interlocked cage. Modules on the strongback were moved in and out the mapper cage by an overhead crane which prohibits personnel from accessing the scanner during operation.

The Module Mapper has two source carriages. Dual source heads are employed to reduce the scan time. Three stepper motors are used to position the two radioactive sources. The two carriages share a vertical motor while the horizontal motion is handled independently by two smaller motors. A cesium-137 source, which produces 661.7 keV gamma is used as the radioactive source. High strength sources of $\sim$ 5-10 mCurie activity are used to make scan faster. Each source is installed in a lead cone to illuminate only a localized area of the scintillator plane. The lead cone has 6 inch diameter and 4 inch height. When unused, the sources carriages are parked in a secure place where the lead cone is covered by a shielding lead plate. The lead cone angle was optimized from a Monte Carlo study to achieve good transverse position resolution of the strip with reasonable exposure time.

Each module has 302 channels: two ID planes with 127 strips each and the OD with 48 strips. Four PMTs cover two ID planes. Two PMTs are used for OD to avoid long optical cables between module and PMT. The clear fiber cable connection for module mapping is shown in Fig. 2.13. PMT2 and PMT3 which connect the U-plane in the XU module cable map are moved to the right to connect to the V-plane in XV module cable map.

The movement and positioning of radioactive source is supported by the rigid Mapper frame during the scanning. But the accurate alignment between the scintillator plane and the Mapper frame is not guaranteed due to the way the scintillator plane is mounted in the module and the imprecise alignment of the docking guides between the Mapper frame and the strongback. Precsision reference points are marked at corners of the scintillator plane, and positions of these fiducial marks are measured by a Mapper fiducial camera that is attached on the source carriage to correct Mapper coordinates to actual module coordinates. Translation (x, y) and
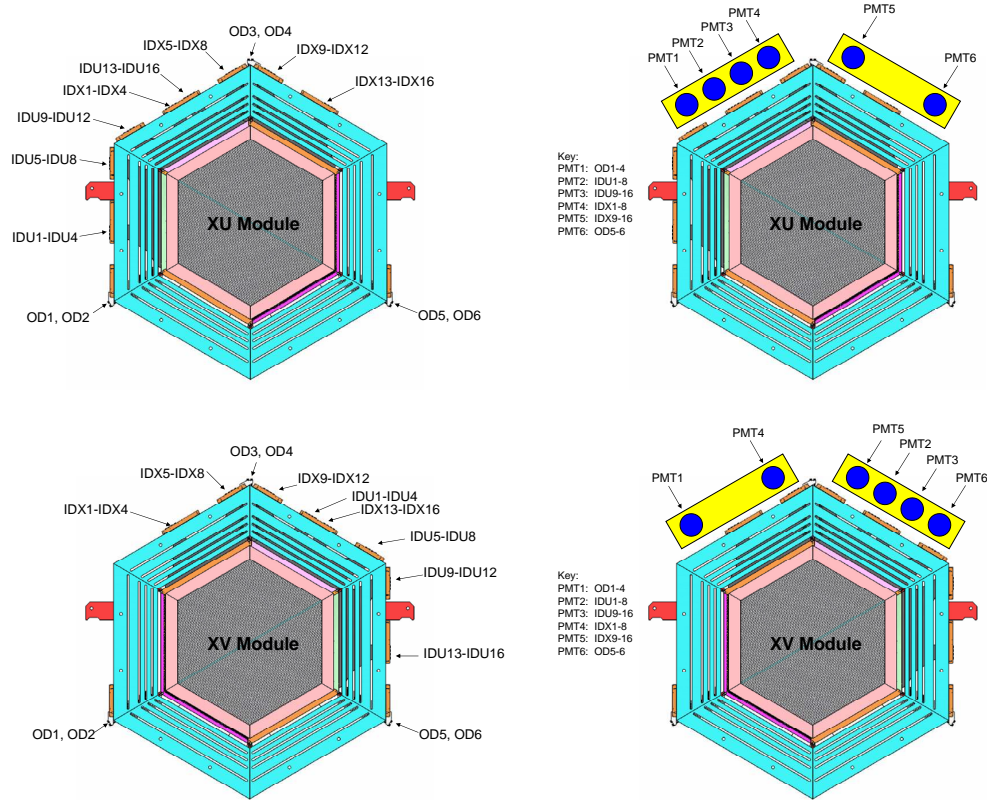
Figure 2.13: Upper: XU Module cable connection map, Lower: XV Module cable connection map

rotation corrections are applied using the measured positions of fiducial marks at the beginning of a scan.

The motion control for radioactive sources and the mapper DAQ are written in MS Visual Basic. The mapper Motion control GUI is shown in Fig. 2.14. Sources are placed at pre-configured positions on a module and then DAQ reads ADCs from FEBs until it collects 1000 discriminator-fired hits. 1000 ADC hits provides reasonable statistics to determine a pedestal location, while one module scanning time is limited to order of half day. During the readout time, the sources do not move. After finishing the readout at a source position, sources are moved to the
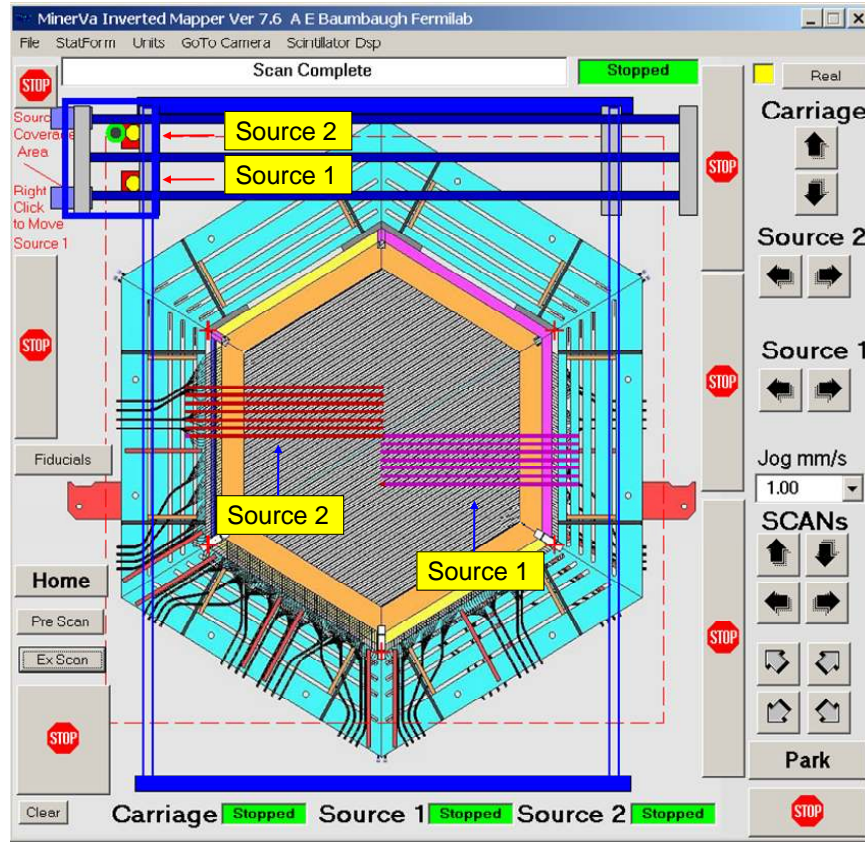
Figure 2.14: MINERvA Mapper motion control GUI

next scan position, and the scan/move cycle is repeated. Scan and move-to-next cycle takes about 3-4 seconds, but one module has about 15000 scan positions, which makes the whole module scan time about 12 hours. All these are automatic based on a scan pattern configuration. Because two sources are coupled in vertical position, two source positions are specified by three numbers, (y, x_1, x_2), where y is common y position (vertical) and x_1 and x_2 are x positions for each source. The hexagonal scan pattern shown in Fig. 2.15 is used to scan two planes, upper X-plane and lower U or V-plane simultaneously.

When the PMT gets light signals from an illuminated strip, the ADC distribution
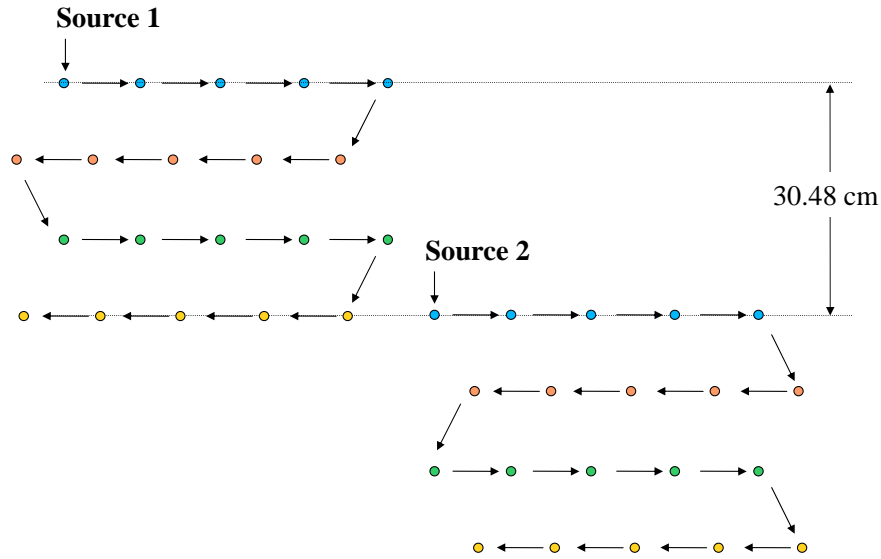
Figure 2.15: Mapper source position pattern

will have ADC values above a pedestal peak. Due to the AC coupling of each input to the ADC, charge on each channel out of time with the readout causes the pedestal position to move to negative direction. The amount of pedestal shift is proportional to total hit activities over the RC time constant of the circuit, which is long compared to the 10 μs read out gate. By measuring the pedestal shift, we can measure how much illumination the strip has received. Fig. 2.16 illustrates the pedestal and signal for cases of different activity in the strip during the scan. A Gaussian fit around the pedestal peak is repeated at each source position.

When a radioactive source approaches a strip, the response of the strip increases as it gets more illumination from the source. Thus when the source scan path is perpendicular to strip, the response of the strip becomes maximum at the source closest to the strip. This perpendicular scan is called a transverse scan. Fig. 2.17 shows a transverse scan and illustrates that the strip position can be identified by
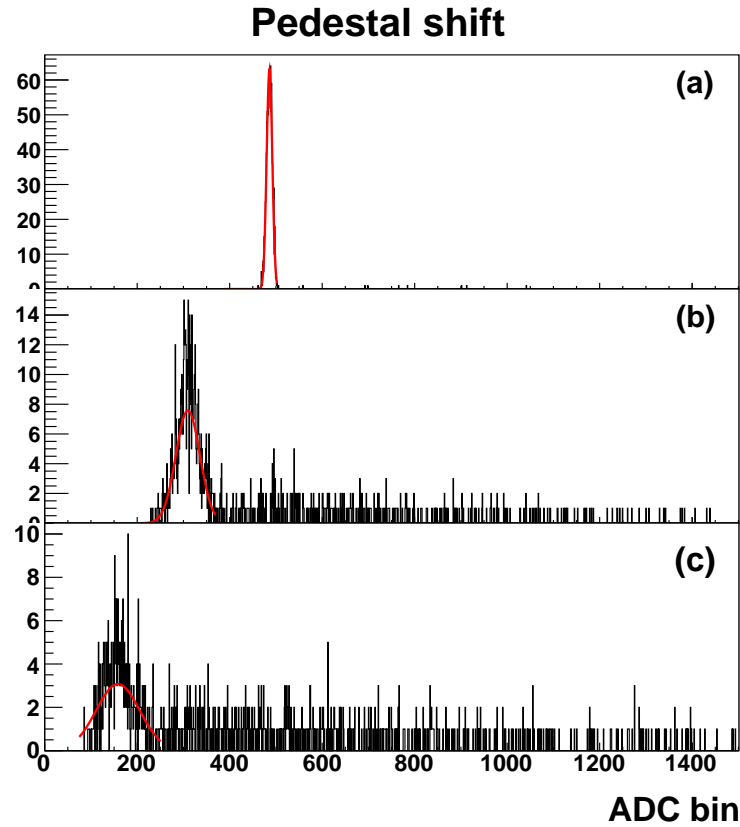
Pedestal shift

Figure 2.16: ADC pedestal shifts for different cases: (a) nominal pedestal position when no source illumination, (b) pedestal shift when the source is near the strip, (c) maximal pedestal shift when the source is closest to the strip.

maximum response position.

One transverse scan gives a light yield measurement at a position of the scintillator strip, where the transverse scan intersects with the strip. Since light attenuates during the propagation in the fiber, if the transverse scans are repeated at several positions along the strip, an attenuation curve is acquired using maximum responses the transverse scans. An attenuation curve is shown in Fig. 2.18. The light output is maximum when the source is near the readout end of the strip and minimum at far end of the strip.

Transverse scan (mod33-layer2-strip61)
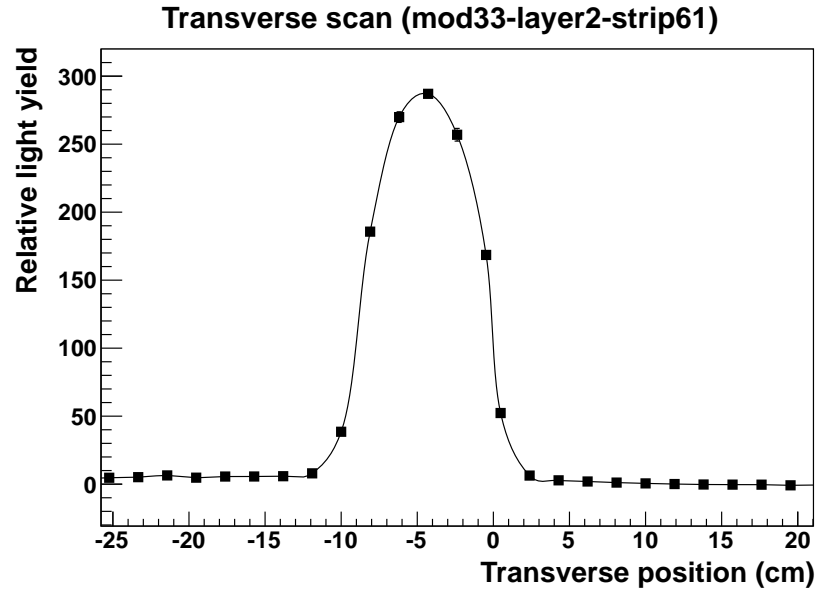
Figure 2.17: Transverse scan

Attenuation curve (mod33-layer2-strip61)

A	533.7 ± 4.479
λ	343.5 ± 3.931
L_{strip}	$235.3 \pm \quad 0$
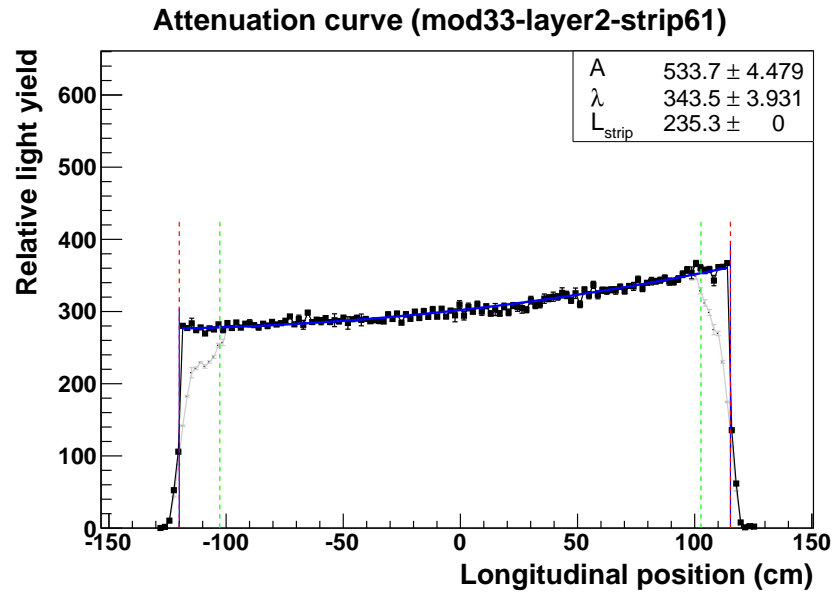
Figure 2.18: Attenuation curve of a single strip

Each attenuation curve is fitted with a single exponential function with a reflected light term:

$$f_i(x) = A \exp\left(-\frac{L_i^{\mathrm{CF}}}{\lambda^{\mathrm{CF}}}\right) \exp\left(-\frac{L_i^{\mathrm{ext}}}{\lambda}\right) \exp\left(-\frac{x}{\lambda}\right) \left[1 + R \exp\left(-\frac{2(L_i - x)}{\lambda}\right)\right],$$
(2.2)

where A is amplitude, λ is attenuation length of the WLS fiber, L_i is length of strip-i, L_i^{ext} is WLS fiber length outside strip-i, λ_{CF} is attenuation length of clear fiber, L_i^{CF} is length of clear fiber of strip-i, λ^{CF} is attenuation length of clear fiber, and R is mirror reflectivity. When the fit is performed, several parameters are fixed to known values. Mirror reflectivity 0.83, measured in destructive tests of samples, and a clear fiber attenuation length of 750 cm from bench measurements are used. The clear fiber length, L_i^{CF}, varies for each cable that holds a group of 8 fibers. WLS fiber length outside strip L_i^{ext} and strip length, L_i^{CF}, also vary for individual strips but are known based on the design of the module. Only the amplitude A and WLS attenuation length L are free parameters, and they determine the shape of an attenuation curve.

Every tracker module has a 2 mm thick lead-collar for side-Ecal absorber. The side-Ecal absorber is located between the red line and green line in Fig. 2.18. Strip response where the lead collar covered is $\approx 20\%$ lower due to absorption of the γ rays in the lead. The grey curve in Fig. 2.18 shows the attenuation curve before any corrections. Correction for side-Ecal lead is applied to recover the original attenuation curve. Also the response has a falling edge effect at the both ends of the strip where the radioactive illumination begins to illuminate points off the edge of the strip. Again, a falling edge correction is made to recover original attenuation shape.

After side-Ecal and falling edge corrections, the attenuation curve is fitted, resulting in A and L. An anomalous attenuation curve is most likely due to a local glue void, but sometimes the attenuation curve shows sudden falling amplitude when there is a broken or damaged WLS fiber inside the scintillator. Amplitude, A, is useful to check absolute light level for quality control of the scintillator plane. In principle, A represents the relative response of strips, but it is not used in offline calibration because the PMT gain in Mapper is not rigorously controlled and measured as in the full MINERvA detector. Instead strip-to-strip calibration using rock muon tracks in offline is used for relative strip calibration. From the mapper scan, only the attenuation curve shape is used in offline analysis to correct light attenuation of the WLS fiber. If the attenuation curve is fitted well with data points, the attenuation correction is made based on a parameterized function. If data points have enough variation from the fitted curve, point-by-point with interpolation is used for the attenuation correction.

2.3.4   Strip-to-Strip Calibration

Rock muons provide a good calibration source. They are shallow angle muons, passing through the whole detector. Rock muon tracks are reconstructed with high efficiency. In these events, the muon's energy loss per unit length is almost constant throughout the detector. Therefore, energy loss per scintillator plane with angle correction will be ideally the same for each module. Deviation of average energy loss of a module from a sample of many rock muons represents relative average response of the module.

Strip-to-strip calibration is performed after all other basic calibrations applied, such as PMT pixel gains, FEB gain, WLS fiber and clear fiber attenuation correction.

From the reconstructed three dimensional track, we can determine the expected path length for each triangular strip that the muon track intersects. In order to calculate the path length correctly, accurate alignement of each scintillator plane is necessary before the strip-to-strip calibration. Energy deposited in the strip, normalized by path length should be constant. A large rock muon sample is necessary to have a good average response for each strip. Again, any variation on strip response is used to determine relative strip-to-strip calibration.

2.3.5   Muon Energy Unit (MEU)

Muon tracks also provide a calibration source for absolute energy response of the detector. The energy loss per scintillator plane (dE/dx) by a muon track is defined as muon energy unit (MEU). The absolute energy scale is tuned based on comparison between data and a Monte Carlo (MC) simulation of the measured energy in each plane. The MEU comparison is performed after attenuation correction and strip-to-strip calibration are applied. MEU calibration uses a rock muon sample that matched with MINOS track, where the energy of the muon was analyzed by range or curvature. The MEU is calculated using energy of one or two strip hits (cluster) of muon track. Cluster definition is described in Reconstruction chapter 4.2.2. Visible delta rays from muon track are excluded in muon track for MEU, but there are also irreducible low energy delta rays that are embedded in the muon track, which are accounted for in the Monte Carlo simulation. The absolute scale of reconstructed MC MEU is calibrated using MC true value. The muon energy loss per scintillator has smearing from fluctuation of ionization energy loss and detector resolution, which are also simulated. The spread of the MEU distribution was also checked between data and MC to validate energy smearing of MC.

2.3.6 Alignment Calibration

Track reconstruction and detector alignment interplay. In order to make track reconstruction work correctly, detector alignment should be done. But to perform the track-based detector alignment, the track has to be reconstructed. Because of the way the scintillator plane is fabricated using assembly fixtures to guide scintillator strip positions, strip to strip misalignments are small. Most misalignments come from imperfect position and orientation of the whole scintillator plane. Due to the way two scintillator planes are mounted in a module, accurate positioning is not guaranteed. Also, modules are installed in the detector hall by placing their Outer detector frame hooks on two rails. The exact shape of the hexagonal OD frame is difficult to achieve because it is built by welding six trapazoidal pieces of heavy steel. Hook positions are not perfect due to thermal expansion during welding, which makes accurate positioning difficult.

Alignment for a plane is described by six parameters; (x, y, z) for position and three Euler angles, $(\alpha_x, \alpha_y, \alpha_z)$. Shallow angle track is not sensitive to z alignment. The z alignment cannot be done based on muon track sample, because a high angle muon track is rare, and reconstruction of a high angle track is poor. The position along the z-axis of modules in the sub-detector (Nuclear target, Tracker, Ecal, and Hcal regions) is measured to determine average pitch of modules in each sub-detector. For the same reason, shallow angle tracks are not sensitive to small tilts around the x or y-axes. Thus α_x and α_y are ignored. Shallow angle can precisely measure the (x, y) position of each module and the rotation angle around the z-axis. α_z. One scintillator plane effectively determines one parameter in the (x, y) of each scintillator plane. For example, X-view scintillator planes are not sensitive to y misalignment.

2.3.7 Timing Calibration

Beam spill timing information is coming from the NuMI beamline, whose timing signals are used to trigger the gate for the DAQ. The MINERvA Timing Module (MvTM) distributes the global timing to the MINERvA DAQ.

The LI calibration is also used for timing calibration of individual FEBs. With each FEB, the TDC of 16 channels descriminated in a single TriP chip are based on same reference time. Further channel-by-channel timing is done by muon time-of-flight (TOF). Time slewing effect has to be taken into account to get correct timing because hit time is affected by pulse height. Optical path length difference due to different clear fiber cable length is also taken into account in the timing calibration.

2.3.8 Michel electron

Michel electron is produced by a decay of stopping muon (anti-muon) or a decay chain of stopping $\pi^{\pm}$,

$$\mu^+ \to \bar{\nu}_\mu + \nu_e + e^+ \tag{2.3}$$

$$\mu^- \to \nu_\mu + \bar{\nu}_e + e^-. \tag{2.4}$$

The response of the detector to Michel electrons at different locations can provide a cross-check of the relative calibration. The overall electromagnetic energy scale can also be checked by comparing the Michel electron spectruma in data and MC simulation.

In general, a Michel electron is identified by a delayed signal near the endpoint of a stopped muon track. However, stopped muons or pions from neutrino interactions occurring in the detector also produce Michel electrons. Finding a Michel electron
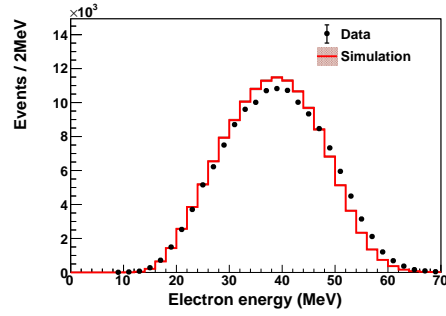
Figure 2.19: Michel electron energy

from a short length stopped track is difficult since reconstruction of the short track is more challenging. Besides the difficulty of short track pattern recognition from small number of hits, the short track is often produced with a high angle where the track reconstruction is poor. Also, short stopped track may be spatially nearby other tracks from the same neutrino interaction. Thus, it is difficult to match the Michel electron with the endpoint of short tracks. But the event rate of unmatched Michel electrons is higher than Michel electrons from rock muons. It is found that the unmatched Michel electron sample has very small background near the Michel electron energy peak. Thus, this unmatched Michel electron sample serves as a high statistics calibration sample. Fig. 2.19 shows data–MC comparison of the unmatched Michel electron spectrum.

Chapter 3

Simulation

3.1 Beamline simulation

A GEANT4[1]-based [?] beamline Monte Carlo (MC) simulation, G4numi, is used to
generate a prediction for the neutrino flux in the NuMI beamline. It replaced the
previous beamline simulation based on FLUKA [?] which is an extensively tuned
hadronic interaction model. However, this prediction could not be tuned to incorpo-
rate recent hadronic production data because the FLUKA license does not allow a
user to modify physics models and because critical information about intermediate
processes is not made available to the user. The GEANT4-based simulation, by
contrast, allows the user to access the complete interaction record for all produced
hadrons, and physics models can be tuned by the user. The Beamline simulation
includes a complete description of the geometry and materials of the baffle, target,
horns, target hall, decay pipe, hadron absorber, muon monitors, and unexcavated
rock in areas relevant for the beamline. The target position and horn current are

---

[1]The GEANT4 version used for the MINERvA flux prediction is 9.4.p03.

configurable.

The Monte Carlo (MC) flux prediction is frequently changed as new constraints from measurements of hadron production in conditions similar to that in the NuMI beamline are added. In principle, each time the flux is changed, the neutrino interaction simulation, detector simulation and reconstruction of this simulated data must be completely redone. This would be very time consuming because of the large number of variations that need to be considered due to the need to study uncertainties on every component of the flux. To avoid this repeated nearly duplicate MC productions, a reweighting technique is used for variations in the flux. Each event in the Monte Carlo simulation gets a reweighting factor from the ratio of new flux to old flux as a function of neutrino energy. To apply the new flux, the reweight factors may be applied on any analysis distribution by filling each event with a weight factor.

3.2   Event Generation

GENIE[2] [?] is an object-oriented neutrino event generator, aimed for common neutrino event generator for current and future neutrino experiments. It is used by various experiments: T2K [?], NOvA [?], MINERvA [?], ArgoNeuT [?], and MicroBooNE [?].

GENIE reads flux information from the external GEANT4 NuMI beamline simulation output files. The GENIE flux driver uses a spatial window to predict neutrino flux at a specific location. This flux window is located upstream of the MINERvA detector, and its position is given in terms of beamline coordinates. The size of the

---

[2]GENIE 2.6.2 is used in MINERvA.

flux window must be big enough to cover the MINERvA detector, but it should not be too big to avoid unnecessary inefficient generation.

To generate neutrino interactions, GENIE must also use a description of the detector materials and geometry. The GENIE flux and material routine is simplified because the neutrino interaction event rate is approximately proportional to the volume and density of detector material. However, there are corrections of order 10% to the neutrino interaction rate depending on the target nucleus. The GENIE flux driver reads the detector geometry in the ROOT [**?**] geometry format. A cross-section spline file is used for efficient generation. A cross-section spline file is pre-generated for each interaction type, each neutrino flavor and each different isotope in the target. As the neutrino flux flows through geometry material, geometry analyzer calculates path lengths through volumes separated by each isotope. The flux driver generates events according to the path length of the neutrinos through the material, the density of material and individual neutrino reaction cross sections. Generated events are written as an output file to be used in detector simulation.

GENIE also provides event reweighting capability. As with the flux, the event reweighting is extremely useful for studying uncertainties due to variations in cross-section models without regenerating Monte Carlo. For example if the axial form factor for quasi-elastic neutrino-nucleon scattering is varied within its uncertainties, this will change the event weight as a function of momentum transfer squared (Q^2).

3.2.1 Physics Models of Signal and Background Processes

Neutrino-electron scattering in GENIE is based on a tree-level calculation [**?**], which is also described in Section 1.3. The low energy term $\left(\frac{m_e}{E_\nu}\right)$ is ignored, which is a small correction for the GeV neutrino energies of MINERvA. A similar reaction,

inverse muon decay ($\nu_\mu e \rightarrow \mu^- \nu_e$) includes 1-loop radiative correction [**?**].

A major background to the neutrino-electron elastic scattering is any process which gives a single electromagnetic particle in the final state. The electron neutrino charged-current quasielastic (CCQE) reactions, $\nu_e n \rightarrow e^- p$ and its anti-neutrino counterpart, are shown in Fig. 3.1. In the MINERvA detector, electrons and positrons are indistinguishable due to the lack of magnetic field. If a recoil proton or neutron is not observed in the detector, which is common at low Q^2, ν_e CCQE events looks like a single EM shower. CCQE in GENIE is based on Llewellyn-Smith model [**?**]. Most parameters of this model are precisely determined in electron scattering, and we used the BBBA2005 [**?**] form factor parametrization of these form factors. However, the nucleon axial form factor, F_A, while precisely known near $Q^2 = 0$, does not have its variation with Q^2 well measured in electron scatering. We assume that Q^2 dependence of axial vector form factor has dipole form,

$$F_A(Q^2) = \frac{1}{\left(1 + \frac{Q^2}{m_A^2}\right)^2},$$
(3.1)

where m_A is axial mass. Under this dipole assumption, other measurements of neutrino CCQE favor a value of m_A=0.99 GeV.

Production of single π^0 in neutral current reactions, $\nu A \rightarrow \nu \pi^0 + \text{recoil nucleus}$, is a background to these single electromagnetic final states. The dominant reactions that produce this final state are the excitation of baryon resonances which decay to nucleons plus pions, and the production of pions from coherent interactions with the nucleus. The coherent pion production mechanism has a smaller cross-section, but it produces energetic forward (small angle with respect to the beam) π^0. Coherent pion production in GENIE is based on the Rein-Sehgal model [**?**]. Pion production
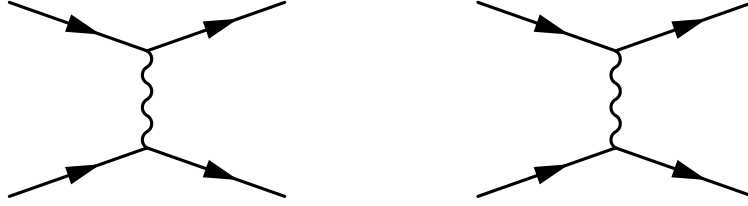
Figure 3.1: CCQE reactions, Left: $\nu_e + n \rightarrow e^- + p$ scattering, Right: $\bar{\nu}_e + p \rightarrow e^+ + n$ scattering

through discrete resonances is based on another model by the same authors [?] for $W < 1.7$ GeV. The Bodek-Yang (modified DIS) model [?] is used to simulate the continuum production for $W < 1.7$ GeV of pions that do not go through a baryon resonance.

All these reactions build from an approximation where the target is a single neutron or proton inside the nuclei. The kinematic modification of this target nucleon is simulated by a relativistic Fermi gas (RFG) model for exclusive processes. In the deep inelastic scattering region region, the reaction rate is modified as a function of Bjorken x based on the ratio of the structure function F_2 on nuclear targets to free nucleons in electron scattering. At low x, this modification as referred to as shadowing; near $x \sim 0.1$ is a behavior called "anti-shadowing"; $0.1 < x < 0.7$ has a suppression of the cross-section referred to as the EMC effect for the experiment that discovered it; and at $x > 0.7$, the Fermi momentum of the target causes a large increase in the cross-section.

Hadrons from neutrino-nucleon interaction may reinteract within the nucleus though a series of processes which are collectively referred to as final state interactions (FSI). For example, $\pi^- p \rightarrow \pi^0 n$ reaction inside the nucleus changes both the

momentum and the charge of a final state pion. Intranuclear rescattering is handled by INTRANUKE/hA model. Hadrons are stepped through the nuclear environment, with a complete simulation of nuclear density, to determine the probability of an interaction at each step. Many different types of interactions are considered whose rates in the simulation are based on measurements of hadron-nucleon scattering: elastic scattering, pion or nucleon charge exchange, inelastic production of pions and absorption of pions.

3.3 Detector Simulation

The MINERvA simulation and analysis are based on the GAUDI framework [**?**]. GAUDI provides a framework layer for detector simulation, which utilizes GEANT4 internally. The GENIE event record does not carry beam timing information. Each event time is randomly distributed according to the Main Injector bunch time structure before being handed to the GEANT4 detector simulation.

3.3.1 GEANT4 Physics Models

The GEANT4 physics model is configurable depending on situation and demand. Electromagnetic interactions use the default GEANT model. The QGSP BERT model [**?**] is used for the hadronic interaction model. A complete "physics list" of GENAT 4 parameters is found in Appendix B.

3.3.2 Geometry Description

The first step of detector simulation is defining detector geometry. The detector geometry consists of shape definitions, material definitions, placing daughter volumes
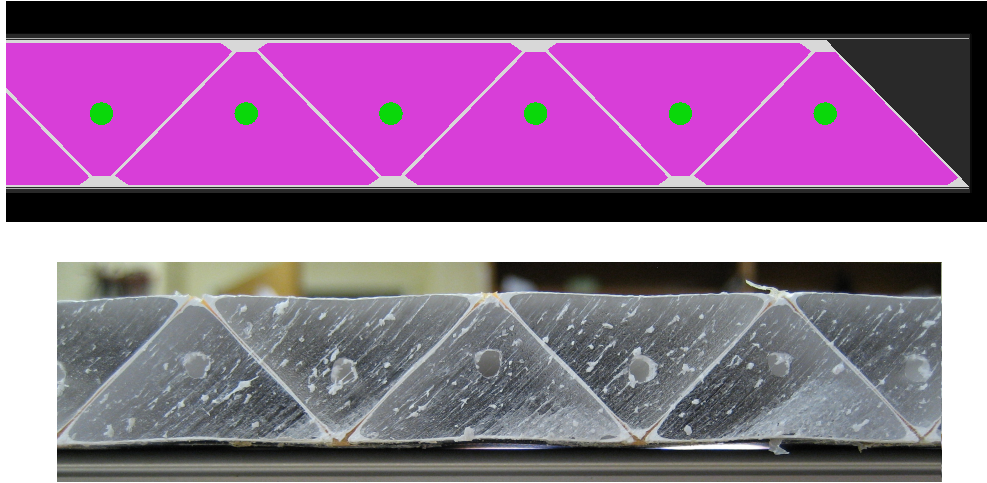
Figure 3.2: Top: Shape of scintillator strips with a fiber hole and rounded corners in simulation (green: WLS fiber, purple: scintillator, white around scintillator: titanium dioxide capstocking material), Bottom: Cross section of an actual scintillator plane

inside mother volumes, and placement of replicas when the geometry is repetitive. Since most of the MINERvA detector is made from the same module, only a few definitions of shapes are necessary. One highly reused volume, the hexagonal scintillaltor plane, has a pretty complicated shape. The fiber hole and the rounded corner of triangular scintillator strip are implemented as shown in Fig. 3.2. The three kinds of module for Tracker, Ecal, and Hcal have slightly different absorber configurations.

Editing and validating the detector geometry is aided by the detector visualization software as shown in Fig. 3.3. MINERvA's GEANT4 simulation is based on the platform of the LHCb detector simulation [**?**], which provides a wrapper for GEANT4. The geometry is defined based on XML[3], which has several advantages. In paticular, modification of geometry does not require recompilation of simulation

---

[3]eXtensible Markup Language
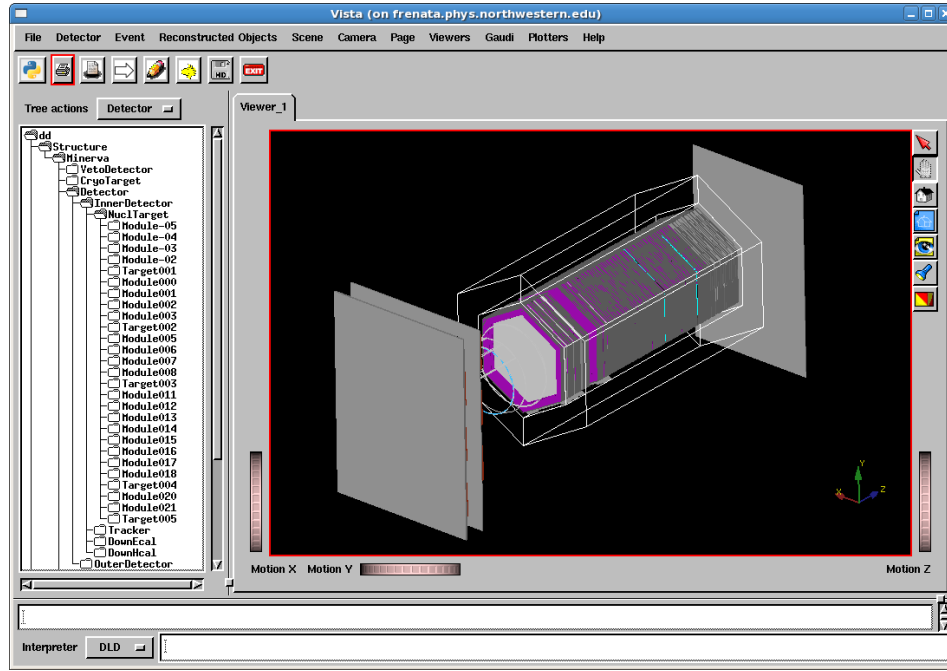
Figure 3.3: MINERvA detector in Vista (Detector visualization software)

code. The XML geometry is given by a set of XML files, which are organized hierarchically. A component in an XML file can access to another component from a different XML file via a reference link. The flexibility of the XML structure allows a slightly different detector configuration to be studied without signifiant duplication of geometry coding.

As discussed in Section 3.2, the same geometry definition is needed for GENIE event generation. Neutrino interaction will be generated based on density of materials and kinds of nuclei. XML geometry is converted to GDML geometry by the GDML writer application, which is a special mode of detector simulation. GDML geometry is then converted to ROOT geometry, which is the format that the GENIE simulation uses.

3.4   Readout Simulation

The raw output of a GEANT4 simulation result is a collection of true energy deposition with coordinates where the energy loss happened in the detector. The particle detector usually consists of active components and inactive components. MINERvA uses scintillator strips as active detector components. Important inactive detector components are Ecal and Hcal absorbers. GEANT4 does not know the exact mechanism of particle detection, it only simulates particle interactions with material when particles travel through the detector volume. Active components are declared as active detectors to GEANT4 so that it may store hit information from these volumes for further readout simulation. MC hits from all scintillator strips are serialized into a list without association to originating volume. Geometric calculation is performed to find the originating strip from (x, y, z) coordindates of the MC hits. Energy deposition in the strip is converted into light in the scintillator proportional to the deposited energy. Light propagation through a WLS fiber is simulated using a measured attenuation curve that was measured from Module Mapper.

In order to find the correct electronics channel that is connected to the strip, a detector strip to electronics channel map is used. This map combines the complicating mapping of clear fiber cables to PMTs and the PMT pixel weave. The number of photoelectrons produced in the photocathode follows Poisson statistics based on the amount of arriving light. The PMT simulation includes the measured optical crosstalk probability that the photon lands on a part of the photocathode which feeds a neighboring PMT dynode. Signal smearing during the dynodes amplification is also simulated, and the response of the electronics is also simulated to produce the equivalent "raw" detector data for the simulation. This "raw" simu-

lated data can then be run through all the same calibration and data processing steps as the real data.

3.5   Overlay with Data

The simulation can be made more realistic when MC events are overlaid with actual data. Multiple neutrino interactions occur per beam spill, and the probability of this is simulated based on Poisson statistics. There are also upstream neutrino interactions that produce particles in the detector, especially rock muons.

Effects of the electronics deadtime are also simulated based on the overlaid activity in the detector. Neutrino interaction in the detector or rock muons may produce deadtime or cause hit overflow, so the following neutrino interaction of interest may not make all hits recorded in the detector. If the region of dead time is near the interaction vertex, the event reconstruction cannot be reconstructed with correct vertex. Such an event will not be used for analysis. If the neutrino interaction overlaps with the previous neutrino interaction or rock muon without dead time, event reconstruction may be obscured by the overlapping. Such effect can be simulated from single interaction MC.

The approach of overlaying real data is chosen because simulating overlapping events from MC itself is complicated. Since the event overlap strongly depends on the time spead of the neutrino interaction recorded on electronics, an accurate model of hit time distribution from detector and electronics is necessary. A realistic hit time model is difficult to due to lack of an accurate model for detector components and electronics. For example, the photon propagation in the irregular inner boundary of the scinitllator strip is not well known. And the noise and after-pulse model in the

electronics are not well modeled. Besides detector and electronics models, making a realistic rock muon simulation solely from beamline simulation and rock geometry is also challenging.

To get around these difficulties, single interaction MC event is overlaid with actual data from a randomly chosen beam spill. The data-MC overlay allows a mimic of realistic deadtime and hit overflow from multiple interactions and event overlapping in the MC sample. Since we are only interested in data hits that are near the MC interaction time, only data hits within 50 ns of the hits from the MC simulated event are considered. The reason to use the latest MC hit time in this calculation is that the interaction may have delayed activity like a Michel electron. Data-MC overlay steps are shown in Fig. 3.4. MC hits that cannot be recorded in the electronics due to deadtime from the data guide are masked as hidden and not used for normal reconstruction. Data-overlaid MC sample is prepared for run period using data from that corresponding run period for the overlay to take into account time variation of running conditions.
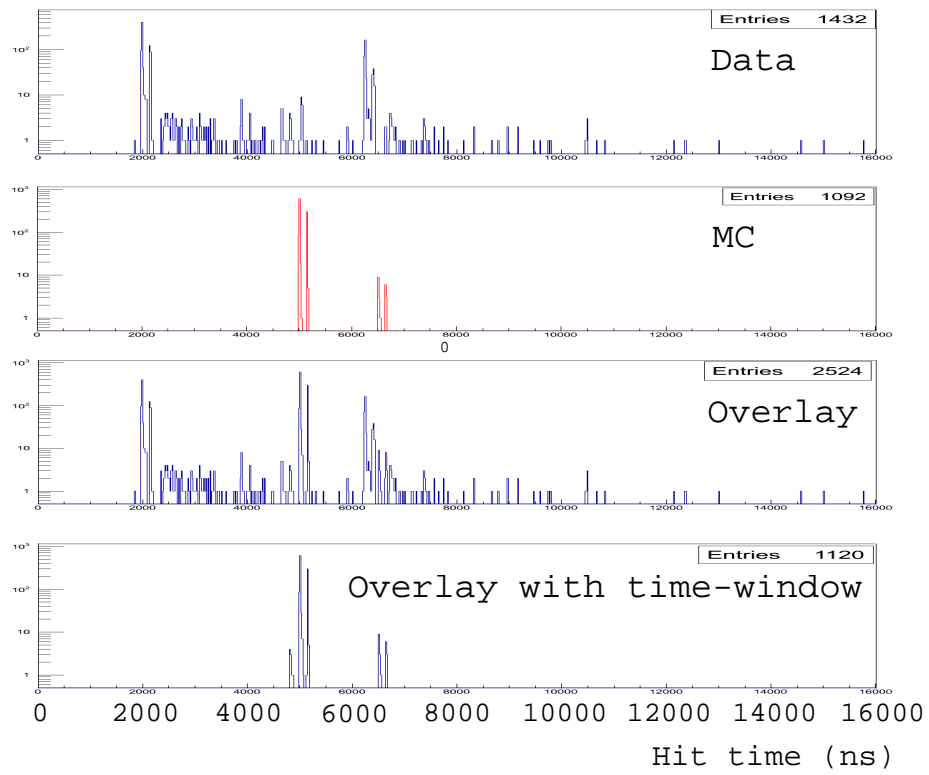
Figure 3.4: Data–MC overlay. Figure taken from [**?**]

Chapter 4

Reconstruction

4.1 Event Reconstruction

As the name implies, the event reconstruction takes the signals from active components of the detector and generates analyzable quantities that correspond to the neutrino interaction that happened in the detector. A neutrino from the NuMI beamline is invisible until it makes a neutrino interaction in the detector. If a neutrino interaction happens, the interaction originates in the middle of the detector during neutrino beam spill time. A neutrino interaction typically produces several particles from the event vertex, which then travel through and interact with the detector materials.

All particle detectors are based on aspects of the electromagnetic interaction between a traversing particle and the medium. The sensitive part of the MINERvA detector is plastic scintillator. When passing charged particles create ionization in a scintillator strip, the excited polystyrene molecules produce light. The light is absorbed by PPO molecules (primary dopant) and light with a longer wavelength
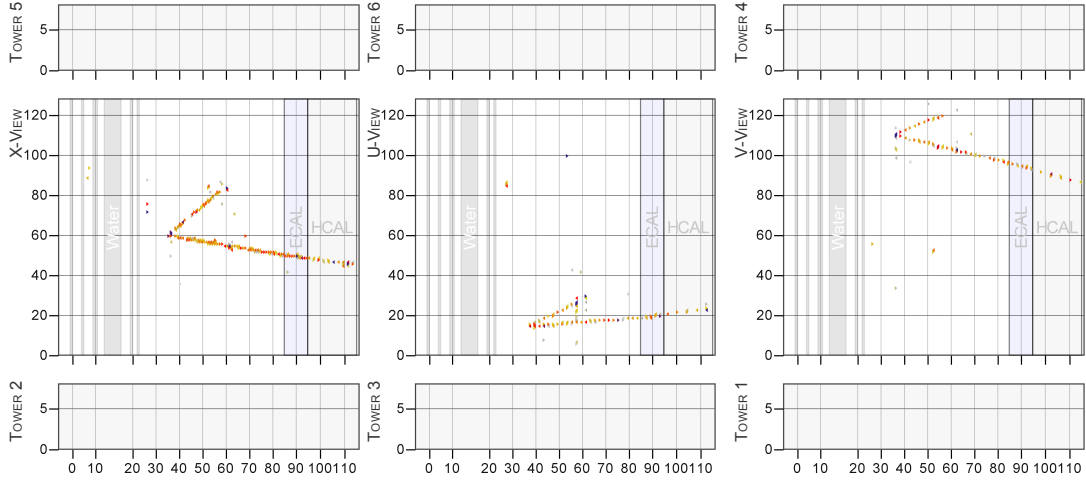
Figure 4.1: Arachne event display. Aspect ratio is not to scale. Neutrino beam is from left to right (left column: X-view, middle column: U-view, right column: V-view).

(UV) is emitted. POPOP (secondary dopant) further wavelength-shifts the light into the blue region of the spectrum. Such wavelength-shifting is necessary to avoid self-absorption, which leads to a very short attenuation length. The produced optical light bounces back and forth in the scintillator strip and some of the light is collected by a so-called wavelength shifting (WLS) fiber. The wavelength-shifted light (now green) in the WLS fiber is transported to a PMT. In the PMT, the photon is converted to photoelectrons and the photoelectrons are amplified to the point that the current can be analyzed by the following electronics. Electric charge and timing of the signal is digitized by the readout electronics. The digitized signal from each strip is called a *hit*. The signal from the detector caused by the neutrino interaction is a collection of *hits* whose energy and time information is measured. Because a *hit* is unambiguously associated with a specific strip, the hit position is also known to be localized within that strip.

If hits from the strips are plotted in strip-module space for each view, the tracks

can be seen visually. A typical two track event is shown in the Arachne event display[1] [**?**] in Fig. 4.1. The three columns in the event display correspond to X, U, and V-views, respectively. Most of the tracks from neutrino interactions travel in the forward direction, which is to say $\ll 90$ degrees from the beam direction. The degree of complexity or multiplicity of event varies depending on the reaction type. A defining feature of ν_μ charged current interactions is the presence of a muon track emanating from the interaction vertex.

The general sequence of reconstruction begins with the easiest part, reconstruction of the muon track. A muon is generally characterized by a thin track passing through the detector. Once the muon track is reconstructed, the reconstruction algorithm can use the reconstructed event vertex, i.e. the start of the muon track, to aid in the reconstruction of the remaining particles. If a muon is not found, the event is most likely a neutral current or ν_e interaction. The reconstruction of muon tracks is done by a series of smaller reconstruction steps, which will be described in the following sections.

4.2 General Reconstruction

4.2.1 Time-slicing

Neutrino interactions can happen throughout the 8 μs beam spill. The number of interactions follows Poisson statistics where the mean number of interactions depends on the neutrino beam intensity. The readout electronics has a multi-buffer memory that allows it to record up to 7 hits for each channel. A collection of hits from each beam spill can contain more than one neutrino interaction, and it

---

[1]A web-based event display
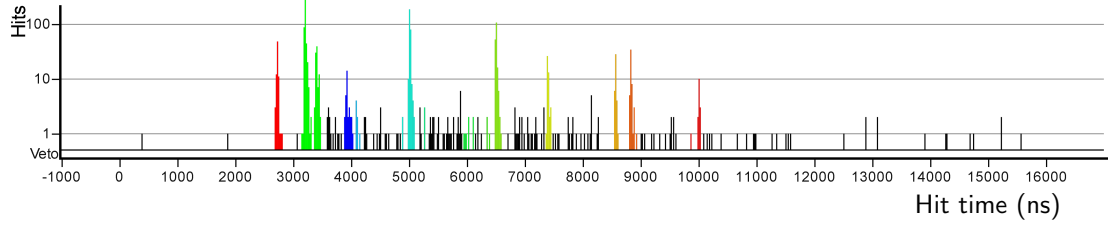
Figure 4.2: Time-slices in a spill. Different color means different time-slice
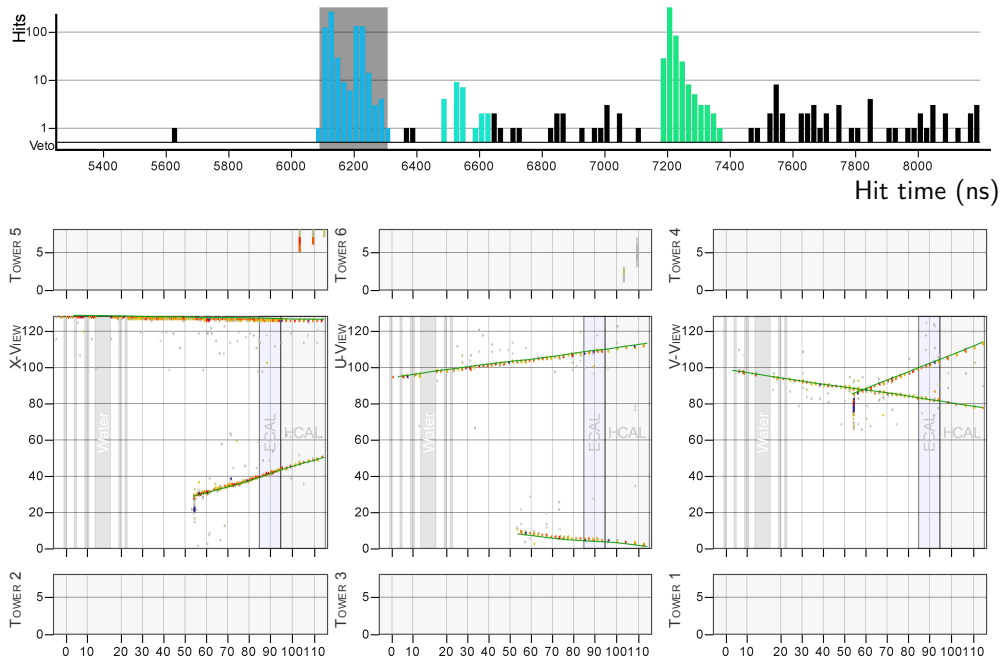
Figure 4.3: Overlapped events in a time-slice. Hit time distribution has two peaks. A neutrino interaction in Tracker and rock muon passing occur at nearly same time.

is necessary to separate these interactions during event reconstruction. The most critical part of the separation makes use of the fact that a single neutrino interaction produces hits throughout the detector over a period of 10-20 ns, which is much shorter than the beam spill time. The division of the hits into shorter time periods is called time-slicing [**?**].

Time slicing relies on the observation that the probability of overlapping 10-20 ns events during a 8 μs beam spill is low. A time-sliced grouping of hits is called a time-slice. The time-slicing algorithm sweeps through time-sorted discriminator-fired hits[2] to find continuous clumps of hits in time. A minimum energy (10 PE) within an 80 ns time-window is required to form a new time-slice. The time-slice keeps growing until the energy in the sweeping time-window becomes below the threshold. Once formed, a time-slice is required to have at least 30 PE, avoiding time-slices with too little energy. Once the time-slices are formed on the basis of the discriminator-fired-hits, non-discriminator-fired hits are included if they are within the time-slice. Fig. 4.2 shows the time-slices in a particular beam spill. Different colors indicate different time-slices.

Generally, one time-slice corresponds to one neutrino interaction; but for some cases the neutrino interaction can have more than one time-slice, for example when it has delayed activity such as the production of a Michel electron from a stopped muon. Associating multiple time-slices for one neutrino interaction is done in a later stage of reconstruction.

Two interactions may occur in the same time-slice as shown in Fig. 4.3. Such occurrences are very rare. The time-slicing is performed only based on hit time information, and events overlapping in time may be split at later reconstruction

---

[2]Hit that passed discriminator energy threshold.
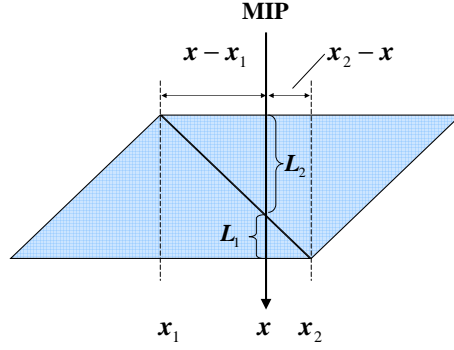
Figure 4.4: Doublet hits produced by MIP

based on pattern recognition in detector space.

4.2.2 Clustering

A muon track or a minimum ionizing particle (MIP) produces a thin track in the detector. When a MIP particle traverses each scintillator plane, ideally it passes through two adjacent triangular scintillator strips. Along the track, it will produce a doublet of hits in each plane as shown Fig. 4.4. The energy deposited in the strip is roughly proportional to the path length of the particle in the strip volume. In the idealized geometry, $\frac{x-x_1}{x_2-x} = \frac{L_2}{L_1} = \frac{E_2}{E_1}$, the transverse position of the track in each plane is calculated as:

$$x = \frac{L_1 x_1 + L_2 x_2}{L} = \frac{E_1 x_1 + E_2 x_2}{E_1 + E_2} \qquad (4.1)$$

where $L_{1,2}$, $x_{1,2}$, and $E_{1,2}$ are path length, transverse position, and energy loss of the strip 1,2, respectively. Charge sharing between two triangular strips provides better position resolution than granularity of strip [?]. Identifying these doublet hits in each plane that are potentially from MIP particles is a useful first step in the

pattern recognition that leads to the reconstruction of muon-like tracks.

In order to handle cases other than doublet hits, general pattern recognition is performed. Hits are grouped together if they are close together in spatial proximity in a plane. Such a group of hits is called a cluster. A cluster is characterized by its size and energy. The size of a cluster is defined as the number of hits in the cluster, and the cluster energy is total energy of the hits assigned to that cluster. Doublet hits are reconstructed as a size 2 cluster. If the energy of the size 2 cluster is consistent with a MIP, then the cluster is classified as *trackable* cluster. If the energy is below minimum MIP energy threshold, it is classified as a *low activity* cluster. If it is above maximum MIP energy, it is classified as a *heavy ionizing* cluster.

A MIP particle does not always produce doublet hits. It often produces a single hit in a plane because the triangular strips have rounded corners as shown in Fig. 3.2. Even if the strip were to have perfectly sharp corners, the energy deposited near the sharp corner can be too small to be detected. Single hit clusters are classified in same way as doublet clusters based on the energy of the cluster.

When multiple tracks are not separated more than a strip width, it produces wider clusters, such as clusters of size 3 or even greater in size. Also very steep angle MIP particles can produce wider clusters because they pass through many adjoining strips in a single plane. Both of these cases are not of particular interest in the first round of reconstruction.

Naively, a size 3 or larger cluster would seem inconsistent with forward going minimum ionizing tracks. However, cross-talk can add hits to clusters, which can result in size 3 or 4 clusters. Because of the checkerboard pattern (Fig. 4.5) of the PMT pixel map, cross-talk hits happen one strip away from original hit. A hit in the i-strip may produce a cross-talk hit at $(i+2), (i-2), (i+8), (i-8)$-strip. Those
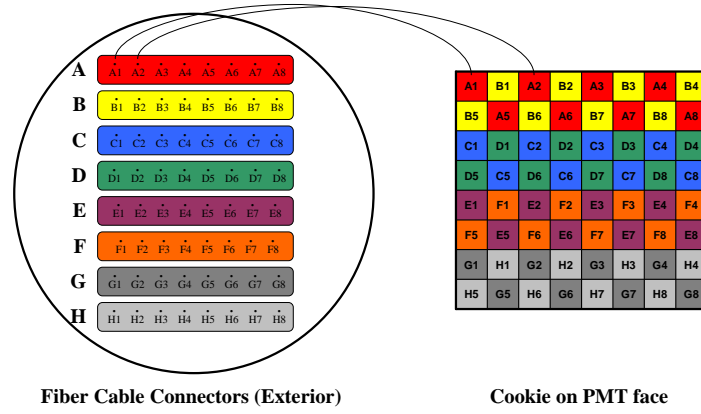
Figure 4.5: PMT pixel pattern
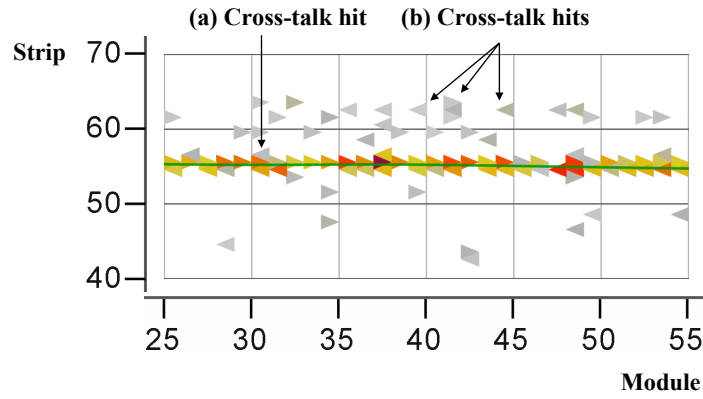
Figure 4.6: Cross-talk hits in a muon track. Low energy hits arey grey.

strip positions correspond to neighboring pixels: up, down, left, and right pixels in the PMT. Cross-talk hits in $(i+8), (i-8)$-strip are easily distinguishable as shown in Fig. 4.6 (b). For a single hit cluster, the cross-talk is not attached to the cluster. But for doublet clusters, cross-talk hits can be connected with the cluster as shown in Fig. 4.6 (a).

Typically, cross-talk hit energy is very low compared to the hit energy of real hits. The hit energy pattern of doublet hits along with a cross-talk hit can be described

by a simple series of symbols like MML where M and L represent the level of the hit energy. Hit energy is classified by (L)ow, (M)ed, and (H)igh based on the energy. A cross-talk hit from a doublet allows for combinations of hit energy such as MML, LMM, MLL, LLM, and LML for size a 3 cluster. But, a trackable cluster excludes MMM, HHH or similar hit patterns inconsistent with doublet and cross-talk. These clusters are classified as heavy ionizing clusters. Note that both hits in a doublet can produce cross-talk hits that are connected to the doublet. Such cases give hit energy patterns like LMML, MMLL, LLMM, LMLL, LLML, MLLL, and LLLM. If a hit energy pattern of a size 4 cluster is one of these patterns and the cluster energy is consistent with MIP, it is also classified as a trackable cluster.

A heavy ionizing cluster is a cluster that is produced by a single heavily ionizing particle, such as a proton track, that is ranging out and rapidly losing energy. It has to be distinguished from wider clusters produced by distinguishable multi tracks. If a size 3 cluster hit energy pattern is HLH, the cluster likely contains distinguishable multi-tracks. Such clusters are classified as *super* clusters. For a size 4 cluster, if the hit energy pattern is like HLLH or a similar pattern, it is classified as a super cluster. For clusters of size 5 or greater, it is considered to be too wide to be a heavy ionizing cluster. Five or higher size clusters are classified as super clusters.

There is a used/unused flag in each cluster to keep track of usage history throughout the reconstruction. Tracking the usage is important because clusters are consumed only once by a higher level object like a track. This insures that energy is conserved in higher level objects.
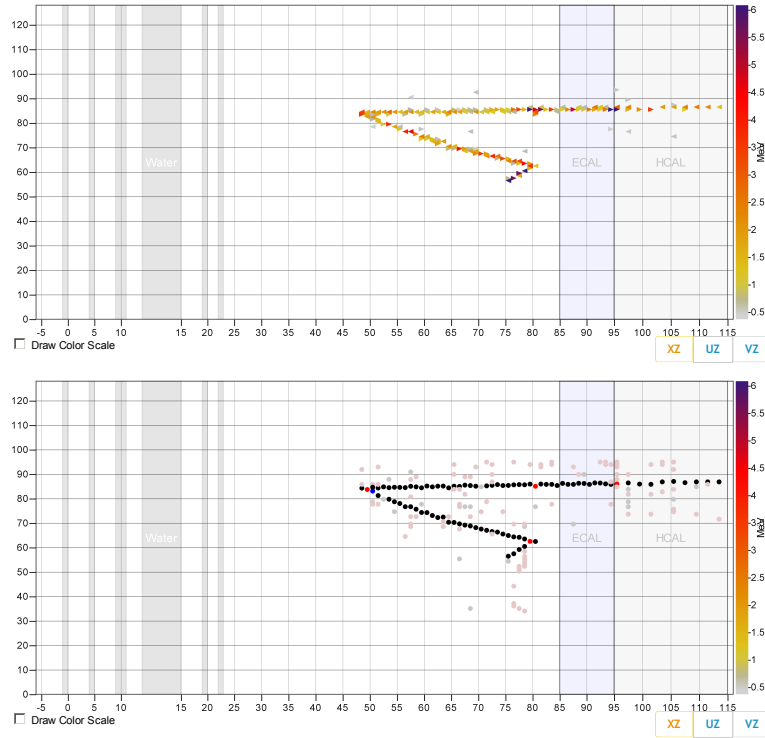
Figure 4.7: Top: Hit map in X-view, Bottom: Cluster view in X-view (black dot: trackable cluster, red dot: heavy ionizing cluster, blue: super cluster, light grey: low activity cluster)

4.2.3 Tracking

In principle, only trackable clusters can be used to find MIP-like tracks. But in reality, muon tracks occasionally produce a δ-ray[3] along the MIP track. δ-rays produce an electromagnetic shower around the MIP track. If only trackable clusters are used, the reconstructed track may be broken near a δ-ray. To mitigate the effect of δ-rays, some heavy ionizing clusters along with trackable clusters are used to find MIP-like tracks. Low activity clusters and super clusters are not used for tracking.

The first goal of the tracking algorithm is to find a 2-dimensional (2D) track

---

[3]a scattered atomic electron from the target

in each view. This is done by finding trackable or heavy ionizing clusters that are lined up along successive planes, to produce tracks like those shown in Fig. 4.7. The first step is to check all possible three consecutive collinear clusters along z in a view. The set of three clusters are called a *track seed*. Collinearity of track seed is checked by its χ^2 to a straight line hypothesis. Adjacent track seeds are merged if the angle between track seeds is small. The merging of track seeds is what produces a track-like object known as a *track candidate*. Track candidates are made for each track seed. Several track candidates may be formed with very similar angles if there are multiple solutions for a set of collinear clusters that only differ slightly because of choice of track seed. Track candidates are merged if they are overlapping or collinear. Merged track candidates are considered to be reconstructed 2D tracks.

The next step is to merge 2D tracks into 3D tracks. If there is more than one track coming out of a vertex, the construction of 3D tracks requires that all possible combinations of 2D tracks between the X, U, and V-views be considered. For each combination, the χ^2 of the 3D track candidates is determined and used as a criterion for selection. Once a 3D track is found, the track direction is fit with a Kalman filter as described below. A reconstructed 3D track is shown in Fig. 4.8.

4.2.3.1   Kalman Filter

Track fitting is a procedure to find track parameters from a series of measurements along a track trajectory. An optimal track fit needs to incorporate the measurement errors and allow for multiple scattering, which requires an inversion of large covariance matrix. A Kalman filter [?] is an iterative method for track fitting that provides a computational advantage because it only needs a small size matrix inversion. It has been used by many experiments [?, ?, ?, ?, ?]. In the Kalman filter, the
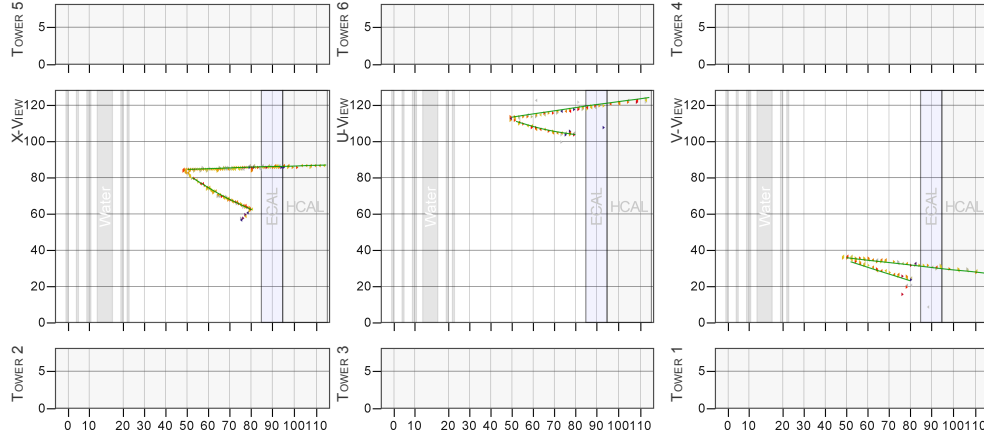
Figure 4.8: Green line indicates reconstructed 3D tracks (From left to right: X, U, V-views).

track propagation along detector elements is described by a discrete linear dynamic system. A state vector, $\mathbf{x_k}$ of 5 parameters, represents the track uniquely at a point in detector

$$\mathbf{x_k} = (x, y, dx/dz, dy/dz, q/p), \tag{4.2}$$

where x, y, z are spatial coordindates, q is charge of particle, p is momentum of particle, and k is an index of discrete z position. The fit node in each scintillator plane is represented by a state vector. The state vector, $\mathbf{x_k}$, in one point is predicted by a linear system from the state vector, $\mathbf{x_{k-1}}$, in the previous point,

$$\mathbf{x_k} = \mathbf{F_{k-1} x_{k-1}} + \mathbf{w_{k-1}}, \tag{4.3}$$

where $\mathbf{F_{k-1}}$ is the track propagator and $\mathbf{w_k}$ is process noise, i.e., multiple scattering. The state vectors are not measured coordinates in the detector. They represent a track that we are trying to fit. The measurement at k is given by a linear function
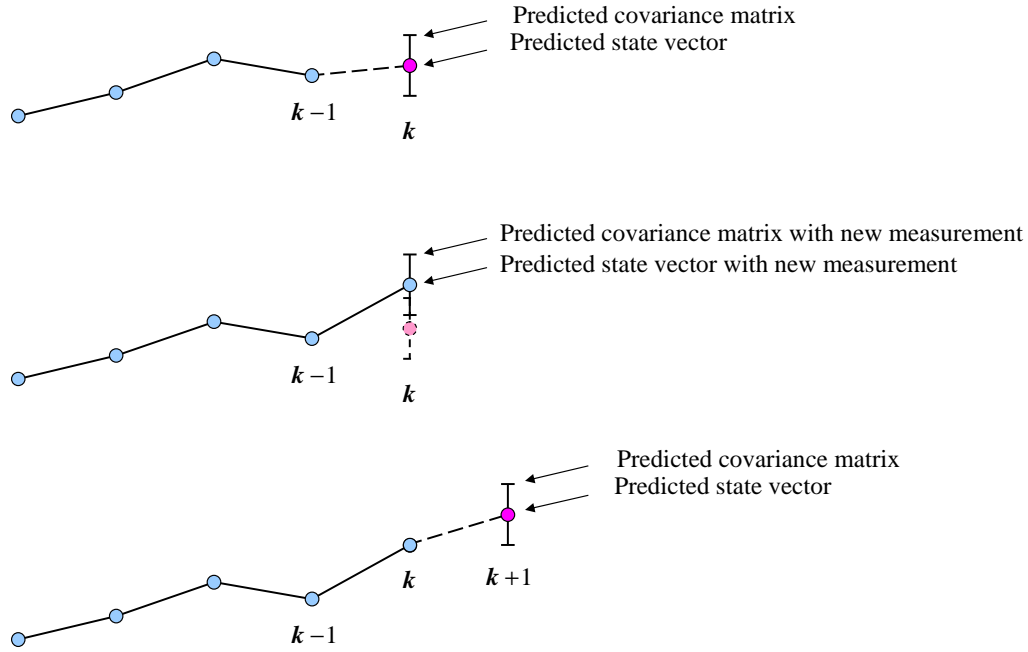
Figure 4.9: Kalman filter iteration

of the state vector.

$$\mathbf{m_k} = \mathbf{H_k x_k} + \epsilon_\mathbf{k} \tag{4.4}$$

where $\epsilon_\mathbf{k}$ is measurement noise. It is assumed that the process noise and the measurement noise are uncorrelated Gaussian distributions with zero mean value.

Three key tasks in a Kalman filter are *filtering*, *prediction*, and *smoothing*. *Prediction* is the prediction of the state vector at a future measurement. *Filtering* is the prediction of current state vector using previous measurements. *Smoothing* is the prediction of the previous state vector with a new measurement in addition to previous measurements.

The initial walk through a track iterates prediction and filtering at each scintillator plane, as shown in Fig. 4.9. After completing the initial forward walk to the track end, the algorithm walks back performing the smoothing step. At each

iteration, the prediction and filtering also estimate a covariance matrix to account for multiple scattering, which depends on material between two positions [**?**].

4.2.4   Blobbing Algorithm

Track reconstruction is just one of the reconstruction steps necessary to prepare the data for analysis. Electromagnetic (EM) showers and small localized energy deposits will not be reconstructed by the tracking. EM showers, hadronic showers, and very short tracks have to be reconstructed by algorithms other than the tracking. Blobbing is used to handle non-track type event reconstruction. Blobbing is an intermediate step for further higher level pattern recognition. In principle, blobbing can be done in several ways for each specific situation. Typical cases that are defined are *dispersed blobs, vertex blobs, and isolated blobs.* Sometimes other types are used depending on the specific needs.

A *dispersed blob* is a simple grouping of unused clusters everywhere in the detector excluding a reconstructed muon track. A dispersed blob is useful for calculating a simple visible recoil energy sum in a charged current inclusive analysis and is also useful for calorimetric energy calculations.

A *vertex blob* is useful for calculating visible energies like a small proton stub around a primary vertex. Vertex energy is calculated from the vertex blob, which is a key parameter for studying CCQE events and their backgrounds.

For electromagnetic showers, *isolated blobbing* provides constituent objects for further higher level pattern recognition algorithms, such as the shower cone algorithm. An isolated blob is a group of hits that are spatially isolated and have a good 3-dimensional (3D) matching between X, U, and V-views. *Isolated blob* formation is done in two stages. First, 2-dimensional (2D) isolated blobs are created. Then

the 2D blobs are grouped further between the X, U, and V-views if they match between three views. For 2D blobbing, clusters are separated by sub-detectors and then by views. The clusters in a view are sorted by the cluster energies. 2D blob formation is seeded by highest energy clusters. The second highest energy cluster is the second seed and so on. 2D blob formation loops over all the clusters letting seeds grow if adjacent clusters are close. If two growing seeds are close enough, they will be merged to produce a bigger seed. 2D blobbing is complete when there is no more possible growth or merging of blobs. A three dimensional triplet is formed from a combination of X, U, and V-view 2D blobs if the three views are consistent. The energy centroid of 2D clusters is given by the energy weighted z and transverse coordinates. Because an EM shower in one view can be broken into two pieces in z while the other views have only a single blob, XUV matching does not require z-centroid matching between three views. It only checks if they overlap in z. The transverse coordinate of energy centroid is checked to verify XUV matching of the 3D isolated blob.

4.3   Electron Reconstruction

4.3.1   Shower Cone and Seeding

An energetic electron traverses about a radiation length as a MIP until it begins to shower. The radiation length, X_0, in the Tracker is about 42 cm, which corresponds to 25 scintillator planes when the direction of the electron is normal to the planes. The track-like part of an electron shower can often be reconstructed as a track. This track serves as the core for shower cone seeding as shown in Fig. 4.10. In order to apply the shower cone algorithm, the start position and direction of the shower

have to be known. The shower cone angle is chosen to collect most of the hits that are associated with the shower. Even though the seeding track is 3-dimensional, the shower cone is applied in 2D, i.e., in the X, U, and V-views. If more than one track is available, the more upstream track will be used first as a shower cone seed. Occasionally, an electron starts to shower early and the MIP track is too short to be reconstructed as a track. In such a case, an isolated blob will be used for shower cone seeding. The most upstream isolated blob is used for shower cone seeding as shown in Fig. 4.11. The direction is determined from a fit to the shower cone seeding isolated blob. If the most upstream isolated blob is too short, and the direction of the isolated blob seed does not give a reasonable direction for the shower cone, the next upstream isolated blob will be used as a shower cone. This procedure continues until the shower cone algorithm succeeds in creating a shower or there are no more available isolated blobs. In the case where the most upstream small isolated blob is skipped for the seeding, the shower axis of the reconstructed shower cone is traced back in the upstream direction to check if the small Isolated blob is on the shower axis. If the small blob is on the axis, the shower start position is moved back to the small blob, and shower direction is determined from the small blob and the reconstructed shower cone.

The shower cone shape is shown in Fig. 4.12. The sharp corner of the cone is clipped to surround the interaction vertex smoothly. Referring to Fig. 4.12, the cone shape parameters that are used are the cone offset (50 mm), the cone opening width (80 mm), and the cone opening angle (10 degrees).
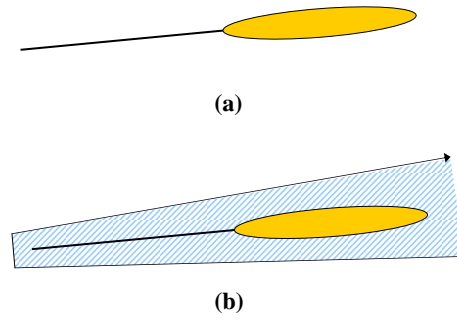
Figure 4.10: (a) Electromagnetic shower with beginning of shower reconstructed as a track (b) Track seeded shower cone
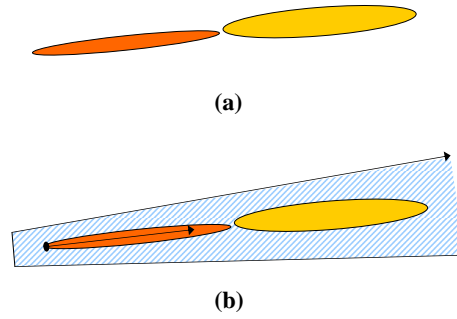
Figure 4.11: (a) Electromagnetic shower with beginning of shower reconstructed as a Isolated blob (b) Isolated blob seeded shower cone
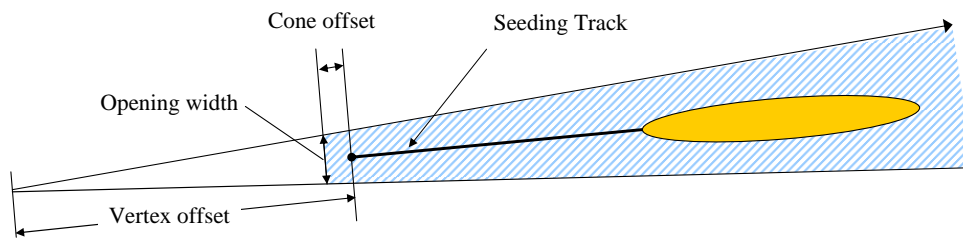
Figure 4.12: Shower cone shape and cone shape parameters

4.3.2 Energy Reconstruction

The energy in a shower cone is calculated calorimetrically. The calorimetric energy is the sum of calorimetric energies in each sub-detector computed with each sub-detector's corresponding calorimetric constant as shown in Eqn. 4.5

$$E = \alpha(E_{\mathrm{T}} + k_{\mathrm{E}}E_{\mathrm{E}} + k_{\mathrm{H}}E_{\mathrm{H}}), \tag{4.5}$$

where E_{T}, E_{E}, and E_{H} are the visible energies in the Tracker, Ecal, and Hcal, respectively. α is a scale factor and k_{E}, and k_{H} are the Ecal calorimetric constant and Hcal calorimetric constant, respectively. k_E and k_H compensate energy loss in passible absorber in the Ecal and Hcal, respectively. The scale factor, α, compensates for energy loss in the inactive materials in each scintillator plane such as the WLS fiber, capstocking material, lexan wrapping, and epoxies. Low activity clusters, which are often after-pulse noise or cross-talk hits, are not included in the calorimetric energy calculation.

Calorimetric constants were determined by a MC study. For example, α was determined from events generated using an electron particle gun MC with a semi-infinite size[4], and a Tracker-only geometry. The scale factor was calculated from the ratio of the true energy to the visible energy ($\alpha = E/E_{\mathrm{T}}$). Similarly, from MC with a semi-infinite Ecal-only geometry, the Ecal calorimetric constant was calculated from $k_E = E/(\alpha E_{\mathrm{E}})$, where α comes from the procedure mentioned above. MC with a semi-infinite Hcal-only geometry is used in a similar fashion to calculate the Hcal calorimetric constant. When the Ecal and Hcal calorimetric constants are calculated, low energy events (E<0.5 GeV) are not used to calculate the ratio

---

[4]Detector is large enough so the shower is fully contained

because the calorimetric constant has a nonlinear behavior at low energy. MC-based calorimetric constants are summarized in Table 4.1.

Parameter	Value
α	1.326
k_E	2.341
k_H	9.54

Table 4.1: Calorimetric constant values

The side-Ecal has not been taken into account in Eqn 4.5. If a hit is known to be in the Side-Ecal region as shown in Fig. 4.13 (a), it can be treated in same way as the downstream Ecal. But the x-y position of a hit is often ambiguous, particularly when part of electromagnetic shower is located in Side-Ecal. Thus, the Side-Ecal calorimetric energy calculation only relies on hit strip position. If the hit is from strip 1-10 or 118-127, it is certainly a Side-Ecal hit. The C hit in the X-plane in 4.13 (b) will be recognized as a Side-Ecal hit, but the same position will not be recognized as a Side-Ecal hit in the following U or V-planes as in 4.13 (c) and (d). Since plane orientation follows XUXV pattern, hit C will be treated as a Side-Ecal hit twice in four planes as shown in Table 4.2. Hit B in the V-plane in 4.13 (d) will be recognized as a Side-Ecal hit but not in the X or U-planes. Hit B will be treated as a Side-Ecal hit only once in four planes as shown in Table 4.2. Hit D in the U-plane will be treated similarly as hit B in the V-plane.

If a hit is from strip 1-10 or 118-127 in the X-view, it is necessary to compensate the missing Side-Ecal energy in the U and V planes. The energy calculation without a correction is $\alpha(k_E e_1 + e_2 + k_E e_3 + k_E e_4)$, where the energy deposited in the 4 planes (XUXV) are e_1, e_2, e_3, and e_4, respectively. The energy deposited in each of the 4 planes are approximately the same, so $\alpha(k_E e_1 + e_2 + k_E e_3 + k_E e_4) \approx 2(k_E + 1)e$.

(a) Side-Ecal hits   **(b) X-plane**

(c) U-plane   **(d) V-plane**
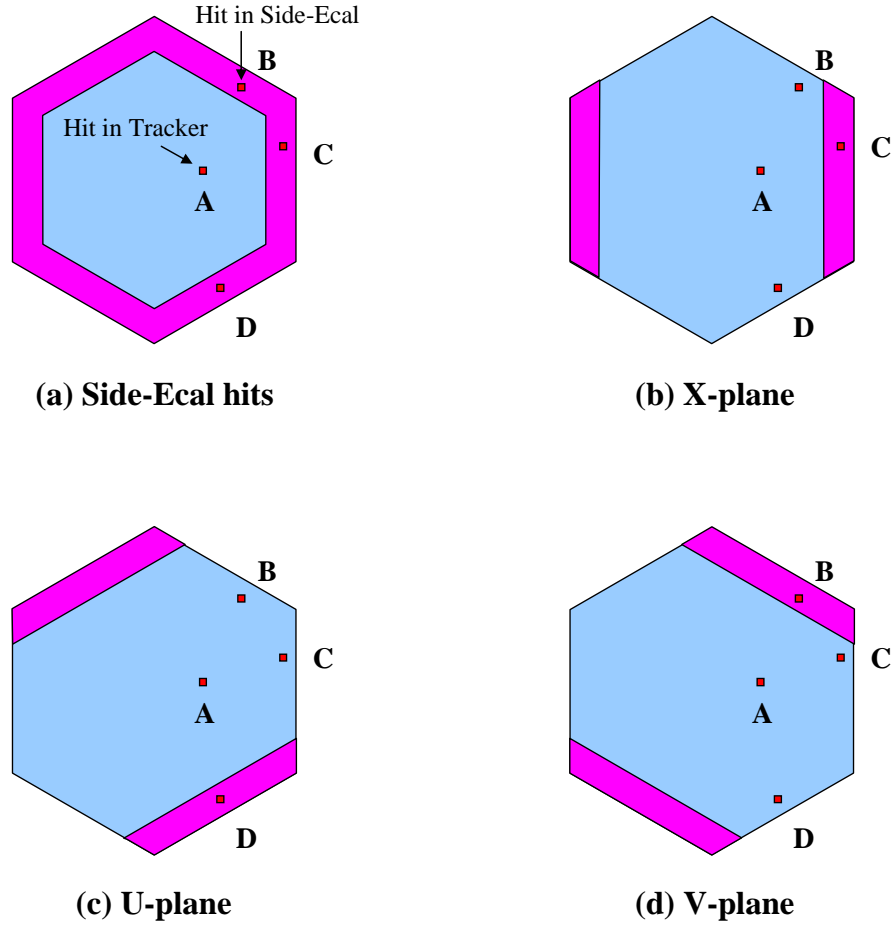
Figure 4.13: Various hit positions (B, C, and D) in Side-Ecal and calorimetric energy calculation based on only strip position

	B	C	D
X-plane		■	
U-plane			■
X-plane		■	
V-plane	■		

Table 4.2: Side-Ecal hit energy reconstruction in 4 planes without x-y position reconstruction. Filled squares represent hits recognized as Side-Ecal hits based on the hit strip position in the plane. Hit positions B, C, and D are defined in Fig. 4.13.
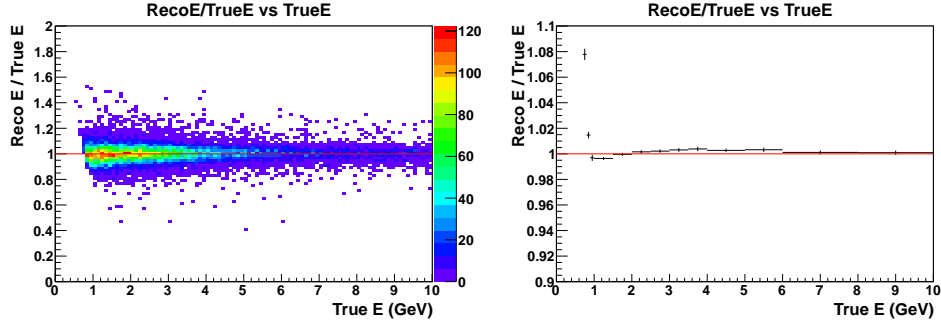
Figure 4.14: A check of the calorimetric energy reconstruction and energy scale

Ideally, the correct form is $4k_E e$. Thus, the missing amount is $4k_E e - 2(k_E + 1)e = 2(k_E - 1)e$. Similarly, a compensation factor for the U or V-plane is $2(k_E - 1)e$. In summary, the calorimetric energy calculation with Side-Ecal is given by:

$$E = \alpha \left[E_T + k_E E_E + (2k_E - 1)E_{SE}^{\text{X}-\text{view}} + (4k_E - 1)E_{SE}^{\text{U,V}-\text{view}} + k_H E_H \right] \quad (4.6)$$

where $E_{SE}^{\text{X}-\text{view}}$ is the visible energy in side-Ecal for X-view plane, and $E_{SE}^{\text{U,V}-\text{view}}$ is the visible energy in side-Ecal for U or V-view plane, respectively.

The energy reconstruction of a simulated ν-e scattering events sample is shown in Fig. 4.14. The signal sample passes all the cuts used for the final event selection in the analysis part of this thesis. The event selection will be described in the Analysis Chapter. Note that the energy scale is flat over the entire energy range.

The reconstructed energy vs. true energy is shown in Fig. 4.15 (left). The energy dependence of the energy resolution is shown in Fig. 4.15 (right). The energy dependence of the energy resolution will not follow conventional calorimetric behavior exactly because the vertex z position varies within the fiducial volume, and the fraction of the energy in the Ecal affects the energy resolution. The low energy point is not on the fit line because the shower does not reach the Ecal. The
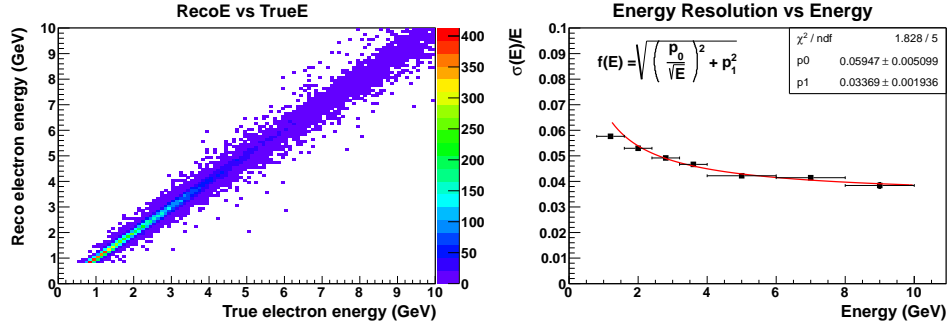
Figure 4.15: Left: reconstructed energy vs. true energy, Right: Energy resolution vs. energy

energy resolution of a shower fully contained in Tracker will be better than one reconstructed in the mixed calorimetry of Tracker and Ecal.

4.3.3 Direction Reconstruction

The accurate direction reconstruction of the electron shower is critical to the rejection of background using $E\theta^2$ for $\nu e \to \nu e$ elastic scattering. The fit nodes and energy centroids of the scintillator planes are fed into the Kalman filter. The use of all fit nodes from the electron shower does not necessarily give the optimal shower direction fit. The beginning of an electron shower is a narrow MIP-like track, which represents initial electron direction well, but the showery part is wider in transverse size, and the transverse energy distribution can be asymmetric due to shower fluctuation. The energy centroid deviates significantly from the shower axis near the end of the shower, where the shower diminishes gradually. Also, occasional heavy bremsstrahlung can give off shower axis energy deposits near shower max position. The direction is fit using up to the first 30 fit nodes. The Kalman filter is used for single particle fitting. The electromagnetic shower is not a single particle once the
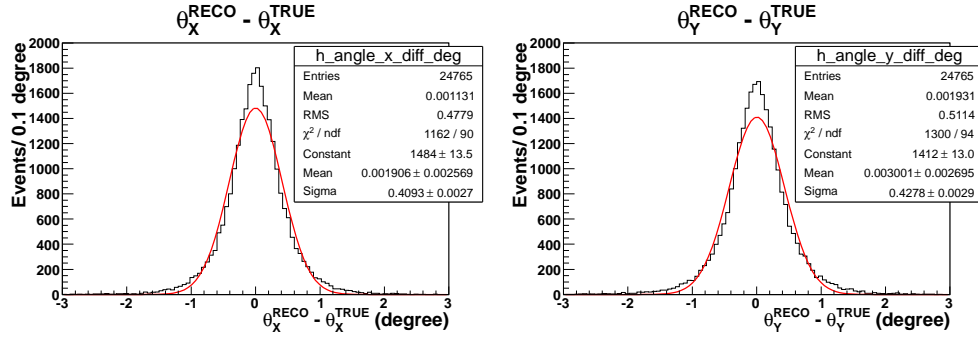
Figure 4.16: Left: x angular resolution, Right: y angular resolution

electron starts to shower. However, the charged showering particles travel collinearly because the detector is not magnetized. So, the showering particles are treated as a single particle collectively using the energy centroid positions. The Kalman filter was used with the single electron assumption. In other words, the particle mass parameter in Kalman filter was set to the electron mass. The fit of the Kalman filter will be best at the beginning of shower, and this is used to represent the initial electron direction.

Fig. 4.16 shows the angular resolution of a signal only sample. The angular resolution is represented by the angle residual in each x and y direction. The y angular resolution is slightly worse than the x angular resolution due to the X, U, and V plane orientation and XUXV plane configuration. The x direction is solely determined by X-planes, while the y direction is determined by combining U and V-planes. Angle residual vs. energy is shown in Fig. 4.17. Angular residual in each energy band in Fig. 4.17 is fitted with a Gaussian function. Angular resolution from the Gaussian fit is plotted as a function of energy in Fig. 4.18. Angular resolution is better at higher energy.
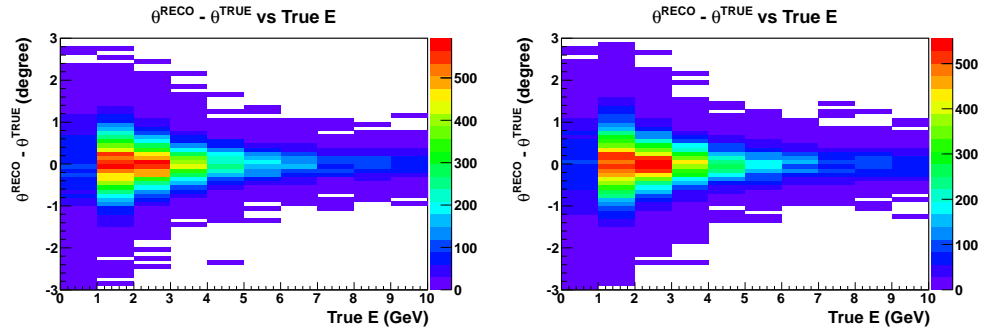
Figure 4.17: Left: x-angle residual vs. energy, Right: y-angle residual vs. energy
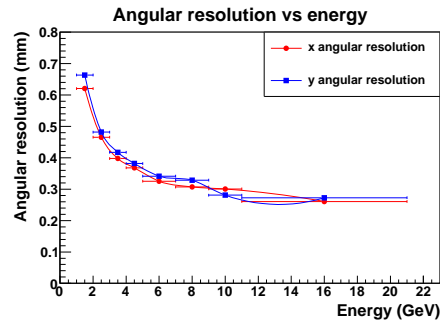
Figure 4.18: Angular resolution vs. energy

Chapter 5

Analysis

5.1 Data Sample

Table 5.1 summarizes the protons on target (POT) of all subsets of the low energy (LE) forward horn current (FHC or neutrino mode) data. To qualify as useful data for analysis, data must meet certain quality requirements. The primary proton beam position and various other primary beam and secondary beam conditions, such as the focusing current in the horns, are monitored during neutrino beam operation. Analysis requires that the neutrino beam is in expected state, so that the POT counting and the beam flux prediction based on that counting are reliable. The MINERvA DAQ status is also required to be good; otherwise data from the detector may not be reliable. Good status of the MINOS near detector is generally necessary for analysis of the ν_μ charged-current reactions that dominate our observed reactions, so that muons that exit from the back of the MINERvA detector can be reconstructed. Because this analysis does not require muon reconstruction using the MINOS near detector, approximately 8% more data where the MINOS detector was

not functioning can be added to the analysis. The total usable data for this analysis integrated 3.53×10^{20} POT.

Playlist	Reco POT (Total)	Reco POT (Good Beam)	Reco POT (Good Beam, Good DAQ)	Reco POT (Good Beam, Good DAQ, Good MINOS)
1	1.01E+20	9.85E+19	9.85E+19	9.59E+19
7	7.73E+18	7.26E+18	7.26E+18	6.65E+18
9	6.80E+18	6.80E+18	6.80E+18	6.78E+18
13A	1.52E+19	1.51E+19	1.51E+19	1.28E+19
13B	3.69E+19	3.65E+19	3.65E+19	1.79E+19
13C	1.32E+20	1.30E+20	1.30E+20	1.28E+20
13D	6.41E+18	6.39E+18	6.39E+18	6.37E+18
13E	5.26E+19	5.24E+19	5.24E+19	5.12E+19
Total	3.58E+20	3.53E+20	**3.53E+20**	3.26E+20
Frac to Total	100.00%	98.64%	98.64%	90.91%

Table 5.1: Protons on target (POT) summary of low energy (LE) forward horn current (FHC) data, processed by event reconstruction (Reco), Playlist is a period of data-taking, that is separated by a change of detector configuration, neutrino beam configuration, or neutrino beam target.

A small fraction of the data, $\approx 3\%$, was lost in the final data processing due to failures in the data handling and the reconstruction algorithms at processing time. Therefore, the sample available for event selection is reduced slightly to 3.43×10^{20} POT.

5.2 Event Selection

In order to maintain high efficiency for single electron signal events, the shower cone based event reconstruction is applied whenever a viable seed is found as described in the previous chapter. Because of this, the raw output of the reconstructed shower does not necessarily represent a good reconstruction, particularly for background

events and events originating outside the tracker region of the detector. To ensure that the reconstructed shower cones are consistent with electrons originating from the Tracker detector, requirements on the location vertex of the shower cone and quality of the reconstruction are necessary.

First, these are basic event selections, or "cuts":

- fiducial event selection

- E > 0.8 GeV

- plausibility cut (only MC).

Then, the analysis applies the following event selections for reconstruction quality:

- neighborhood energy cut

- reduced chi squared

- bending angle < 9°

- consistent energy among X, U and V views ("energy balance")

- maximum transverse RMS among X, U, and V views

- shower end z position

- shower end transverse position (TPos)

- Ecal-Hcal visible energy asymmetry

- deadtime cut.

Most of the reconstruction quality cuts keep the signal event with very high efficiency (~99%).

After these initial cuts, several cuts are introduced in order to remove rare event topologies in which events that are not single electromagnetic showers can appear similar to the signal events:

- upstream energy cut

- number of transverse energy peaks in Ecal ≤ 1

- shower transverse RMS at first 1/3 of shower

- longitudinal energy profile

- non-trackable cluster fraction in the Tracker.

Finally, we apply the most important selections, which remove photons and electrons at an angle too large to be consistent with neutrino-electron scattering, respectively:

- Mean dE/dx (plane 1-4) < 4.5 MeV/1.7cm

- $E\theta^2 < 0.0032$ and Q^2 (CCQE) < 0.02

These selections are described in detail in the following sections.

5.3   Basic Analysis Cuts

5.3.1   Fiducial Volume

The fiducial volume is defined by a hexagon with an apothem 88.125 cm whose outer boundary is therefore 4 cm away from the inner boundary of the side-Ecal. A
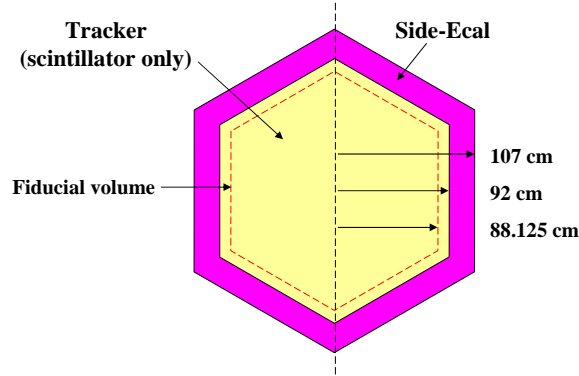
Figure 5.1: Fiducial volume as viewed from the direction of the beam

z-view of the Inner Detector is shown Fig. 5.1. The most upstream two modules in the Tracker are excluded from the fiducial volume to remove interactions from the Nuclear target region which is not comprised of scintillator and has different detector response for electromagnetic showers. The most downstream four modules in the Tracker are excluded from the fiducial volume in order to have at least four module track length in Tracker so the reconstructed shower has good angular resolution before it enters into Ecal. The top view of the Inner Detector with highlighted fiducial volume is shown in Fig. 5.2. The total mass of detector within the fiducial volume, which is proportional to event rate, is about 3 metric tons.

5.3.2   Minimum Energy Cut

The energy of electron candidates is required to be greater than 0.8 GeV because of very high background at lower energies, mostly resulting from photons from π^0 decays. The event reconstruction is also more challenging for lower energy electrons. In particular, particle identification of low energy electrons becomes more difficult because the electron does not have sufficient energy for bremsstrahlung and subse-
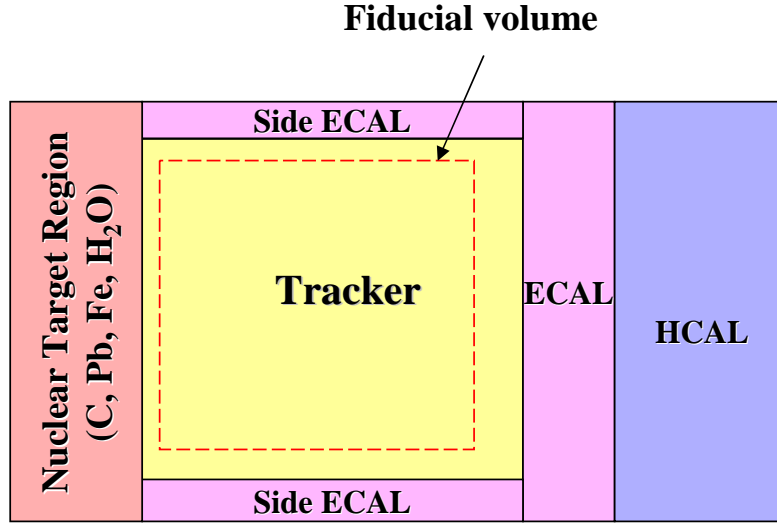
Fiducial volume

Figure 5.2: Fiducial volume as viewed from above, shown as red dashed line within Tracker region. The outer detector is not shown for simplicity.

quent photon e^+e^- pair production processes to cause the particle multiplicity to rise as the electron traverses the detector. In this case, electrons are too similar to particles which merely lose energy by ionization and leave straight tracks in the detector. Another pathology of low energy electrons is that they often create showers with gaps along their longitudinal development due to hard bremsstrahlung. When a hard bremsstrahlung photon carries most of the energy from an electron, the shower becomes invisible in the detector until the bremsstrahlung photon undergoes pair production. Since the gappiness in the electromagnetic shower is unique, it could serve as particle identification for low energy electron. These shower gaps are not used in this study, but they could be used to allow extension of the energy threshold to lower energies, albeit at low efficiency.

5.3.3 Plausibility Cut

Data-overlay in MC is used to mimic overlap of multiple interactions and deadtime of electronics. Some MC events will become unanalyzable due to the event overlap or deadtime as a result of event overlap, and the simulation successfully reproduces such occurrences. However, it is possible that neutrino-electron scattering events *from overlaid data* can be reconstructed as a MC event even if the true MC interaction is some other reaction that happens outside the fiducial volume. Because the MC analysis relies on the simulation itself generating the candidate event, this is not a genuine MC event for the purposes of this analysis. For a given reconstructed event in MC sample, it can be either a genuine MC event or an overlaid data event or even possibly a mixture of both. Because it is a MC simulation and we have full knowledge of the event, we can determine what fraction of energy in a reconstructed event is from MC hits. Genuine MC and overlaid data are well separated in MC energy fraction, with genuine simulated events almost always having a very high MC energy fraction, so such mixed events are very rare. Events in the MC sample are required to have more than 50% of their electron shower energy from the MC event.

5.4 Reconstruction Quality Cuts

5.4.1 Neighborhood Energy Cut

Since each signal event is a single electron, the reconstructed candidate event should be a well isolated shower with little other nearby activity. In principle, a sum of all the energy outside the shower cone could be used to ensure a singlel electromagnetic
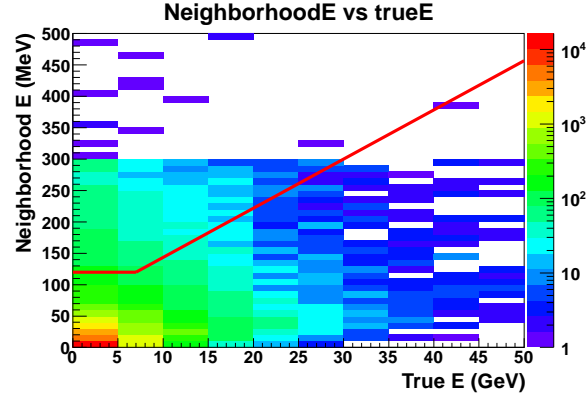
Figure 5.3: Neighborhood energy vs. true electron energy for simulated events, with the selection requirement shown as the region below the red line

(EM) shower, but this quantity is maximally sensitive to overlapping energy from pileup in the detector, which can lower the cut efficiency. Therefore only nearby, "neighborhood", energy to shower cone is used to check if an EM shower is isolated. The neighborhood is defined as a region within 5 cm of the outer boundary of the shower cone. Energetic electrons can produce a shower which is slightly wider than the cone. To maintain good efficiency at high energy, the neighborhood energy cut is loosened linearly above the electron shower cone energy of 7 GeV. The neighborhood energy cut, shown as the red line in Fig. 5.3, is

$$
\text{Neighborhood energy}
\begin{cases}
< 120 & \text{if E} < 7 \text{ GeV} \\
< 7.82609E + 65.2174 & \text{if E} > 7 \text{ GeV}
\end{cases}
. \tag{5.1}
$$

5.4.2 Reduced Chi Squared Cut

The direction of the electron shower was reconstructed assuming the beginning of the electromagnetic shower behaves like a single particle, which was described in

Section 4.3.3. The Kalman fitter produces a χ^2 statistic describing the quality of the fit to this underlying model of a single particle. The reduced chi squared, χ^2/degree of freedom does not follow the expected χ^2 distribution because the single particle hypothesis is not correct. However, high values of this parameter are highly correlated with events where the fitted direction of the electromagnetic shower is misreconstructed due to a poor fit. In particular, some classes of background events will contain multiple particles in the cone and will not be well represented by a single straight shower. For such events, the χ^2/NDF of such background event will be larger than the electron shower, and they can be removed by the very loose requirement that χ^2/NDF < 100.

5.4.3   Bending Angle Cut

High energy electromagnetic particles produces a shower that follows a straight line in the same direction of the initial particle, since typical transverse momentum exchanged by bremsstrahlung or pair-production reactions is of order m_e. In particular, a large fluctuation of the transverse direction in the early stages of a true electromagnetic shower is very rare, and when this does happen, it is often correlated with the "gappy" behavior described above. By contrast, hadronic interactions impact transverse momenta of order m_π, and so often appear bent along their path. The bending angle of a shower is measured by drawing segments between the shower start point, its end point and the midpoint as shown in Fig. 5.4. The angle between A-M and M-B is measured. In some cases with a large kinked path, the shower cone will not contain the entire kinked track. However, this metric is almost always sufficient to identify such events.
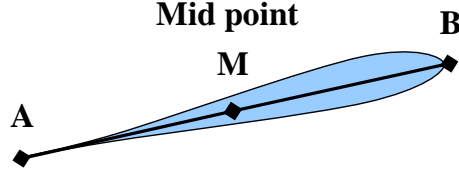
Figure 5.4: Bending angle of shower

5.4.4 Energy Balance between Views

Since scintillator plane configuration follows XUXV pattern, on average, the electromagnetic shower will deposit 50% of its energy in the X-view and 25% of its energy in the U- and V-views. Energy balance between three views can be expressed as two conditions $E_x - E_u - E_v \approx 0$, and $E_u - E_v \approx 0$. For background events with multiple particles, energy balance is not guaranteed within the shower cone, as illustrated schematically in Fig. 5.5. Thus, energy balance cut will be useful to reject misreconstructed events. Energy balance metrics are formed by

$$E_{XUV} = \frac{E_x - E_u - E_v}{E_x + E_u + E_v} \text{ and} \tag{5.2}$$

$$E_{UV} = \frac{E_u - E_v}{E_u + E_v}, \tag{5.3}$$

and these quantities are used to select events with

$$|E_{XUV}| < 0.28 \text{ and } |E_{UV}| < 0.5. \tag{5.4}$$

These requirements were designed to be highly efficient for signal events.
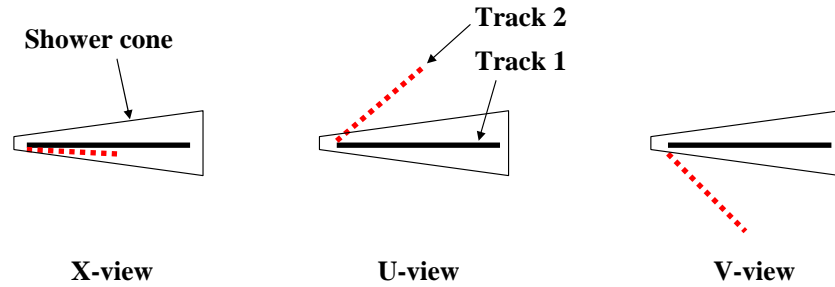
Figure 5.5: Example of energy imbalance between X, U, and V views

5.4.5   Maximum Transverse Spread among X, U, and V-views

Once a track is formed from a shower cone, the energy-weighted mean residual distance of clusters from the shower axis was calculated to determine the transverse spread of energy from the shower axis. Electromagnetic showers from a single electron will have a greater spread in this variable than is expected from single minimum ionizing particles. However, background events where this larger transverse size is actually because of nearly overlapping tracks, will tend to have a larger transverse spread than electron showers. When two particles overlap in the shower cone with a small opening angle, it is possible that in one view the two tracks may accidentally overlap giving a small transverse spread in that view. However, if the transverse energy spread is calculated in each view, the maximum value among three views will be affected by the opening angle between the two overlapping tracks. By contrast, a single electromagnetic shower will have approximately the same transverse spread in all three views. Thus, the maximum root mean squared (RMS) of transverse residual among three views has sensitivity to distinguish two track background events.

We calculate

$$(\text{RMS of transverse residual})_{\text{x-view}} = \left[\frac{1}{E_{\text{x-view}}} \sum_{i,\text{x-view}} (\Delta t_i)^2 e_i \right]^{1/2} , \qquad (5.5)$$

where $E_{\text{x-view}} = \sum_{i,\text{x-view}} e_i$. This quantity is required to be < 65 mm to reject events with two or more overlapping tracks in the shower cone.

5.4.6 Shower End Z Position

The most downstream ("end") position of an electromagnetic shower in the MINERvA detector gives a handle to reject some types of background events. Even the most energetic electromagnetic showers will not penetrate far into the Hcal with its 1 inch steel absorbers, regardless of how close the shower begins to the downstream end of the detector. This is because electromagnetic shower loses most of its energy in Ecal (≈ 8 X_0), and so the remaining showering particles cannot reach too deep into the Hcal. The outlying case for true electromagnetic showers is where the end of the shower has a high energy photon that can, by bad luck, traverse a few modules in the Hcal before pair production of an e^+e^-, which at these energies will typically result then in only hits in the next one or two downstream Hcal modules. Therefore, it is desirable that the definition of the shower end point should not be sensitive to such straggling low energy photons.

The shower end position is then defined so that it is the most downstream hit in a triplet of planes, one in each view, all with hits, which is not longer in extent than five consecutive modules. If a triplet candidate is more than five modules in extent, then the most downstream hit of that triplet is ignored, and the next most upstream triplet is considered until the five module criterion is met.

The shower end, defined in this way, is required to be between module 70, in the Tracker and module 112, near the upstream end of the Hcal.

5.4.7   Shower End Transverse Position

Events in the fiducial volume where the electron candidate has a large angle with respect to the z-axis may escape out the side of the inner detector. Such events, if the particle is minimally ionizing like a muon, leave very little energy in the side-Ecal before exiting, and the hits in the side-Ecal extend to the edge of the detector. However, if the exiting particle is making an electromagnetic shower, then it leaves significant energy with a typically large transverse energy spread. The transverse position at the end of such a shower is measured by the energy centroid, and because of the transverse spread of energy deposited in such events, the apparent position as the shower exits can be far from the edge of the detector.

Because the Inner Detector is hexagonal, an exiting track should escape through one of six sides, and this means that the track will often only reach the edge of the detector in one view. For example, in the event shown in Fig. 5.6, the two reaches the side of the event display in the U-view, but in the X- and V-views, the track appears to end in the middle of the detector. To measure the proximity to the edge of the detector, the maximum of the absolute value of the transverse position (TPos) from each of the three views is calculated. This is equivalent to the apothem of the minimum side hexagon centered along the detector z-axis that encloses the shower end transverse position. This is required to be less than 105 cm, which is 2 cm from the boundary of the Inner Detector as shown in Fig. 5.6(c).
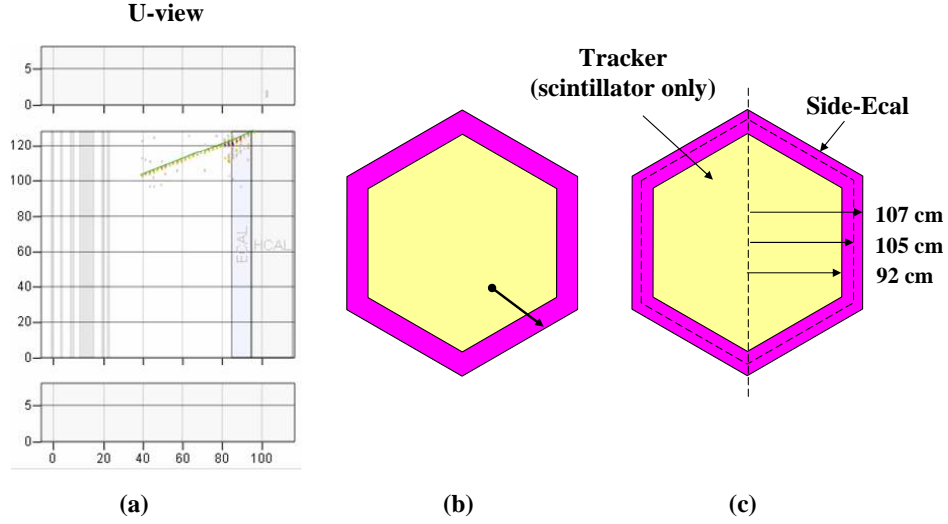
Figure 5.6: Shower end transverse position. (a) An exiting track in event display of U-view (b) Same exiting track seen from z axis (c) Dimension of side-Ecal, shower end transverse position cut and detector boundary

5.4.8 Ecal-Hcal Visible Energy Asymmetry

Whenever an electromagnetic shower reaches to Hcal from an event originating in the Tracker, it has to go through Ecal. Most of the electromagnetic shower energy not deposited in the Tracker should be deposited in the Ecal. We define the energy Ecal-Hcal energy asymmetry as

$$A_{EH} = \frac{\mathrm{E}_{\mathrm{vis}}^{\mathrm{Ecal}} - \mathrm{E}_{\mathrm{vis}}^{\mathrm{Hcal}}}{\mathrm{E}_{\mathrm{vis}}^{\mathrm{Ecal}} + \mathrm{E}_{\mathrm{vis}}^{\mathrm{Hcal}}}. \tag{5.6}$$

$A_{EH} > 0.6$ was required for the selected events.

5.4.9 Dead Time Cut

The data acquisition has some insensitive "dead time" after hits, as described in Section 2.2.6. In order to avoid incorrect reconstruction due to the effect of dead

time, the channels upstream of the start of the reconstructed shower cone are checked to see if these channels are dead at the time of the interaction. If there are such dead channels, then the reconstructed vertex position may be shifted downstream from its true value, and this will have cascading negative effects on the entire reconstruction.

The reconstructed candidate electron track is extrapolated through two upstream modules, or four planes, to find a central strip in each plane. The total number of dead channels on these strips and the adjacent strips in each of the four planes is required to be no more than one.

5.5 Initial Background Rejection Cuts

5.5.1 Upstream Interaction Veto

A neutrino interaction that happens upstream of the fiducial volume may contribute background if its event vertex is misreconstructed. This upstream region includes the Nuclear Target region and material in front of the detector, so it contains significant mass and therefore a large rate of neutrino interactions. As an example, a neutral current interaction with π^0 in the Nuclear Target region could mimic the signal since a photon from the π^0 decay will typically travel through detector about one radiation length without making a track and may produce an electromagnetic shower beginning in the fiducial volume.

Fortunately, such electromagnetic showers point back to the location of an upstream neutrino interaction. The total energy is calculated inside a cylinder of radius 30 cm and whose center axis is the upstream extrapolation of the reconstructed electron candidate track. This energy is calculated in three views. If there is localized activity near the true neutrino interaction vertex, then the z extent of the energy in

all three views should overlap. Each pair of views is checked for such an overlap and deposited energy is only considered in a views if there is such an overlap. Events with all three possible overlaps are rejected if the energy in the overlap region is > 300 MeV.

5.5.2 Number of Transverse Energy Peaks in Ecal

One of main backgrounds is a single photon background from π^0 decay where one of the two photons is not observed. This happens for one of two reasons. Either the energy of one of the photons is very small, or the π^0 is energetic and the two photons are nearly collinear in the original π^0 direction. In the latter case, the two photons may not be reconstructed separately if their opening angle is small. Photons travel a significant distance in the Tracker before interacting, but never more than a very short distance in the Ecal because of the high pair production cross-section in the lead absorbers.

When π^0 decays into two photons with a small opening angle they may both be within the same shower cone, but this does not mean that they are not separated transversely in space. Fig. 5.7 illustrates such a case where two peaks in the transverse projection can be identified within a single shower cone. The event selection looks for such peaks in the Ecal, where the photons lose most of thir energy, and requires only one.

5.5.3 Shower Transverse RMS at First 1/3 of Shower

For an electron, the beginning of the electromagnetic shower does not show significant transverse energy spread because the particle content at the start of the
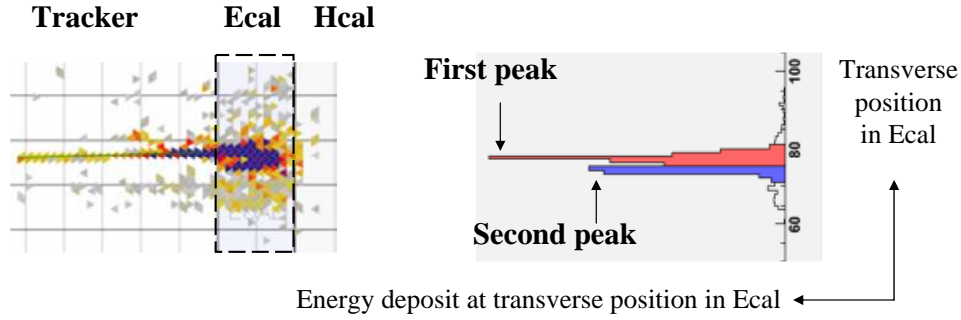
Figure 5.7: Identification of two transverse energy peaks in Ecal. The two peaks are made from two photon showers.

shower is still a single electron until the first hard bremsstrahlung interaction, and the radiation length is more than ten modules in Tracker for electrons in the beam direction. However, background events with multiple particles may have some transverse spread in energy even if they are within the shower cone.

As the shower develops, the electromagnetic shower will eventually show significantly wider transverse distribution near its shower maximum, so the discrimination will not be as useful in this region. Therefore, the transverse energy distribution is calculated at the first one third of the shower in the Tracker region using the method described in Section 5.4.5 but summing over all three views. The energy weighted transverse residual RMS in the first third of the shower in the Tracker region is required to be less than 20 cm.

5.5.4 Longitudinal Energy Profile

An electromagnetic shower has a characteristic longitudinal energy profile determined by the shower cascade processes. When electromagnetic particles such as electron, positron and photon traverse in a medium, they produce electromagnetic

showers via successive bremsstrahlung, $e^{\pm} \to e^{\pm}\gamma$, and pair production, $\gamma \to e^+e^-$ in the fields of the atoms in the target. The number of showering particles increase exponentially like a cascade until the energies of the particles drop below the energies where such multiplicative reactions dominate, referred to as the "critical energy", E_c. The longitudinal energy deposition profile, which is proportional to the number of charged showering particles $(e^{\pm})$ at each point in the shower, follows the same pattern. Electromagnetic shower development is stochastic, but on average the longitudinal energy profile of the shower is given by a photon distribution [?],

$$\frac{dE}{dt} = Eb\frac{(bt)^{a-1}e^{-bt}}{\Gamma(a)}, \tag{5.7}$$

where t is the distance in units of radiation lengths, E is the initial energy and a and b are free parameters that can be empirically determined for each material. In such a distribution, dE/dt reaches its maximum when

$$t_{\max} = \frac{(a-1)}{b} = \ln y + C, \tag{5.8}$$

where $y = E/E_c$ and $C = -0.5$ for electrons and $+0.5$ for photons. The critical energy, E_c, for carbon (Z=6) is 111 MeV according to the following empirical formula,

$$E_c = \frac{800\text{MeV}}{Z + 1.2}. \tag{5.9}$$

For 1 to 10 GeV electrons in carbon, $y = E/E_c$ ranges from 9 to 100. b is nearly constant for a given detector material but has a slight dependence on y [?] that is shown in Fig. 5.8. For y values of 9 to 100, b ranges 0.64 to 0.7 for carbon.
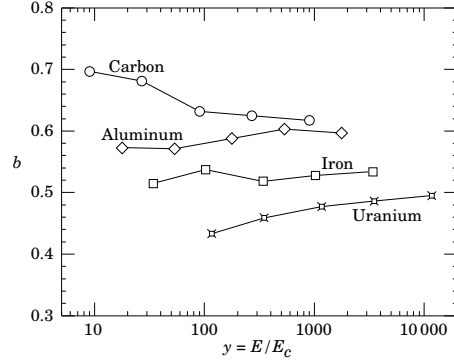
Figure 5.8: y dependence of b parameter (figure taken from [**?**])

The dE/dx value at shower maximum $(t = (a - 1)/b)$ is

$$\left(\frac{dE}{dt} \right)_{\text{max}} = \frac{Eb}{\Gamma(a)} \left(\frac{a - 1}{e} \right)^{a-1}. \qquad (5.10)$$

Define the vertex to shower maximum average slope as

$$\frac{(dE/dx)_{\text{max}}}{x_{\text{max}}} = \frac{Eb}{\Gamma(a)} \left(\frac{a - 1}{e} \right)^{a-1} \frac{1}{t_{\text{max}} X_0} \qquad (5.11)$$

$$= \frac{Eb}{\Gamma(a)} \left(\frac{0.7 t_{\text{max}}}{e} \right)^{0.7 t_{\text{max}}} \frac{1}{t_{\text{max}} X_0}. \qquad (5.12)$$

Therefore, the following quantity is, on average, approximately constant for an energetic electron shower,

$$\frac{(dE/dx)_{\text{max}}}{x_{\text{max}}} \frac{1}{E} \sim \text{constant}, \qquad (5.13)$$

although on an event by event basis, this quantity does vary due to the stochastic behavior of shower development. A low value of this cut means the particle appears minimumally ionizing, like a muon. But a high value is characteristic of background events with overlapping short tracks stopping not too far from the vertex, for exam-
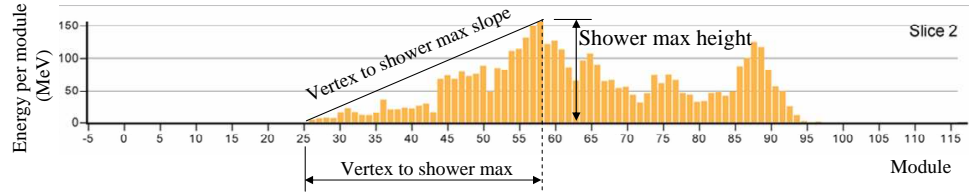
Figure 5.9: Slope of vertex to shower maximum

ple when a non-relativistic recoil proton stops inside the shower cone. We require

$$\frac{(dE/dx)_{\max}}{x_{\max}} \frac{1}{E} < 5. \tag{5.14}$$

Fig. 5.9 shows a typical longitudinal energy profile for an electron shower.

5.5.5 Non-trackable Cluster Fraction in Tracker

A minimum energy of electron candidates of 0.8 GeV is required due to very high background at lower energies. Even with this requirement, most backgrounds are still concentrated between 0.8 and 2 GeV, and therefore extra selection cuts are useful to target backgrounds in this region.

The effectiveness of the particle identification methods depends on the energy of candidate events because the both the longitudinal and transverse size of the electromagnetic shower, and in particle the amount of energy deposited in the Ecal, have a significant dependence on energy. While most of the electrons below 2 GeV do still reach to the Ecal, they often do not deposit sufficient energy in the Ecal to rely on that energy for background rejection. In fact, electrons and charged pions at low energy can be much more easily confused in the Ecal by at lower energies than they can be at higher energy. Because of the small and fluctuating energy in

the Ecal, these extra selection cuts rely on the shower development in the tracker.

The pattern of energy deposited by a charged pion that doesn't undergo inelastic interactions is consistent with a track of a minimum ionizing particle (MIP) in the Tracker. In elastic interactions, which typically make a track the abruptly changes directions, or kinks, are already removed by the reconstruction quality cuts.

When an electron traverses the Tracker, it starts to shower by bremsstrahlung and subsequent pair production of those photons, but because the particle multiplicity is still low, the resulting electromagnetic (EM) shower is slender. However, the overall transverse size of the EM shower is still slightly wider than that of the MIP particle.

The transverse size of the EM shower can be quantified by the different topologies of clusters which are described in Section 4.2.2. For example, these slender EM showers may make a number of three strip clusters before reaching the Ecal, but MIP particles will almost always only create one or two strip clusters, which we categorize as "trackable" clusters, along the track. The fraction of non-trackable cluster in Tracker is used to reject MIP-like track in the Tracker. Useful discrimination is only possible when interaction vertex is in the upstream part of the fiducial volume, so the particle can travel a sufficient distance to begin to shower before it enters into Ecal.

For EM candidates with energy below 2 GeV whose vertex position is not too close to Ecal, with vertex module < 65, the fraction of non-trackable clusters in the Tracker is required to be < 0.05 to reject MIP-like tacks.

5.6   Final Background Rejection Cuts

5.6.1 γ/e Discrimination by dE/dx

Energy loss of charged particles from ionization, often referred to as dE/dx, is often an excellent particle identifying discriminant as a particle passes through material. Not only is this energy loss the effect of many small interactions, typically ionizing thousands of atoms per gram/cm^2, and therefore less subject to stochastic fluctuations, it also depends strongly on momentum as the particle slows down from ultra-relativistic and therefore the pattern of dE/dx as the particle stops is sensitive to its mass.

Electromagnetic (EM) particles are generally clearly distinguishable from heavier hadronic particles which constitute some of our backgrounds because ionization dE/dx of electrons and positrons is larger than that of hadrons. In addition, as electrons pass through matter, an EM shower cascade is developed via successive processes of bremsstrahlung photons and pair production of these photons. Photon initiated shower development is shown schematically in Fig. 5.10. Note that the photon is not visible in the detector until it creates charged particles by pair production, or undergoes Compton scattering from atomic electrons. At high energies, the pair production dominates, and the mean free path of the photon is $\frac{9}{7}X_0$, where radiation length, X_0, in the Tracker is about 50 cm. If the interaction vertex is known, for example, by a muon track from ν_μ CC reaction, and an EM shower starts some measurable distance from the vertex and the shower direction points back to the vertex, it is almost certainly due to a photon.

In the case of neutral current single π^0 production, the only visible particles in the event may be the photons from the π^0 decay. In some cases, one of the two
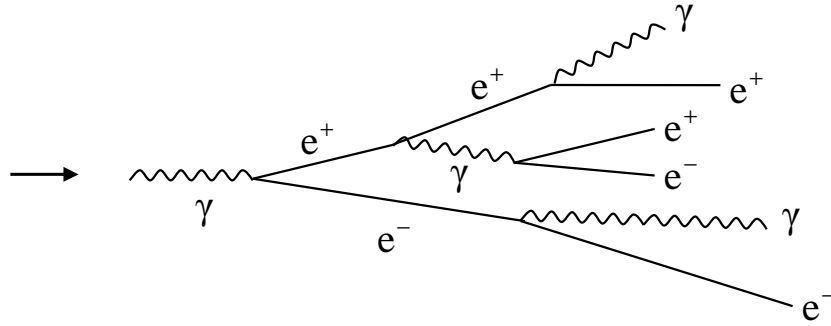
Figure 5.10: Beginning part of photon-initiated electromagnetic shower

photons may not be observed in the detector because it is low energy, and it can look like a single EM shower. Also, when the produced π^0 is highly relativistic, i.e., high energy, the decay of π^0 may produce two photons with a very small opening angle. With the small opening angle, these two photon showers can nearly overlap and appear like a single EM shower. Since the photon shower development processes are very similar to an electron shower, it can mimics the signal.

However, a photon and an electron have an important difference at the beginning of the shower. When an electron traverses in the detector, it initially loses energy due to ionization[1] until the multiplicative processes in EM shower development increase the shower multiplicity. The most common first step in a photon shower for energies above 10 MeV is pair production of e^+e^-, and thus the start of a photon shower typically has twice the dE/dx of what is seen in electron showers. As the EM shower cascade develops, the number of particles increases and dE/dx continues to increase and become more influenced by the stochastic fluctuations in shower development. Therefore, it is advantageous to calculate dE/dx near the beginning of shower to separate electrons and photons. But if too few planes are included in the calculation,

---

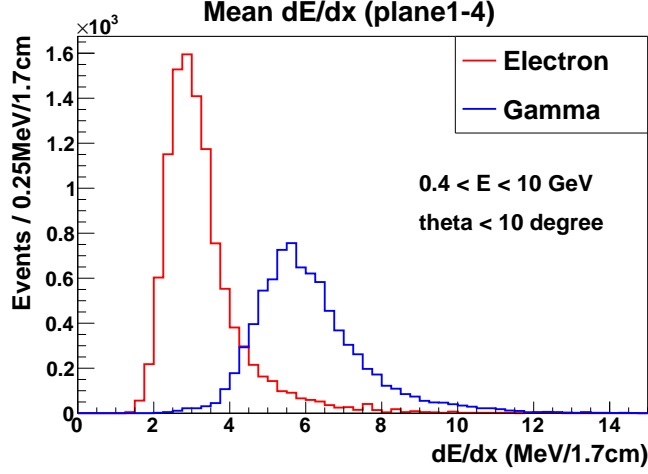[1]See appendix C for the electron energy loss in scintillator

Figure 5.11: MC dE/dx comparison between electron and photons. For these samples, the energy of both the electrons and photons is randomly generated between 0.4 GeV and 10 GeV with a uniform angle with respect to the detector z-axis between 0 and 10 degrees. The units of dE/dx are given as MeV/1.7cm because the dE/dx is calculated from $dE/$(dplane), and the scintillator plane thickness is approximately 1.7 cm.

the dE/dx has broad distribution due to variation of the vertex position within the first scintillator strip and due to the energy resolution in the detector. Increasing the number of planes included in the sum decreases these smearing effects. Measuring the dE/dx over first 4 scintillator planes is found to be a good choice for optimal discrimination. We define the mean measured energy loss

$$\langle dE/dx \rangle_{1-4} = \frac{1}{4} \sum_{\text{plane } i=1}^{4} dE_i \times \cos\theta, \qquad (5.15)$$

where dE_i is energy deposited in the i-th plane and θ is the angle of shower in detector coordinates.

$\langle dE/dx \rangle_{1-4}$ of the Monte Carlo simulated electron and photon samples are compared in Fig. 5.11. Electron and photon $\langle dE/dx \rangle_{1-4}$ have a peak near 3MeV/1.7cm

and 6MeV/1.7cm, respectively, and indicate a good discrimination between electron and photon showers is possible. $\langle dE/dx \rangle_{1-4} < 4.5$ MeV/1.7cm is required for this analysis.

Other experiments plan to use this technique in the future to discriminate electrons from photons in neutrino interactions. For example, MicroBooNE [?] will use the same technique, which utilizes good energy resolution of LAr TPC[2], to study the particles responsible for the MiniBooNE excess of EM showers at low energies [?]. A similar technique will be used in the LBNE oscillation experiments to reduce backgrounds to ν_e appearance.
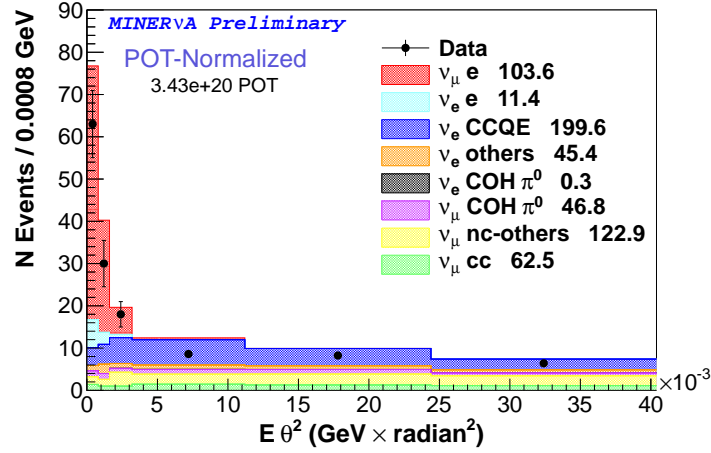
5.6.2 $E\theta^2$ Cut

With the dE/dx selection removing most of the backgrounds from photons, the remaining major background is from ν_e CCQE, $\nu_e n \rightarrow e^- p$ and $\bar{\nu}_e p \rightarrow e^+ n$. If the recoiling nucleon is not observed in the detector, which is common at low Q^2, the final state is a single electron or positron. The MINERvA detector does not distinguish electron from positron due to lack of magnetic field. Even though ν_e content of the neutrino beam is only about 1%, the ν_e CCQE background is potentially very large because the neutrino electron scattering cross-section is factor of 2000 smaller than neutrino nucleon scattering.

Since the observable particle content is identical, no particle identification requirement can reject ν_e CCQE background directly. However, neutrino electron scattering can be separated using a kinematic constraint which is derived in Appendix A,

$$E\theta^2 < 2m_e, \tag{5.16}$$

---

[2]Liquid argon time projection chamber

Figure 5.12: $E\theta^2$ distribution before applying $E\theta^2$ cut

where E is electron energy, θ is theta angle of the electron with respect to the neutrino beam direction, and m_e is electron rest mass. The CCQE background, in which the target is a nucleon, can have values of $E\theta^2$ up to $2m_N$, where N is the mass of the target nucleon. The $E\theta^2$ cut was previously used by the CHARM II experiment to measure the weak mixing angle from ν-e scattering [**?**].

Fig. 5.12 shows the $E\theta^2$ distribution of candidate events after all event selections are applied except the $E\theta^2$ cut. The signal event are peaked at very small $E\theta^2$ value. Note that the signal peak is much wider than $2m_e \approx 1$ MeV due to the angular resolution of the event reconstructed.

$E\theta^2 < 0.0032$ GeV radian^2 is applied for ν-e analysis. After the $E\theta^2$ cut, an electron spectrum is obtained as shown in Fig. 5.13.

5.6.2.1 Q^2 (CCQE) Cut

The $E\theta^2$ cut removed ν_e CCQE background effectively at low energy, but this cut is less effective for high energy electrons because the electrons from CCQE also
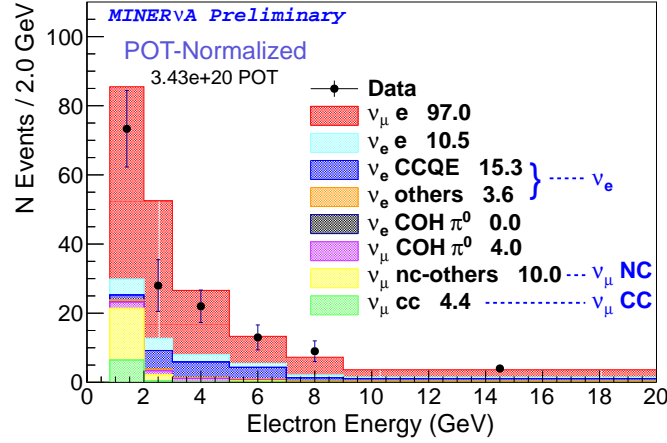
Figure 5.13: Electron spectrum after final cut (before background tuning)

are observed at smaller angles at higher energy, so that the angular resolution becomes more important. As a secondary cut, Q^2 is reconstructed directly under the assumption of ν_e CCQE kinematics,

$$E_\nu = \frac{m_n E_e - m_e^2/2}{m_n - E_e + p_e \cos\theta}, \tag{5.17}$$

$$Q^2 = 2m_n(E_\nu - E_e), \tag{5.18}$$

where E_ν is neutrino energy, E_e is electron energy, p_e is electron momentum, m_e is electron mass, and m_n is neutron mass. $Q^2(\text{CCQE}) < 0.02$ GeV^2 is required to reject high energy electron from ν_e CCQE. This is a small addition to the existing $E\theta^2$ cut and is also only a function of the electron angle and energy. Therefore, for the purposes of showing the effects of cuts, it is lumped together with the $E\theta^2$ cut.
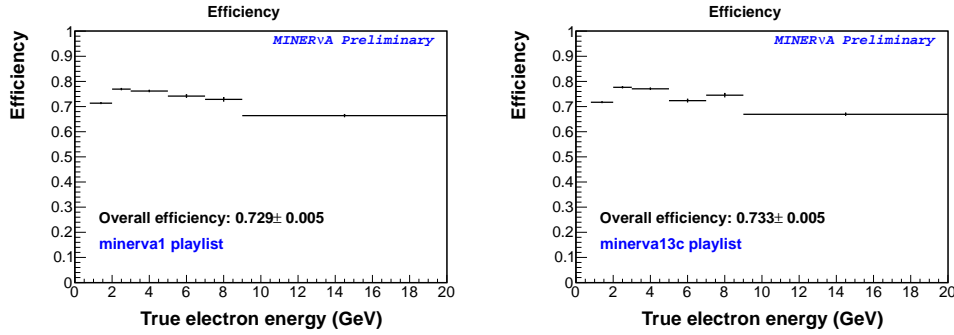
Figure 5.14: Efficiency as a function of true energy. Signal MC sample for each playlist was overlaid with corresponding playlist data (Left: minerva1 playlist, Right: minerva13c playlist).

5.7 Signal Efficiency

Fig. 5.14 shows efficiency[3] as a function of true electron energy. Efficiencies are calculated separately for each of two major playlists, to handle individually in case of variation of efficiency with time due to slightly different running conditions. In particular, the signal MC simulation was overlaid with events from different playlists as described in Section 3.5. The efficiency is calculated to be lower for higher instantaneous beam intensity due to deadtime and event overlapping. The overall efficiencies for playlists 1 and 13c are 0.729 and 0.733, respectively.

5.8 Stability

In order to verify that variations in beam and detector conditions are correctly simulated, the data is subdivided over time, and quantities related to the selected sample without the $\langle dE/dx \rangle_{1-4}$ and $E\theta^2$ cuts, the so-called "pre-selection" sample, were studied. Figure 5.15 shows the time variation of the number of events, the

---

[3]Efficiency of finding $\nu - e$ candidates, Efficiency $= \frac{\text{Number of reconstructed and "cut"-passed events}}{\text{Number of generated events}}$

mean electron energy and the $\langle dE/dx \rangle_{1-4}$. No excursions for small portions or the runs or slowly changing trends were observed. Number of event, energy, and dE/dx vs POT are plotted in Fig. 5.15.
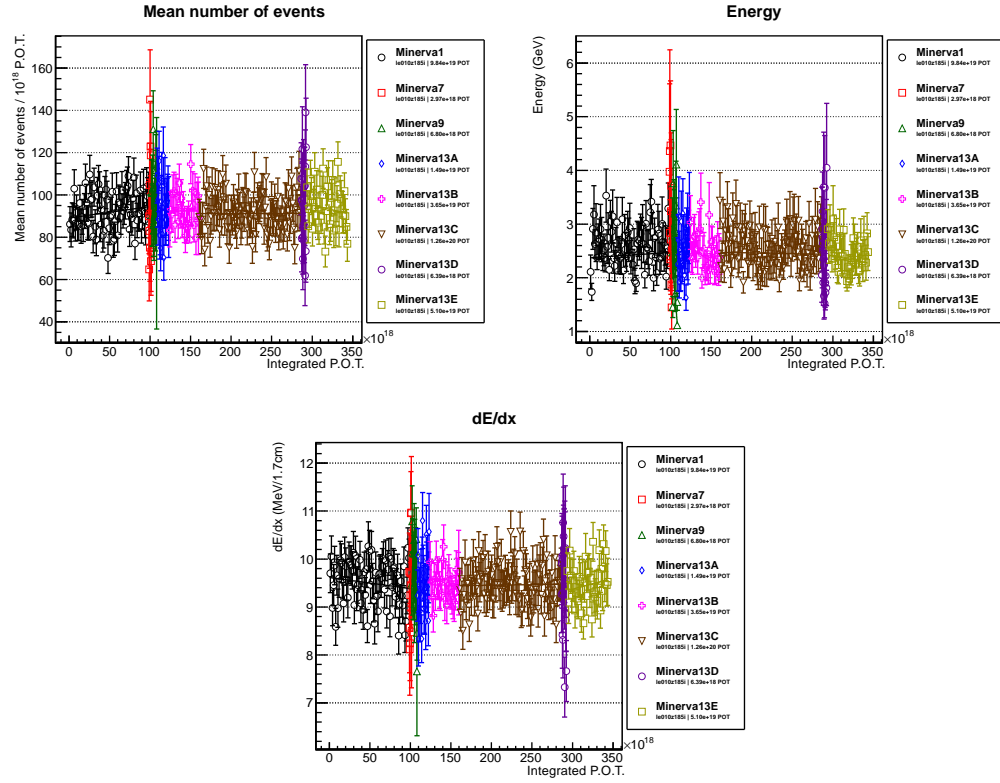

Figure 5.15: Stability of pre-selection samples: Number of events, energy, and dE/dx vs POT

The data was also subdivided by modules of in which the event vertex occurred to look for local problems in the detector, and similarly no problems were found. These "vertex stability" studies are shown in Appendix D.

5.9   Beam Angle Correction

At the location of the MINERvA detector the beam points down by $\approx 3°$ so that the NuMI beam arrives near the surface at the far detector location of MINOS in northern Minnesota, 735 km from MINERvA. While the direction of the beam is well known by survey relative to outside references, any measurement of track angles in the MINERvA detector is based on the MINERvA detector coordinates. If there is a misalignment of the MINERvA detector with respect to the beam, the measured angle at MINERvA will be shifted.

The beam angle is important for many measurements in MINERvA. For example, the neutrino energy reconstruction of CCQE events depends on the muon angle with respect to the beam direction. But because neutrino-electron scattering produces very "forward" electrons, ones at a small angle with respect to the beam direction, the angles in the x-z and y-z planes with respect to the beam direction peak sharply at zero which other interactions have a more broad distribution. Because the peak electron direction is the same as the beam direction, the neutrino-electron scattering signal can help to check the detector alignment if it is close enough so that the event selection hasn't affected the distribution. Fig. 5.16 shows angle x and y distributions of sample before $E\theta^2$ cut is applied. Peak positions of angles in the x-z and y-z planes, θ_x and θ_y, peak at the beam direction. Note that in the neutrino-electron scattering, the beam angle has a strong effect on the $E\theta^2$ event direction. We see modest evidence that the angle in the y-z plane, θ_y is slightly shifted with respect to the expectation. A correction to the beam angle in the data sample was applied to restore the peak position to zero angle, and $E\theta^2$ was recalculated using this corrected angle.
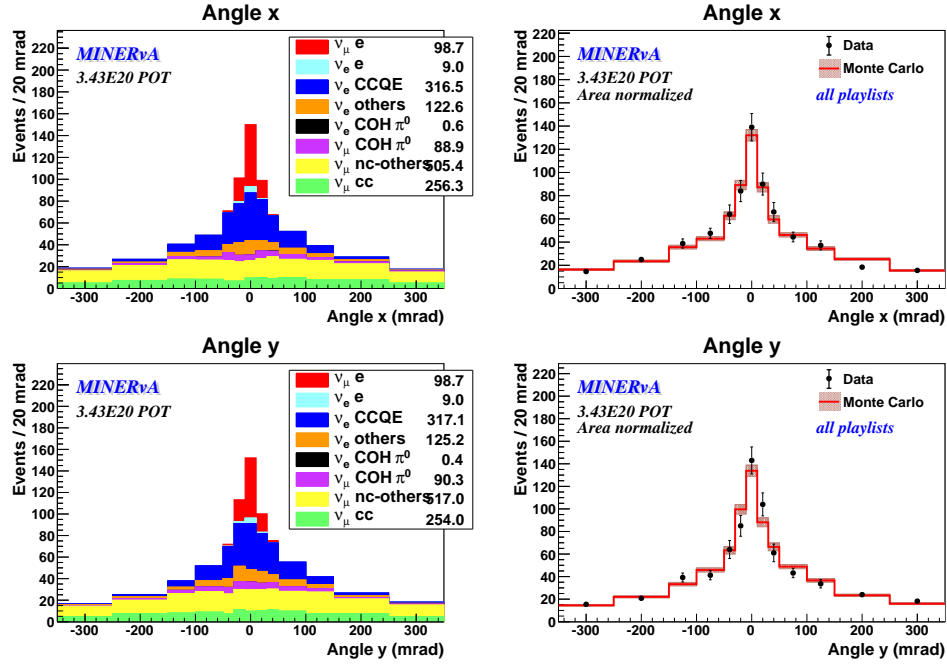
Figure 5.16: Angles in the x-z and y-z planes distributions of event sample before $E\theta^2$ cut is applied. The narrow peak is mainly from the signal events. Peak positions of angle x and y with respect to the nominal beam direction.

5.10   Background

As shown in Fig. 5.13, the number of predicted background events after the final event selection is a small fraction of the signal events. If the MC predicted background is subtracted from data distribution, then a measure of the number of neutrino-electron scattering events is obtained. This procedure is subject to systematic uncertainties in the MC prediction of the background because mismodeling of the background will bias the signal measurement. There are uncertainties in both the neutrino flux and the cross-sections for the background reactions. The uncertainties due to the flux are particularly problematic, since we seek to use this measurement to constrain the neutrino flux. To break the circular reasoning and

reduce the background uncertainties, sidebands, portions of the data that fail one or more of the event selection cuts, are used to constrain the backgrounds.

The sidebands are used to tune the background predictions so that the MC simulation gives results similar to the data in the sidebands. Tuning is a procedure that makes MC prediction similar to data by correcting normalizations for different background reactions and extrapolating those normalizations into the signal region. The uncertainties in the model are reduced but not eliminated, since these uncertainties may still result in uncertainties in this extrapolation. The sidebands also provide a test of the model and the uncertainties since one can study distributions of observables that are sensitive to the different reaction cross-sections in these sidebands. The tuning will be optimal if the tuned parameter is the real source of the discrepancy between data and MC. If the physics model is wrong, the tuning may not perform very well; if the model is approximately correct or only good in certain regions of the sideband, the tuning will not be perfect but it is still useful to make data and MC similar. In this analysis, we tune using many sideband distributions in the data to thoroughly test these predictions of the background within their uncertainties. Two different tuning parameters may have similar effects on one distribution but have different effects on the another distribution.

In principle, it is ideal to tune all the free or uncertain parameters in the flux and cross-section model. However, it is more practical to fit for a small number of non-degenerate parameters. The simplest case is just to fit for an overall correction to the rate of a given process. We will test if this simplification is acceptable by comparing distributions of observables in the data and simulation in the sidebands.

Fig. 5.17 shows background components after the final event selection. The total background consists of many different reactions which are governed by distinct
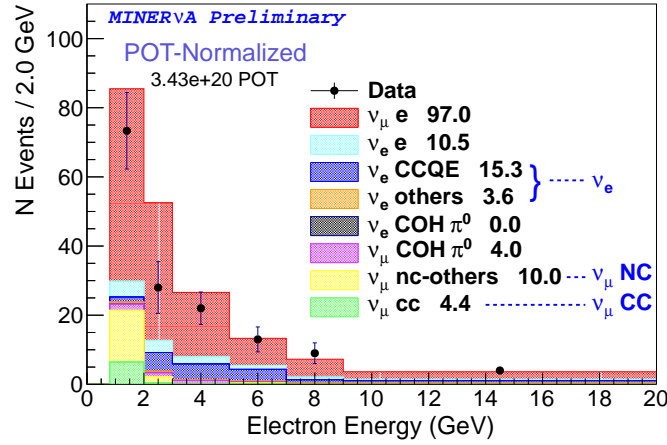
Figure 5.17: Electron spectrum after final cut before tuning

physics models. The background components which are tuned are those which are known to be most uncertain and have the biggest representation in the signal and sideband regions. In tuning, we classify reactions as either charged-current (CC) or neutral-current (NC). Both are subject to uncertainties from the neutrino flux, but NC cross-sections have additional uncertainties because the measurements of these reactions are few, and the uncertainties are therefore larger. The largest component in background as shown in Fig. 5.17 is ν_e CCQE reaction, and here the major uncertainties in the model of ν_e CCQE events is due to the large uncertainty in the ν_e flux. Because of this, all ν_e induced events are grouped together with one tuning parameter. The coherent π^0 production is not tuned but it is an insignificant part of total background. Future analysis might attemp to tune either by improved sideband tuning or using CC coherent measurement. So in summary, the model tuning parameter chosen for the sideband studies are four normalizations: one for all ν_e induced processes except coherent π^0 production, one for all NC ν_μ induced processes except coherent π^0 production, and one for all CC ν_μ induced processes.
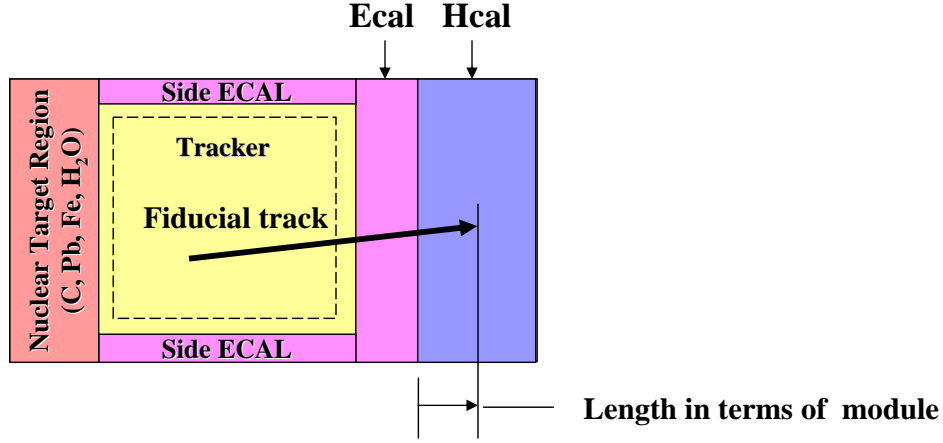
Figure 5.18: Fiducial track length in Hcal

After choosing the parameters to tune from the sideband data, we need to chose the selections for defining the sidebands and the distributions in those sidebands to fit.

5.10.1 Distributions Studied in Sideband Tuning

Two new quantities are introduced in the sideband studies which are not used in the signal selection.

Any track that originates from the fiducial volume is defined as a fiducial track. The length that such fiducial tracks penetrate into the Hcal, defined schematically in Fig. 5.18, is a good discriminant between tracks from electromagnetic showers, which do not penetrate far into the Hcal, and MIP tracks such as muons from charged-current interactions which will typically penetrate deep into the Hcal.

Min$\{dE/dx_{2-6}\}$ is defined as the minimum measured deposited energy, dE/dx, in the second to sixth planes of the candidate electron, numbering from plane one at the vertex. The main difference between $\langle dE/dx \rangle_{1-4}$ and this measure, is that

Min$\{dE/dx_{2-6}\}$ is less sensitive the possibility of a few planes with high deposited energy near the vertex. For example, in ν_e CCQE, the recoiling proton may leave noticeable energy near the vertex that overlaps with the electron shower cone. Typically these protons are not collinear with the electron, and some of the energy of recoil protons may not be fully contained within the shower cone. But even in these cases, some of the energy may overlap in one view as illustrated in Fig. 5.5. Even in such cases, however, the XUXV plane arrangement ensures that such overlaps cannot happen in every plane, and therefore Min$\{dE/dx_{2-6}\}$ will select dE/dx from one of the planes without an overlapping electron. When a low energy proton makes energy deposition only in first a few planes, Min$\{dE/dx_{2-6}\}$ is not affected by the small vertex energy. Most ν_e CCQE events will have Min$\{dE/dx_{2-6}\} < 3$ MeV/1.7cm.

5.10.2 Sideband Region

As discussed earlier, the final selections for background rejection require $\langle dE/dx \rangle_{1-4} <$ 4.5 MeV/1.7cm and $E\theta^2 < 0.0032$ GeV radian^2, shown as region (a) in Fig. 5.19. The primary sideband, region (b), is defined to be all events with $E\theta^2 > 0.005$ GeV radian^2 and $dE/dx < 20$ MeV/1.7cm. Very high dE/dx tends to select complicated events which are not representative of the events that are background to this analysis. The region $0.0032 < E\theta^2 < 0.005$ GeV radian^2 is not used in the sideband in order to avoid having a significant signal component in the sideband region. for sideband to avoid the mixed region that has both signal and background. Region (c), $E\theta^2 < 0.005$ GeV radian^2 and $4.5 < dE/dx < 20$ MeV/1.7cm, is not used because $E\theta^2 < 0.005$ GeV radian^2 is a very restrictive requirement that selects a tiny population compared to the sideband, except for in the case of the signal reaction.

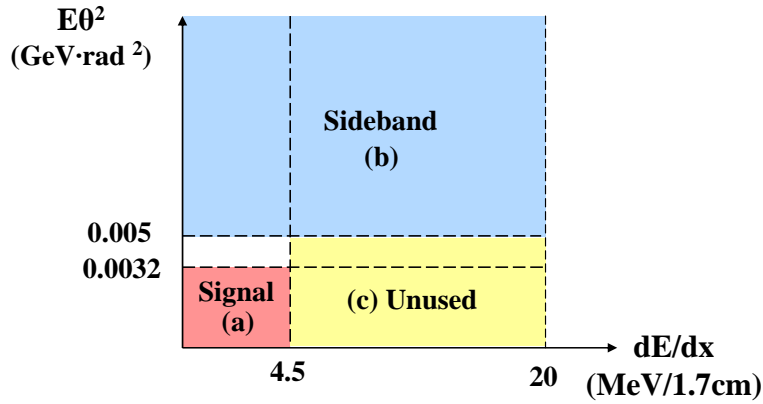The primary sideband ($E\theta^2 > 0.005$ GeV radian^2) is a sample with many real elec-

Figure 5.19: Sideband region

tromagnetic (EM) showers, but very of these events are ν_μ CC background because of the restrictive cuts in the analysis. Several cuts were dropped from the standard analysis to define the sideband to accept more of these events: the shower end transverse position was no longer required to be < 1050 mm, and the shower transverse spread int he first 1/3 of the shower was no longer required to be < 20 mm. ν_μ CC sensitive distributions, the shower end transverse position and the track length in the Hcal, are shown in Fig. 5.20. ν_μ CC events dominate the events with shower end transverse position > 1050 mm region because these events contain side exiting muons.

The sideband is further divided into three sub-regions so that the sub-regions contain a different mixture of background components. If a particular background component is a small fraction of the overall sideband, it is difficult to constrain this sideband. This subdivision also helps to enhance shape differences in the distributions used in the fit. Without such shape differences, it is also difficult to constrain the different components that make up the background. The three sub-regions are shown in Fig. 5.21. The three regions are separated by electron energy and by
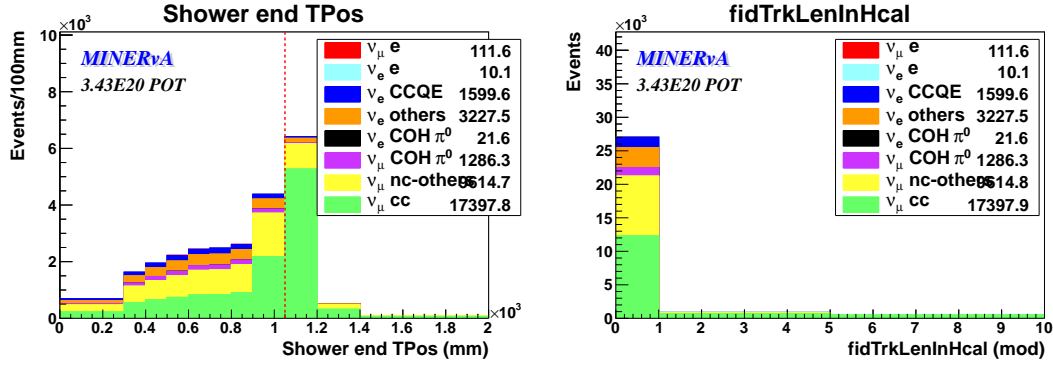
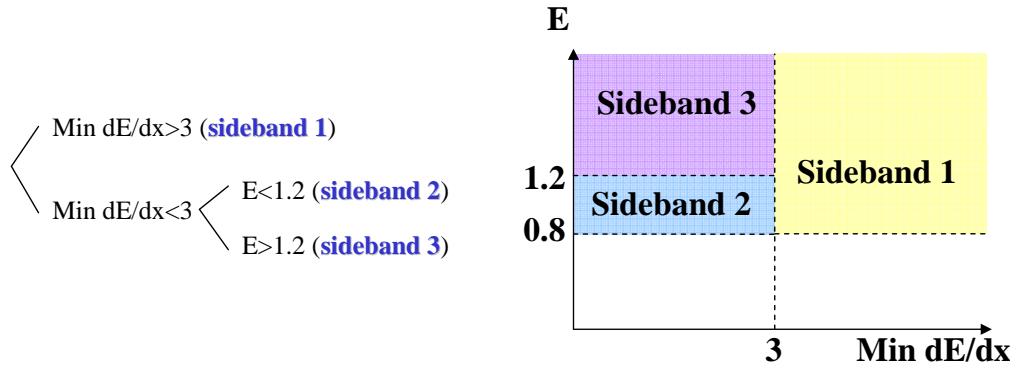Figure 5.20: Shower end transverse position and shower end position in Hcal

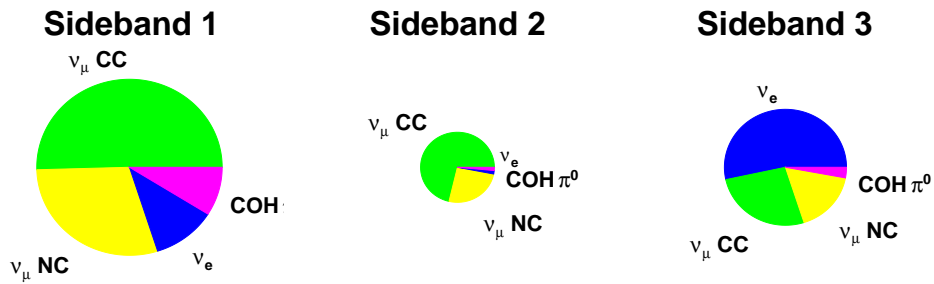Figure 5.21: Division of sidebands

Figure 5.22: The composition of each of the background sidebands

$\text{Min}\{dE/dx_{2-6}\}$. The composition of each of the sidebands is shown in Fig. 5.22.

5.10.3   Sideband Tuning

The sideband tuning is performed by adjusting the normalization of each of the three processes described above to make the Monte Carlo (MC) simulation agree with the data distributions in each of the three sidebands. The normalization of ν_e induced processes, ν_μ NC and ν_μ CC processes are simultaneously tuned using seven distributions in three sidebands to match normalisation and shape of the distributions with data.

Optimal normalizations are determined by a χ^2 fit comparing the data and MC distributions as a function of the normalization parameters. The χ^2 minimization is performed by the TMinuit [?] minimization module in ROOT [?] with the MIGRAD algorithm.

A total of seven distributions are fit in the sideband tuning:

- Sideband 1:

    - shower end transverse position

    - fiducial track length in Hcal

- Sideband 2

    - shower end transverse position

    - fiducial track length in Hcal

- Sideband 3 (ν_e enhanced)

    - shower end transverse position

    - fiducial track length in Hcal

    - maximum Transverse RMS among X, U, and V-views
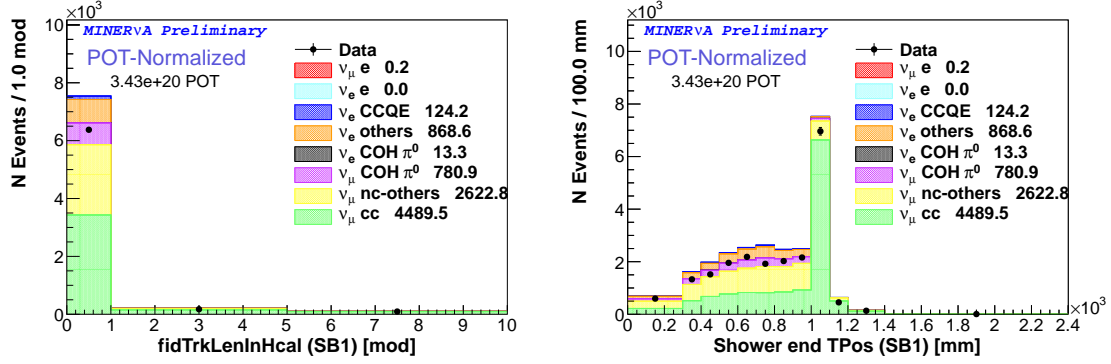
Figure 5.23: Distributions in sideband 1 before tuning
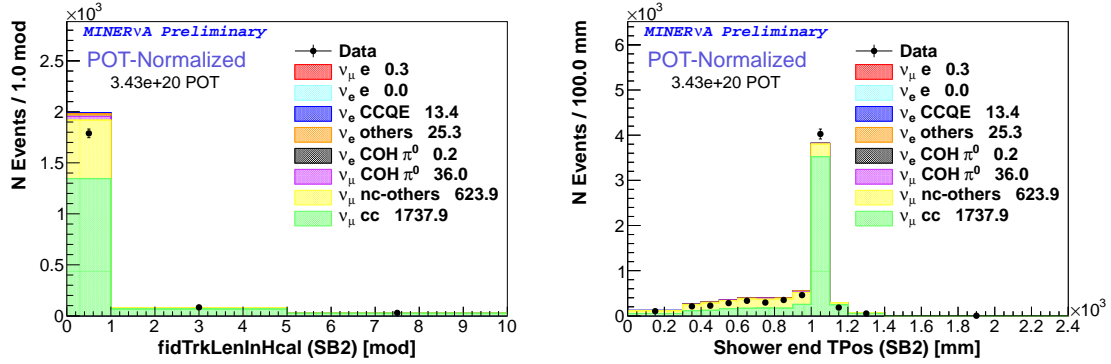
Figure 5.24: Distributions in sideband 2 before tuning

The seven distributions are shown in Figs. 5.23, 5.24, and 5.25.

The sideband tuning minimizes χ^2 in the seven distributions of sidebands one through three simultaneously. The χ^2 used in the minimization is the sum of the seven individual χ^2 so that

$$\chi^2 = \sum_m \sum_i \frac{\left(D_i^{(m)} - M_i^{(m)}\right)^2}{M_i^{(m)}},$$ (5.19)

where m is histogram index, i is bin index in a histogram, D is data histogram,
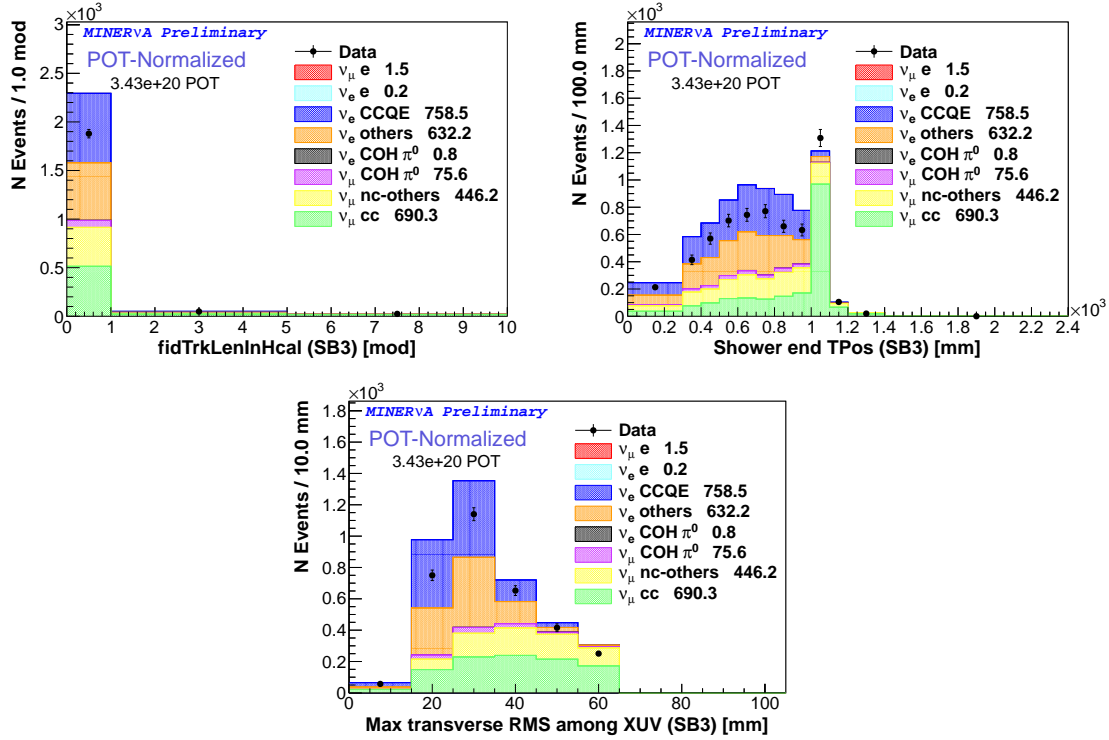
Figure 5.25: Distributions in sideband 3 before tuning

Parameter	Tuned value
ν_e	0.76 ± 0.03
ν_μ NC	0.64 ± 0.03
ν_μ CC	1.00 ± 0.02

Table 5.2: Tuned parameter values

and M is MC histogram. Variable histogram binning is used to ensure that the MC simulation prediction has at least twenty entries in each bin. The χ^2 is a poor approximation of the true likelihood of the data distribution given the prediction when the number of entries in each bin is too small.

The normalization parameters after tuning are shown in Table 5.2. A comparison of the sideband distributions in data and MC simulation after tuning is shown in

Figure 5.26: Distributions in sideband 1 after tuning
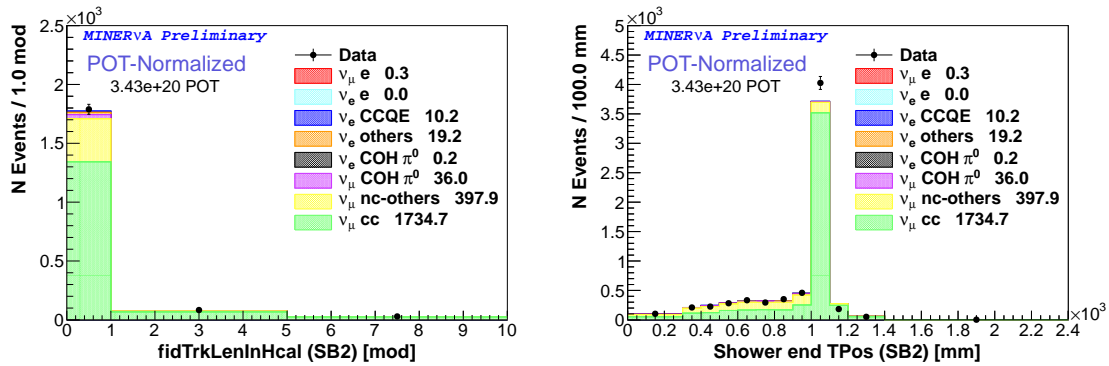
Figure 5.27: Distributions in sideband 2 after tuning

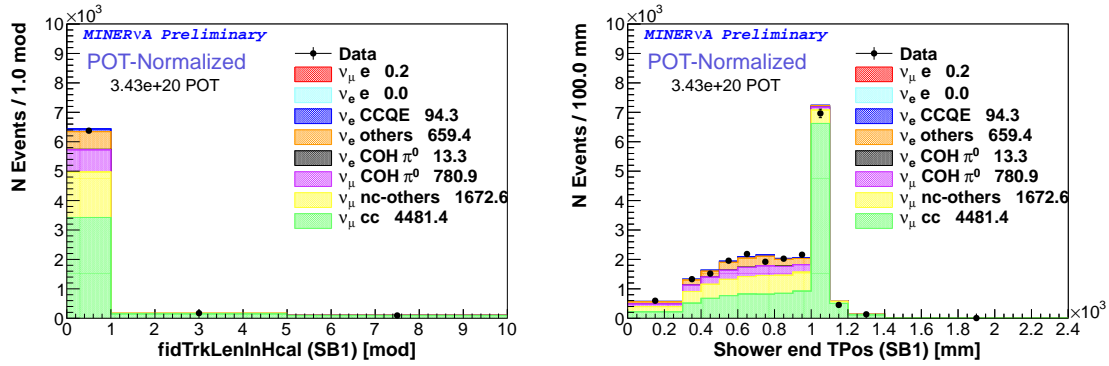Figs. 5.26, 5.27, and 5.28.
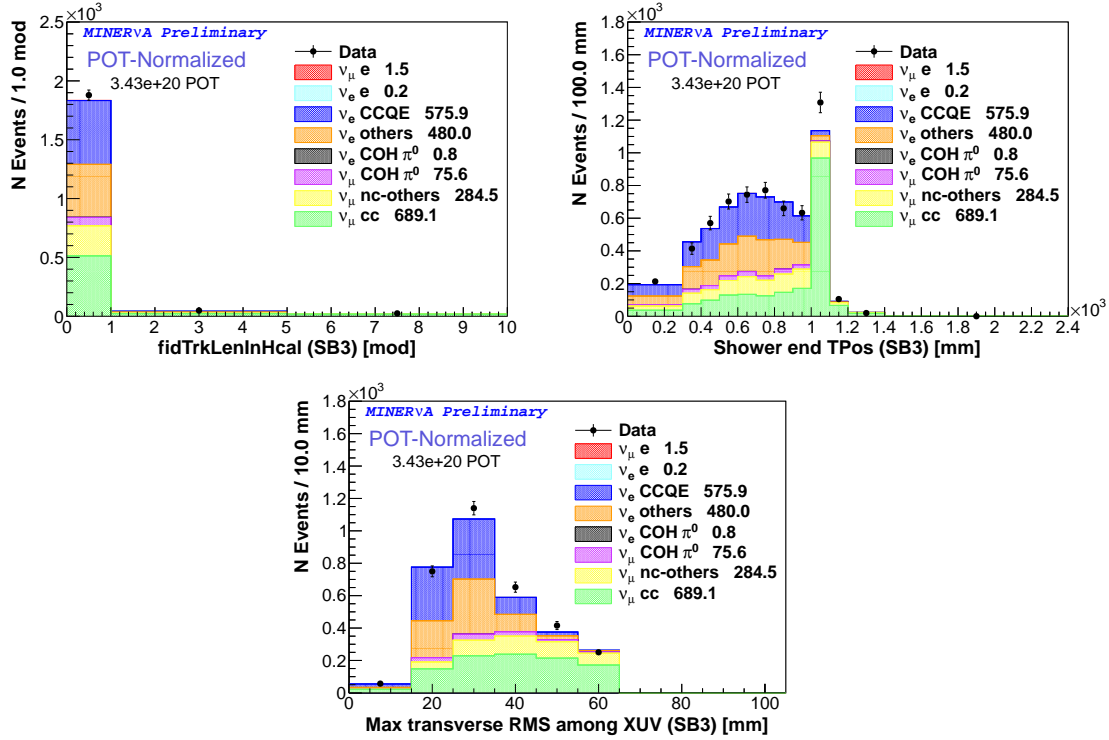
Figure 5.28: Distributions in sideband 3 after tuning

5.11 Multi-universe Method

To evaluate systematic uncertainties, this analysis uses the so-called "multi-universe" method. In this method, each "universe" is a single scenario that incorporates systematic uncertainties on the models of the neutrino flux, MINERvA detector and underlying reaction cross-sections. A reweighting of a single MC simulation sample is used to simulate each of these universes. The name multi-universes refers to the creation of a statical ensemble of such individual randomly generated universes. The measurement is repeated in each individual universe and the statistical variation of the measurements is used to evaluate systematic uncertainties.

There are many individual systematic uncertainties that are evaluated. For con-

venience and clarity of presentation, the largest uncertainties are combined into broad categories.

All systematic uncertainties on neutrino interactions are simulated within GE-NIE by varying individual parameters. A complete list of these uncertainties is given in Appendix E, but in final evaluations, these uncertainties are combined into a single GENIE parameter systematic.

There are also large uncertainties associated with the flux of neutrinos on the detector. These are grouped into three categories. *Focusing* uncertainties are uncertainties in the beam optics. This includes uncertainties from alignment of two horns, uncertainties in the horn current, and uncertainties on the current distribution within the horn[4][**?**]. MINERvA uses data from the NA49 hadron production experiment that measures pion and kaon rates produced from interactions of protons on thin carbon targets. If neutrinos result from such measured interactions, the rate is given by the NA49 measurements and the uncertainties of that data are used as an uncertainty in the flux. Approximately 60% of neutrinos are produced by processes that use this data to constrain the flux, and we refer to these uncertainties as *NA49* uncertainties. The primary reactions not constrained by this data are reactions where the are multiple interactions in the target or in other material such as horns and the decay pipes that create the particles that decay into neutrinos. We use the term *Tertiary* to cover the uncertainties on such processes since the most common case of such reactions is production of secondary particles in interactions of primary protons in the carbon target, which then result in a tertiary meson that decays to neutrinos. This uncertainty is evaluated by the maximum spread on different available hadron production models, QGSP, FTFP_BERT, QGSC_BERT, QGSP_BERT
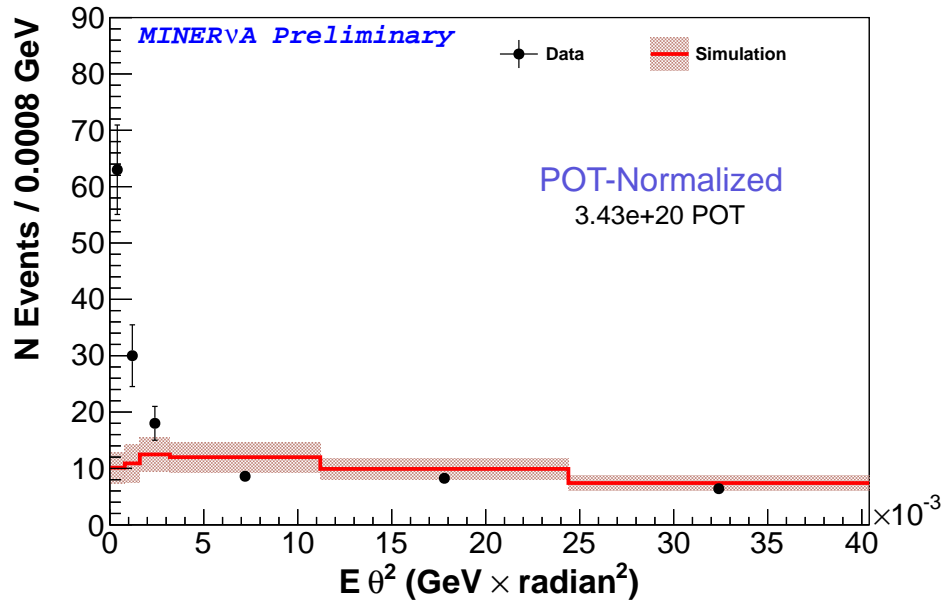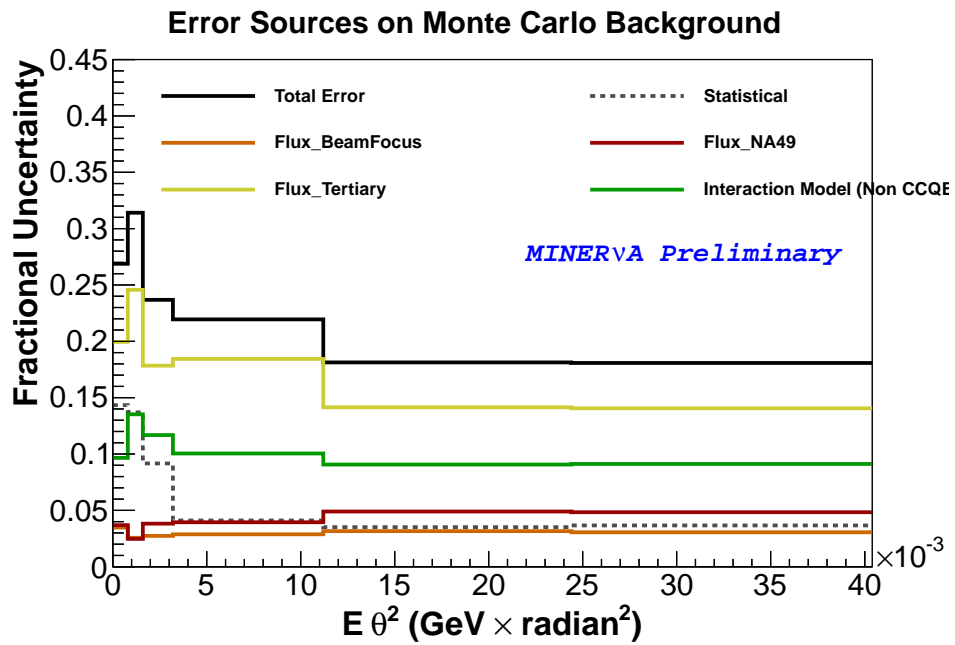
---

[4]Alternating current flows slightly below the conductor surface (skin depth).
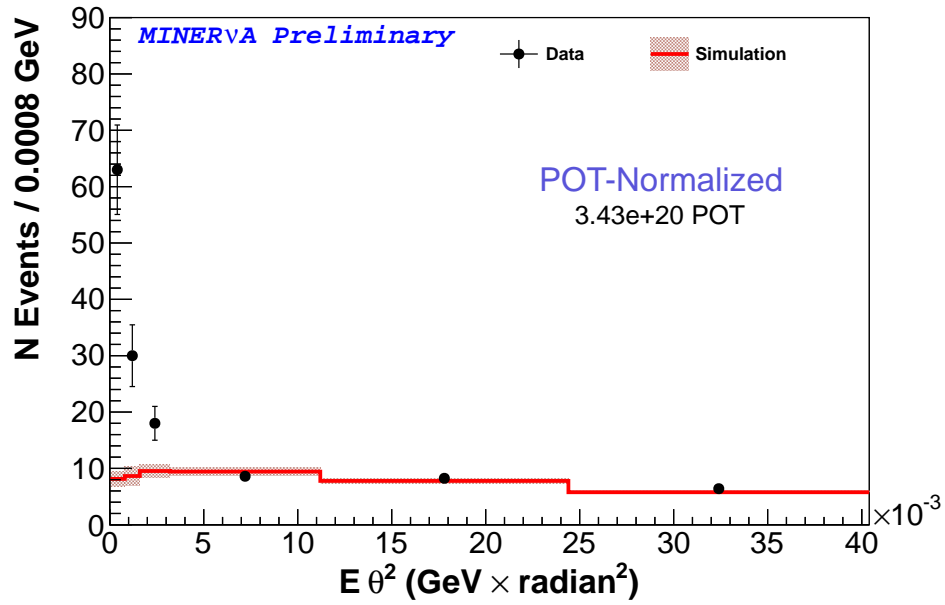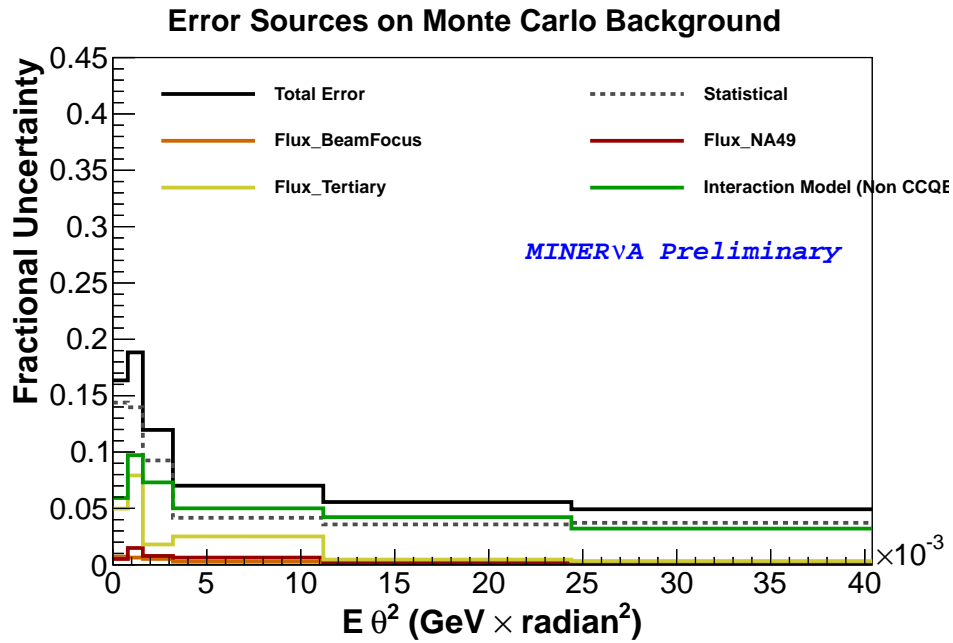
and FTF_BIC.

5.12   Sideband Tuning on Multi-universes

As part of the evaluation of systematic uncertainties in the multi-universe method, sideband tuning was performed on each universe. This provides a way to measure how systematic uncertainties are reduced by the data constraint in the sideband tuning. A simplest example of an uncertainty we would expect to vanish in sideband tuning is the normalization uncertainty, such as one due to uncertainty in the scintillator mass in the detector. If the MC normalization is different than reality, the sideband tuning will alter the MC normalization to match the data. The flux uncertainties, although they do have some variation with neutrino energy, have an overall uncertainty independent of energy as their primary effect. Therefore, much of the flux uncertainty will be reduced by sideband tuning.

Fig. 5.29 shows the uncertainty, as an error band, on the background from multi-universe before the tuning. Note that there are correlations between the uncertainties in the different bins since many systematic uncertainties have correlated effects across the bins. Fig. 5.30 shows the size of major category of systematic uncertainty before the tuning. The Tertiary flux uncertainty is the largest, and uncertainties due to the GENIE interaction model are the second largest. Figs. 5.31 and 5.32 show the reduction of the error band after the sideband tuning. Similar plots restricted to the selected signal sample are shown in Figs. 5.33, 5.34, 5.35, and 5.36. The reduction in the Tertiary flux uncertainty is substantial, but large uncertainties due to interaction cross-section remain.

Figure 5.29: MC background error band in $E\theta^2$ before tuning

Figure 5.30: MC background uncertainty breakdown in $E\theta^2$ before tuning

Figure 5.31: MC background error band in $E\theta^2$ after tuning

Figure 5.32: MC background uncertainty breakdown in $E\theta^2$ after tuning

Figure 5.33: MC background error band in signal region before tuning

Figure 5.34: MC background uncertainty breakdown in signal region before tuning
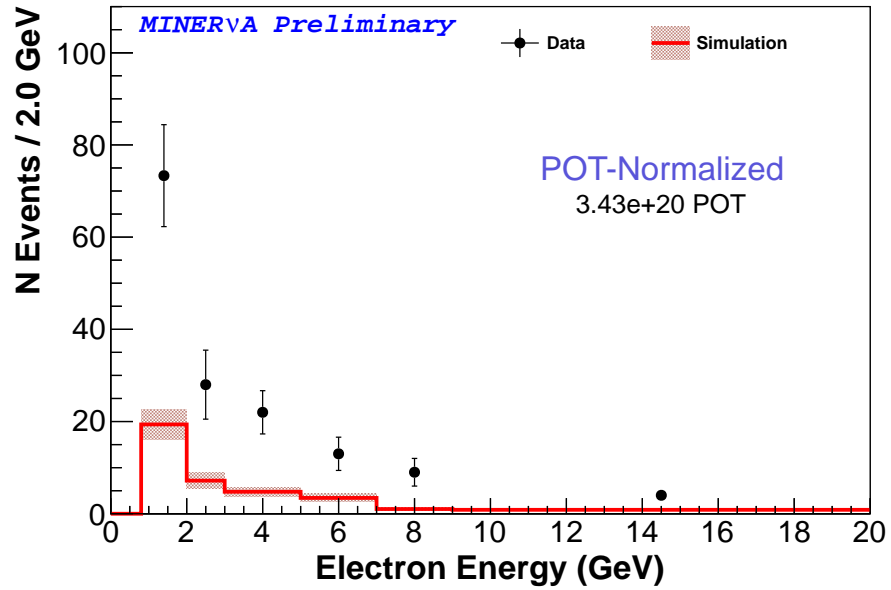
Figure 5.35: MC background error band in signal region after tuning
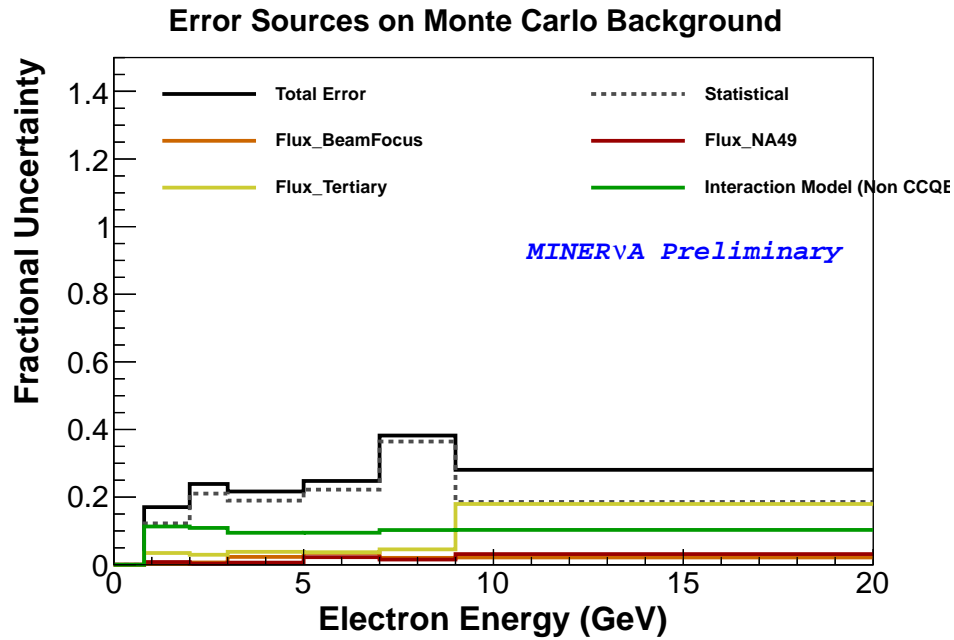
Figure 5.36: MC background uncertainty breakdown in signal region after tuning
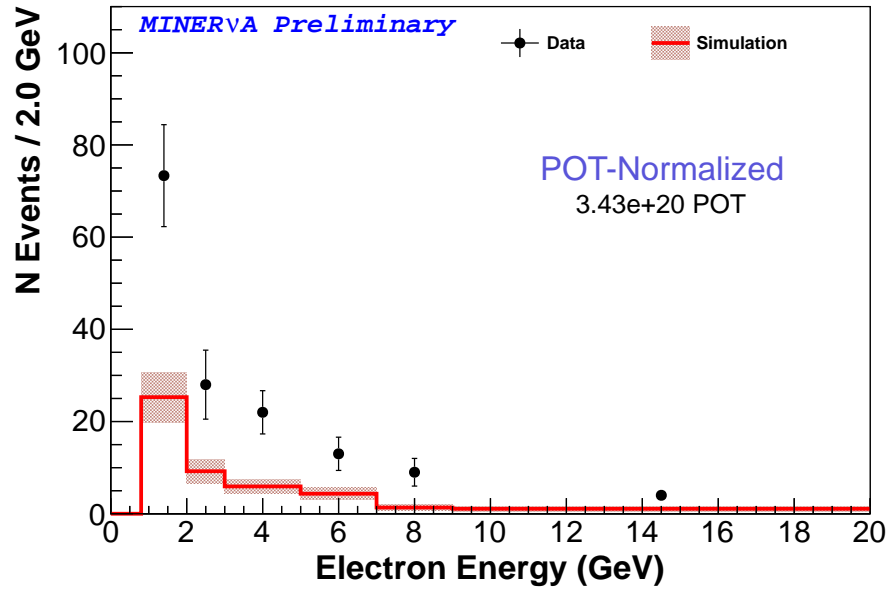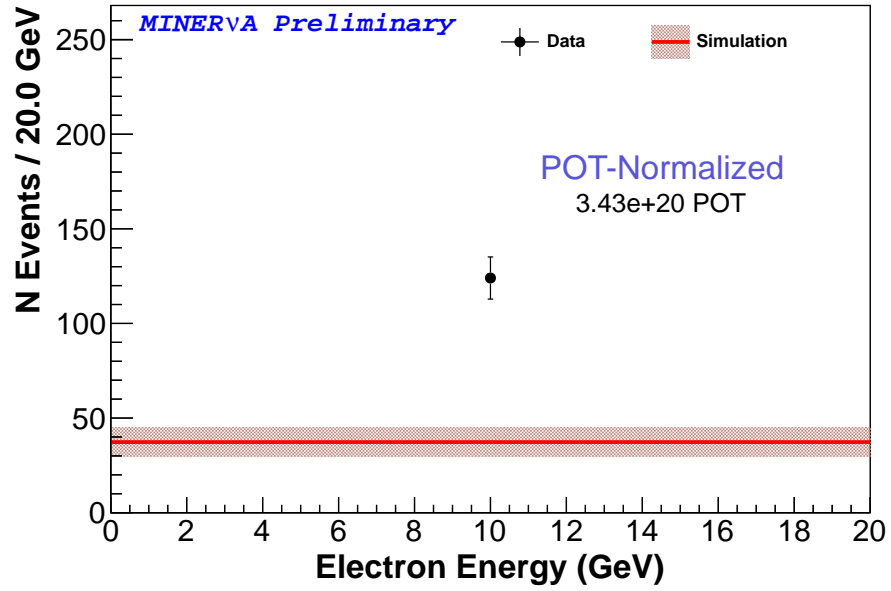
Figure 5.37: MC background error band (1bin) in signal region before tuning
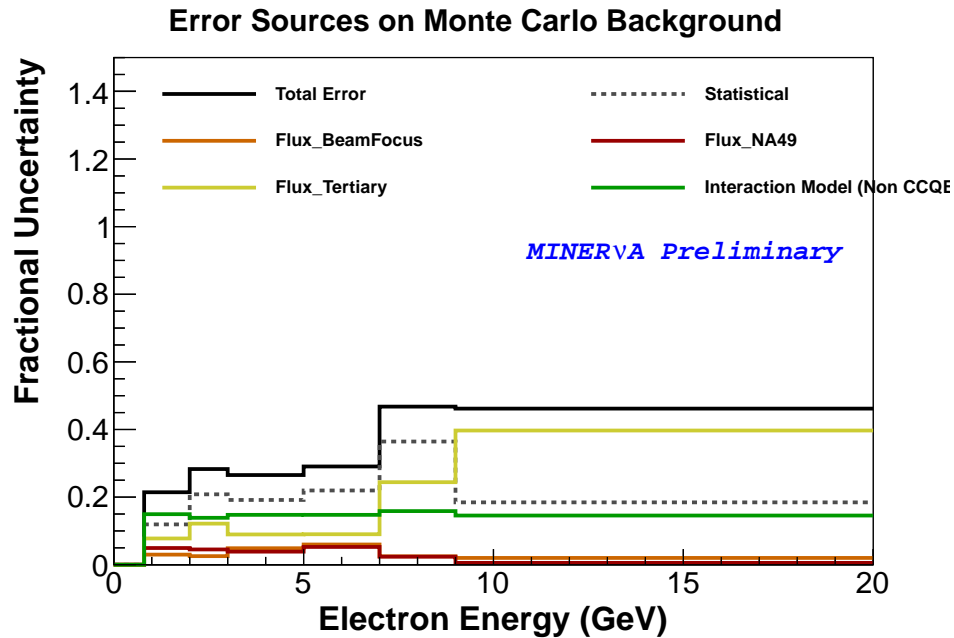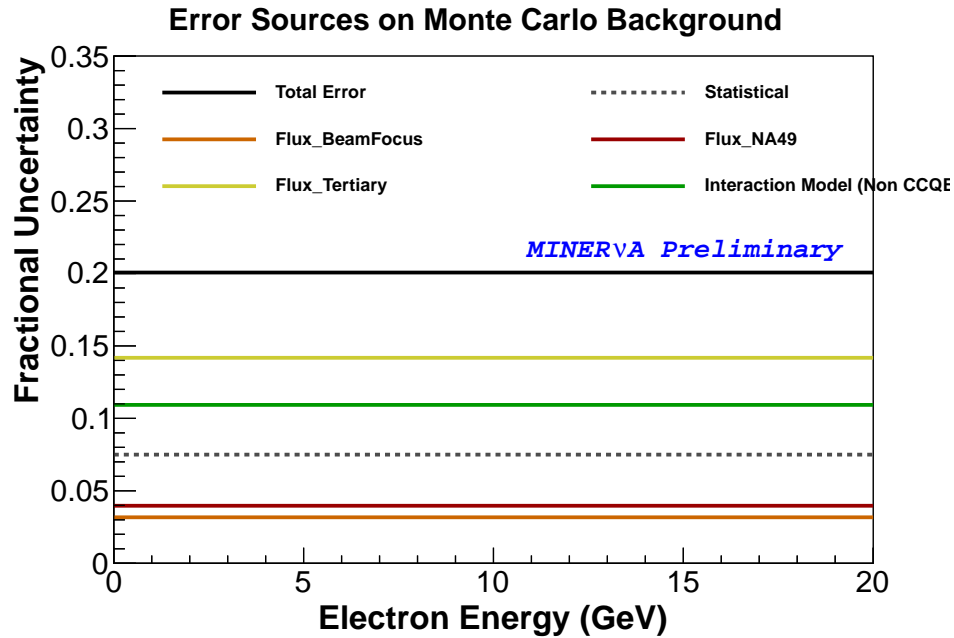

Figure 5.38: MC background uncertainty breakdown (1bin) in signal region before tuning
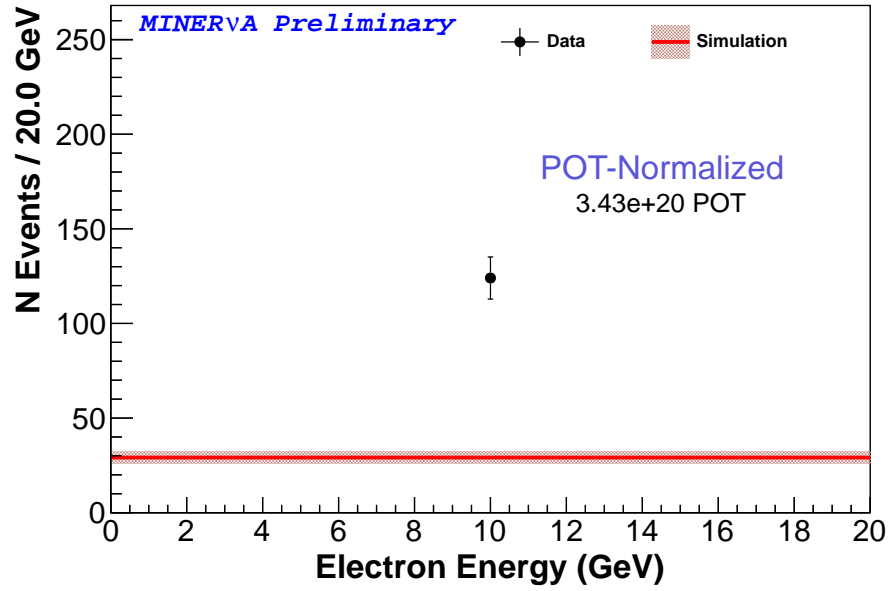
Figure 5.39: MC background error band (1bin) in signal region after tuning
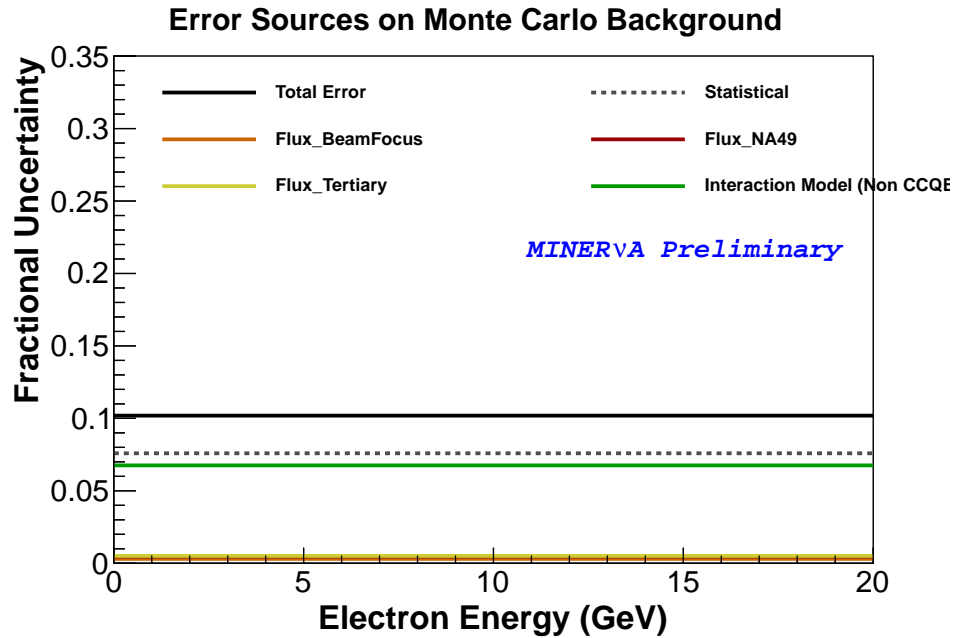
Figure 5.40: MC background uncertainty (1 bin) breakdown in signal region after tuning

Chapter 6

Results

6.1 Electron Spectrum of ν–e Scattering

After both the selection of events in data and the tuned background prediction complete, 124 neutrino-electron elastic scattering candidate events are observed with tuned background of $29 \pm 2(\text{stat}) \pm 3(\text{syst})$. The measurement of the number of neutrino-electron elastic scattering events in the event sample is performed by subtracting the background from the sample and correcting for the signal efficiency discussed in Section 5.7. The resulting electron energy spectrum is shown in Fig. 6.1.

Fig. 6.2 compares the measured electron energy spectrum and the Monte Carlo (MC) predicted electron energy spectrum. Since there is no significant uncertainty in the neutrino-electron scattering cross-section, the uncertainty on the predicted spectrum comes directly from the prediction of the neutrino flux. A significant disagreement between these two would therefore be an indication of an incorrect neutrino flux prediction.
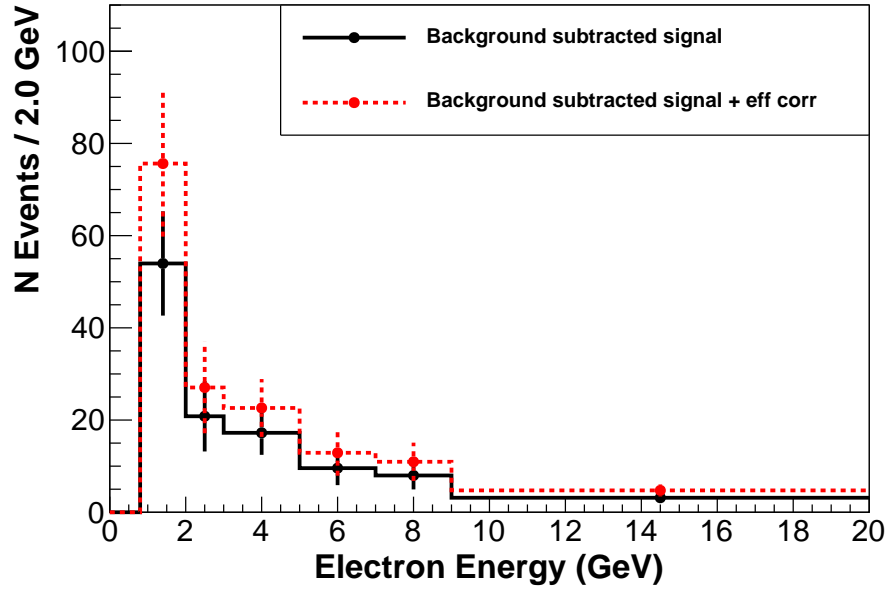
Figure 6.1: Efficiency correction on tuned MC background subtracted data

The total rate of $\nu e \rightarrow \nu e$ scattering events in the detector fiducial volume, estimate from the measured νe events is $131 \pm 16(\text{stat}) \pm 7(\text{syst})$. The Monte Carlo prediction is $149 \pm 19(\text{flux})$.

6.2 Discussion

This result provides a measurement of the rate of neutrino-electron scattering events which is in good overall agreement with the flux prediction, and is of comparable precision to that prediction. As noted in Fig. 1.9, the electron energy distribution for the ν_μ that dominate the flux (Fig. 6.4 is approximately uniformly distributed up to the neutrino energy, and the scattering cross-section rises linearly with neutrino energy. Therefore, this measurement has a stronger constraint on the high energy
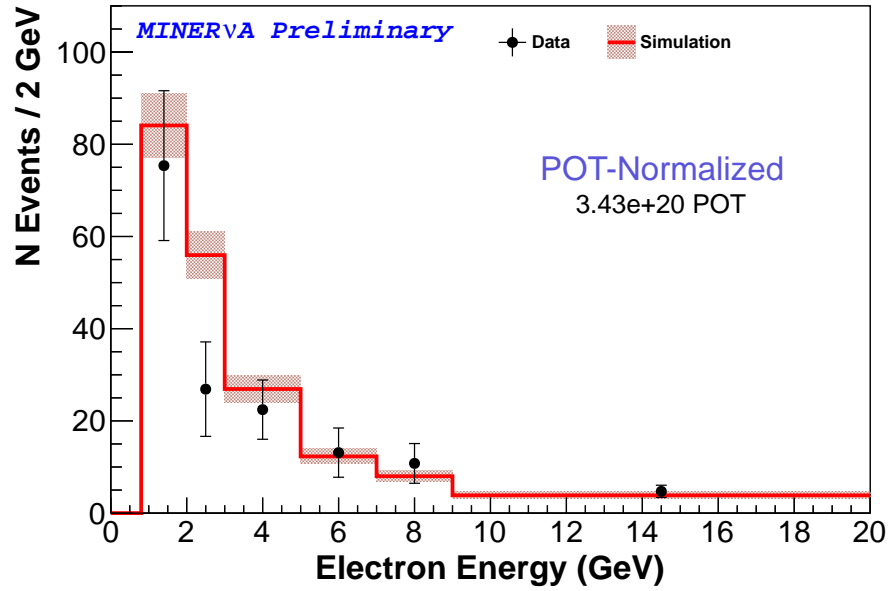
Figure 6.2: Comparison of efficiency corrected electron energy and MC true electron energy predicted by default MC flux
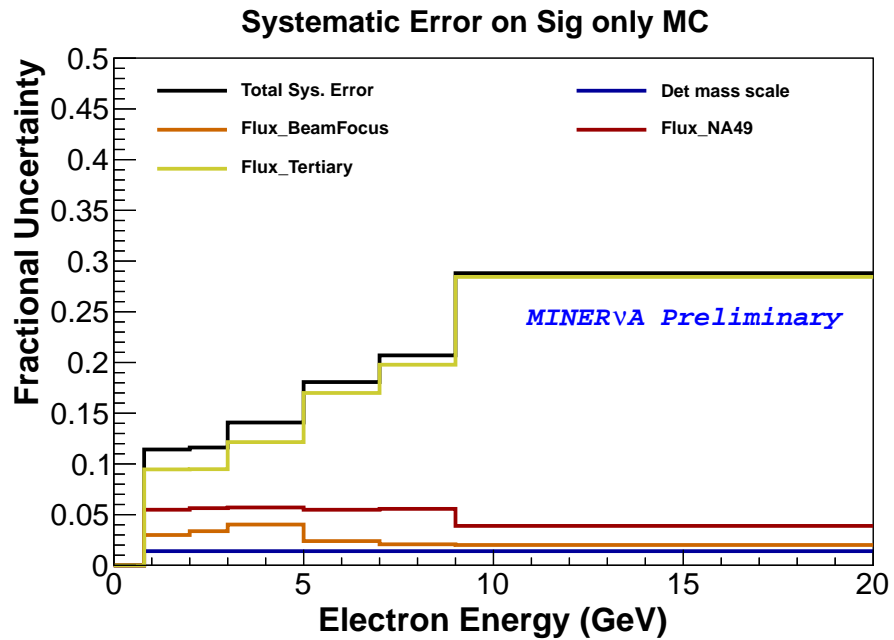
Figure 6.3: Electron energy uncertainty of νe events
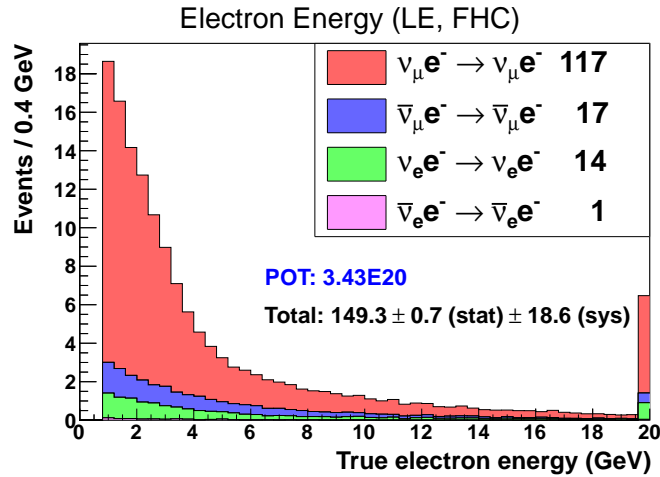
Figure 6.4: MC true electron energy by each neutrino flavor

neutrino flux than that at lower energies.

The electron energy spectrum based on the νe scattering measurement in Fig. 6.2 has large uncertainties in each individual energy bin, so the ability of this result to constrain the neutrino flux as a function of energy is marginal. There is a barely significant indication that the rate of events observed below 3 GeV electron energy is less the nominal flux predicted, with a deficiency of $36 \pm 21\%$ but no such deficiency at higher energies. This indicates that the data would prefer slightly less flux at lower neutrino energies, but again, the observation is not significant.

MINERvA will continue to operate in the medium energy (ME) run in the NuMI beamline. Neutrino beam peak energies of LE and ME are about 3.5 and 6.5 GeV, respectively, as shown in Fig. 2.3. The νe scattering sample in this beam will be significantly larger because the νe total cross-section is proportional to the neutrino energy and because the expected number of protons on target should be 12×10^{20} POT, about 3.5 times the size of the exposure in this analysis.

An important part of the machinery developed for this analysis is the tuning

of backgrounds on data using sideband samples. This suggests that uncertainties on the backgrounds will decrease with increased statistics. Our preliminary MC simulation studies suggest that the signal-to-background ratio will be similar in the ME beam to that in the LE beam used in this analysis. For the full ME sample, we expect approximately 1100 signal and 300 background events. That should provide a flux integrated constraint with 3–4% uncertainty, which is much smaller than the uncertainty of the flux prediction itself.

Chapter 7

Conclusion

Studies of neutrinos have long been difficult because these elusive particles rarely interact with matter. Wolfgang Pauli, who proposed the neutrino in 1930 as a way to solve puzzles in beta decay, was later critical of his idea: "I have postulated a particle that cannot be detected". The weak interactions of the neutrino do make the reaction rate very small, and fewer than one in a billion of the neutrinos passing through our MINERvA detector ever interact. But with enough neutrinos and a sufficiently large detector, today we are able to study their reactions. A major difficulty in such studies is that there are few direct ways to study the source of neutrinos, independent of observing their reactions that are the object of studies. Indirect methods of characterizing the source of neutrinos are complex and imprecise.

Since its discovery in the late 1990s, neutrino flavor oscillation has become one of most interesting phenomena in particle physics. Its occurrence implies that the Standard Model of particle physics is incomplete since it cannot accommodate massive neutrinos. It also opens the possibility of differences between neutrinos and their anti-matter counterpart, anti-neutrinos. Such differences, some of which are

observable by studying reactions of neutrinos in future neutrino oscillation experiments, might have seeded the difference between matter and anti-matter which led to today's matter dominated Universe.

In this work, an extremely rare neutrino scattering process, neutrino-electron elastic scattering $\nu + e^- \rightarrow \nu + e^-$, is measured as a reference process to determine the flux of neutrinos per unit of primary beam energy and per unit area at our detector, in the NuMI neutrino beam at Fermi National Accelerator Laboratory (Fermilab). Indirect methods can be used to predict the flux of this beam, which is produced by interactions of 120 GeV protons in a carbon target that produce unstable hadrons which, in turn, decay to neutrinos. The prediction of neutrino beam flux has large uncertainty due to a poor understanding of the relevant hadron production reactions. By contrast, neutrino-electron elastic scattering is predicted unambiguously to better than 1% precision in the electroweak unified theory of the Standard Model. Therefore, by measuring the rate of this well understood reaction, the neutrino flux can be constrained.

Use of neutrino-electron scattering as a reference reaction is challenging because it has very small cross section. Isolating the reaction from background reactions that are nearly ten thousand times more common is critical for this technique to be practical. Because the electron is a very light target, neutrino elastic scattering from electrons produces an electron that travels in nearly the same direction as the incoming neutrino. A requirement that the observed electrons be precisely in this direction and that no other activity is observed in the detector is the main discriminant to reduce this background. In addition, mean energy loss of the candidate electrons per unit length in our detector is used to reduce the largest remaining background, which comes from photons that result from production of neutral pions

in the detector. These photons, when they react in the material of the detector, convert to e^+e^- pairs, which looks exactly like an electron but have twice as much energy loss per unit length in the initial signal they leave in the MINERvA detector.

Using a data sample produced by neutrinos from 3.5×10^{20} protons hitting our target in the NuMI low energy neutrino beam configuration, neutrino-electron elastic scattering can constrain the overall flux with 13% precision. That precision is comparable to indirect methods. This technique will be more precise in MINERvA's upcoming higher statistics run in the NuMI medium energy beam. In the future experiments such as Fermilab's planned LBNE, which have higher rate neutrino beams, this technique could be even more precise and might be the best tool for providing a direct measurement of the neutrino flux.

In our experiment, MINERvA, the neutrino flux is the denominator for all measurements of neutrino cross-sections that will be performed by the MINERvA experiment, which in turn are valuable inputs for future accelerator-based neutrino oscillation experiments.

Appendix A

Kinematic Constraint on $E\theta^2$

$E\theta^2 < 2m_e$ constraint is purely from two body kinematics. For a scattering of the form $AB \rightarrow CD$, we have two independent kinematic variables. Mandelstam variables are Lorentz invariant and they are often used to express other kinematic variables in two body scattering. Three variables (s, t, u) are defined as follows,

$$s = (p_A + p_B)^2 \tag{A.1}$$

$$t = (p_A + p_C)^2 \tag{A.2}$$

$$u = (p_A - p_D)^2 \tag{A.3}$$

where p_A, p_B, p_C, and p_D are 4-momentum vectors for particle A, B, C, and D. Not all of three variables are not independent. They are constrained by the following relation,

$$s + t + u = m_A^2 + m_B^2 + m_C^2 + m_D^2. \tag{A.4}$$

Now kinematic variables will be calculated for $\nu + e \rightarrow \nu + e$ scattering. p_ν and

p_e represent 4-momentum for initial neutrino and electron, respectively. And, p'_ν and p'_e represent 4-momentum of neutrino and electron after collision. t in the CM (center of mass) frame is calculated as follows,

$$t = (p_\nu + p'_\nu)^2 \tag{A.5}$$

$$= 2p_\nu \cdot p'_\nu \tag{A.6}$$

$$= 2E_\nu E'_\nu (1 - \cos\theta^*) \tag{A.7}$$

$$= \frac{s}{2}(1 - \cos\theta^*) \tag{A.8}$$

where θ^* is scattering angle in the CM frame. Electron rest mass was ignored, as interesting scattering is highly relativistic ($E_e \gg m_e$).

Inelasticity y is defined as follows,

$$y = \frac{p_B \cdot q}{p_B \cdot p_A} \tag{A.9}$$

$$= \frac{p_B \cdot (p_A - p_C)}{p_B \cdot p_A} \tag{A.10}$$

where q is 4-momentum transfer. y is calculated in lab frame as follows,

$$y = \frac{p_B \cdot (p_A - p_C)}{p_B \cdot p_A} \tag{A.11}$$

$$= \frac{(E_B, 0) \cdot (E_A - E_C, \vec{p}_A - \vec{p}_C)}{(E_B, 0) \cdot (E_A, \vec{p}_A)} \tag{A.12}$$

$$= \frac{E_B(E_A - E_C)}{E_B E_A} \tag{A.13}$$

$$= \frac{\nu}{E} \tag{A.14}$$

where $\nu = E_\nu - E'_\nu$. E_ν and E'_ν represent initial and final neutrino energies. Thus,

inelasticity represent energy loss fraction of incoming neutrino.

y in CM frame is

$$y = \frac{p_B \cdot (p_A - p_C)}{p_B \cdot p_A} \tag{A.15}$$

$$= \frac{(E, -\vec{p}) \cdot (0, \vec{p} - \vec{p}\,')}{(E, -\vec{p}) \cdot (E, \vec{p})} \tag{A.16}$$

$$= \frac{\vec{p} \cdot \vec{p}\,' - |\vec{p}|^2}{2E^2} \tag{A.17}$$

$$= \frac{\cos \theta^* - 1}{2}. \tag{A.18}$$

From Eqn A.8, A.18, we get

$$t = -sy. \tag{A.19}$$

u in the lab frame is

$$u = (p_\nu - p'_e)^2 \tag{A.20}$$

$$= m_\nu^2 + m_e^2 - 2\vec{p}_\nu \cdot \vec{p}\,'_e \tag{A.21}$$

$$= -2(E_\nu, \vec{p}_\nu) \cdot (E'_e, \vec{p}\,'_e) \tag{A.22}$$

$$= -2(E_\nu E'_e - p_\nu p'_e \cos \theta) \tag{A.23}$$

$$= -2E_\nu E'_e (1 - \cos \theta). \tag{A.24}$$

p_ν is incoming neutrino 4-vector, p'_ν is neutrino 4-vector after collision, p'_e is recoil electron 4-vector.

Because $s + t + u = 0$ and $t = -sy$,

$$s + t = -u \tag{A.25}$$

$$s(1 - y) = 2E_\nu E_e(1 - \cos\theta) \tag{A.26}$$

$$2m_e E_\nu(1 - y) = 2E_\nu E_e'(1 - \cos\theta) \tag{A.27}$$

$$m_e(1 - y) = E_e'(1 - \cos\theta). \tag{A.28}$$

For small θ angle,

$$1 - \cos\theta = 1 - \left(1 - \frac{\theta^2}{2!} + \frac{\theta^4}{4!} - \dots\right) \tag{A.29}$$

$$\approx \frac{\theta^2}{2}. \tag{A.30}$$

Now, we get an expression in a simple form

$$E\theta^2 = 2m_e(1 - y) \tag{A.31}$$

where E is electron energy, θ is the recoil electron angle, m_e the electron rest mass and y inelasticity.

Since $0 < y < 1$,

$$E\theta^2 < 2m_e. \tag{A.32}$$

Appendix B

Geant4 Physics List

B.1 Pre-defined physics list modules

Particle interactions are modeled in Geant4 physics models. Various pre-defined physics lists are available for generic and specific applications. Not all applications need all physics models. For example, if the beam is not polarized, physics model with polarization is not necessary. Some physics models are available for choice between speed and accuracy. Physics models are usually specified for relavant particles. For example, compton scattering (G4ComptonScattering) is only for photon.

MINERvA detector simulation uses following pre-defined physics lists. More details of the physics lists are shown in following sections, if necessary.

- G4Decay

- QStoppingPhysics

- IonPhysics

- G4EmStandardPhysics

- HadronPhysicsQGSP_BERT

- G4HadronElasticPhysics

B.2 G4EmStandardPhysics

- gamma

  - G4PhotoElectricEffect

  - G4ComptonScattering

  - G4GammaConversion

- e^-

  - G4eMultipleScattering

  - G4eIonisation

  - G4eBremsstrahlung

- e^+

  - G4eMultipleScattering

  - G4eIonisation

  - G4eBremsstrahlung

  - G4eplusAnnihilation

- $\mu^\pm$

  - G4MuMultipleScattering (with G4WentzelVIModel)

  - G4MuIonisation

- – G4MuBremsstrahlung

- – G4MuPairProduction

- – G4CoulombScattering

- α, He^3

  - – G4hMultipleScattering

  - – G4ionIonisation

- GenericIon

  - – G4hMultipleScattering

  - – G4ionIonisation

- $\pi^{\pm}, K^{\pm}$, proton

  - – G4hMultipleScattering

  - – G4hIonisation

  - – G4hBremsstrahlung

  - – G4hPairProduction

- $B^{\pm}, D^{\pm}, D_s^{\pm}$, anti-$\text{He}^3$, anti-$\alpha$, anti-deuteron, $\bar{\Lambda}_c^+, \bar{\Omega}^-, \bar{p}, \bar{\Sigma}_c^+, \bar{\Sigma}_c^{++}, \bar{\Sigma}^{\pm}$, anti triton, $\bar{\Xi}_c^+, \bar{\Xi}^-$, deuteron, $\Lambda_c^+, \Omega^-, \Sigma_c^+, \Sigma_c^{++}, \Sigma^{\pm}, \tau^{\pm}$, triton, Ξ_c^-, Ξ^-

  - – G4hMultipleScattering

  - – G4hIonisation

B.3   QStoppingPhysics

- μ^-

  – G4MuonMinusCaptureAtRest

- any other negative charged, short lived particles

  – G4QCaptureAtRest

B.4   IonPhysics

- Deuteron

  – G4LEDeuteronInelastic

  – G4DeuteronInelasticProcess

- Triton

  – G4LETritonInelastic

  – G4TritonInelasticProcess

- Alpha

  – G4LEAlphaInelastic

  – G4AlphaInelasticProcess

B.5   G4HadronElasticPhysics
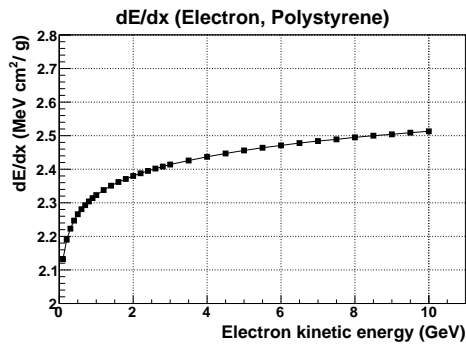
- $\bar{\Lambda}, \bar{n}, \bar{\Omega^-}, \bar{p}, \bar{\Sigma^\pm}, \bar{\Xi^-}, \bar{\Xi^0}, K^\pm, K^0_L, K^0_S, \Lambda, \Omega^-, \pi^\pm, p, \Sigma^\pm, \Xi^-, \alpha,$ deuteron, triton

- G4WHadronElasticProcess (with following cross-section models)

    * p: G4CHIPSElasticXS

    * $\pi^{\pm}$: G4BGGPionElasticXS

    * any others: G4VHadronElastic

- neutron

    - G4WHadronElasticProcess with cross-section model: G4CHIPSElasticXS
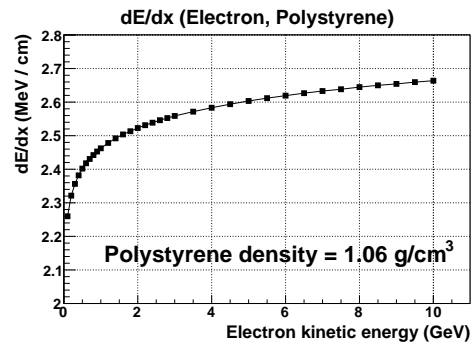
Appendix C

Electron dE/dx

Fig. C.1 shows electron dE/dx (only by collison) in polystyrene. The data is taken from [?] and `physics.nist.gov/PhysRefData/Star/Text/contents.html`.

Figure C.1: Electron dE/dx in polystyrene (a) dE/dx (density normalized), (b) dE/dx in actual scintillator density

Appendix D

Vertex Stability

Vertex distribution of pre-selection is plotted. If there is unusual noise or dead channels like a group of 8 channels for a period of time, the vertex module distribution will suddenly change.

Figure D.1: Vertex stability plots of pre-selection sample (mod25-32)

Figure D.2: Vertex stability plots of pre-selection sample (mod33-56)
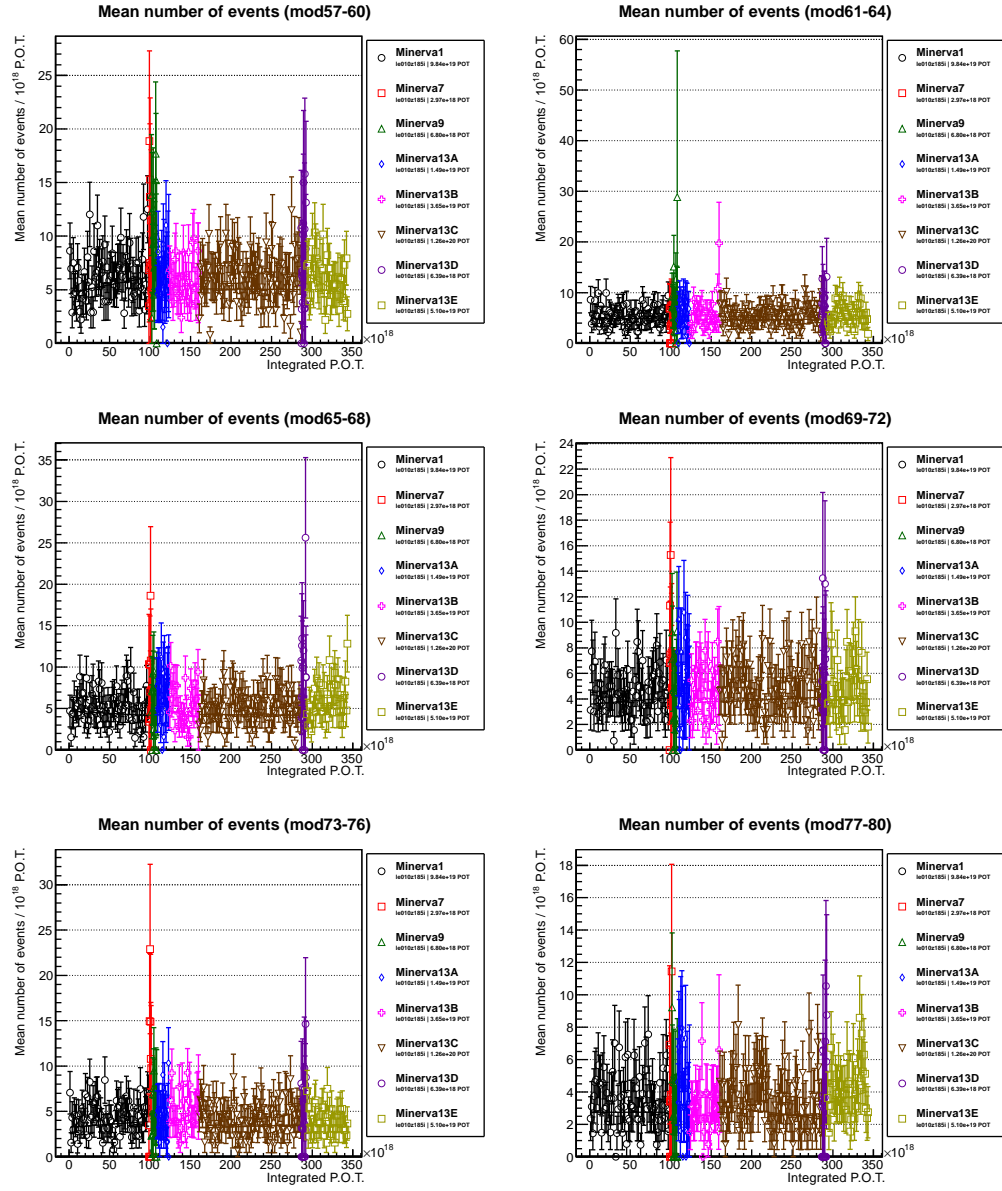
Figure D.3: Vertex stability plots of pre-selection sample (mod57-80)

Appendix E

GENIE Reweightable Uncertainties

Summary of GENIE reweightable uncertainties is taken from [**?**]. "Calc" column indicates if it is calculated in MINERvA analysis (as part of GENIEWeightAssembler process).

Table 1.1: Cross section model uncertainties

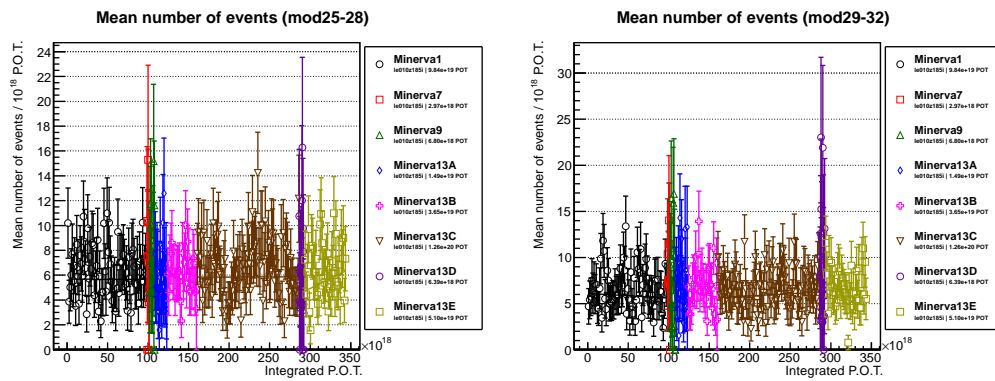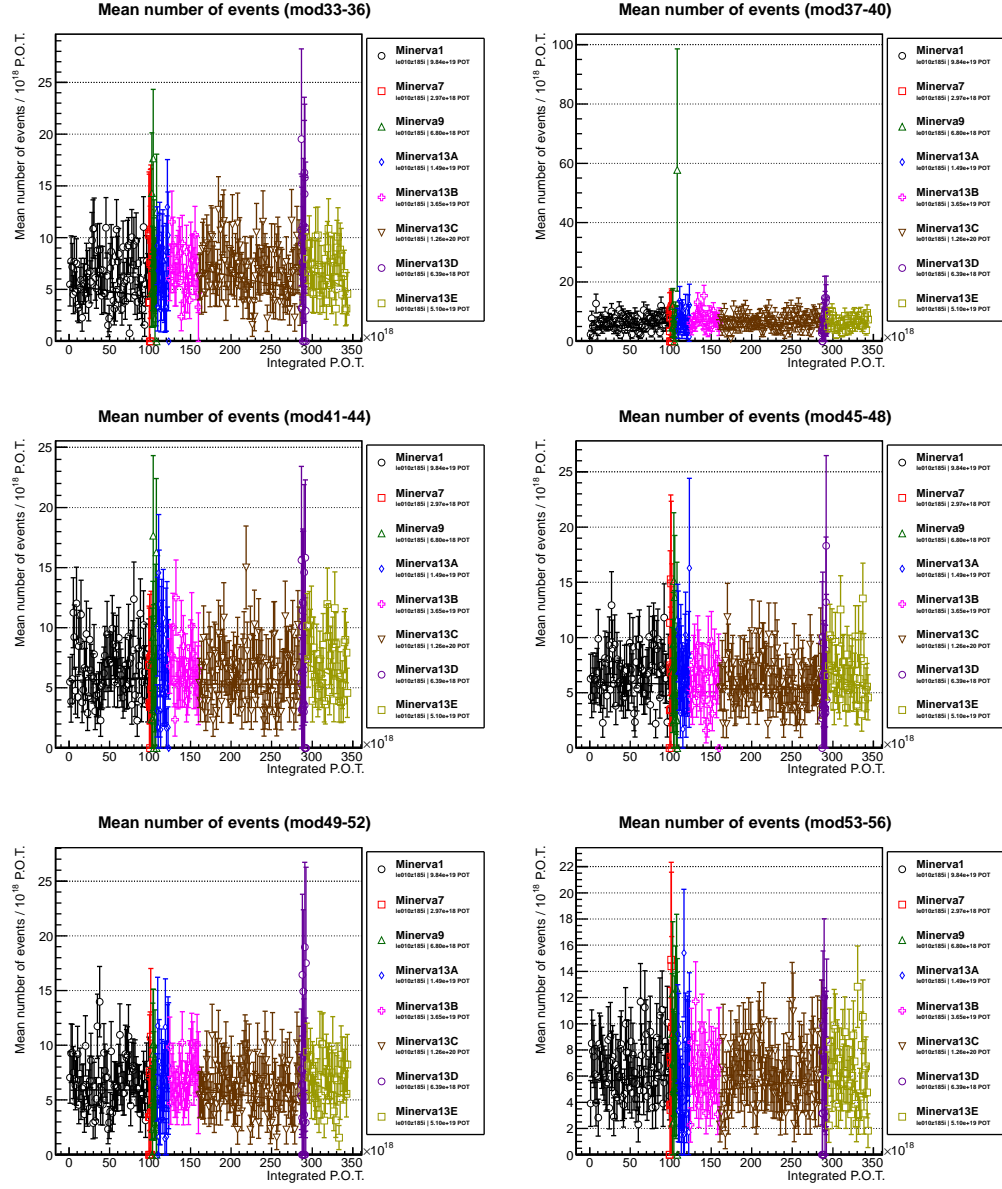| Uncertainty	GENIE knob name	Description	1 σ	Reference	Calc	Notes
M_A (Elastic Scattering)	MaNCEL	Adjusts M_A in elastic scattering cross section.	$\pm 25\%$	Estimated in T2K studies?	•	
Eta (Elastic scattering)	EtaNCEL	Adjusts eta in elastic scattering cross section.	$\pm 30\%$	Estimated in T2K studies?	•	
M_A (CCQE Scattering)	MaCCQE	Adjusts M_A in Llewellyn-Smith cross section, affecting shape and normalization.	$+25\%$ -15%	[?] Updated in T2K studies – now asymmetric.	•	
CCQE Normalization	NormCCQE	Adjusts CCQE Normalization	$+20\%$ -15%	Estimated in T2K studies?	•	
CCQE Normalization (maintaining energy dependence)	NormCCQEenu	Adjusts CCQE Normalization (maintains energy dependence)				
M_A (CCQE Scattering, shape only)	MaCCQEshape	Adjusts M_A in Llewellyn-Smith cross section, affecting shape only.	$\pm 10\%$	Estimated in T2K studies?	•	
CCQE Vector Form factor model	VecFFCCQEshape	Changes from BBBA to dipole, affecting shape only			•	
CC Resonance Normalization	NormCCRES	Changes the normalization of CC Rein-Sehgal cross section.	$\pm 20\%$	Estimated in T2K studies?	•	
NC Resonance Normalization	NormNCRES	Changes the normalization of NC Rein-Sehgal cross section.	$\pm 20\%$	Estimated in T2K studies?	•	
M_A – shape only (CC Resonance Production)	MaCCRESshape	Adjusts M_A in Rein-Sehgal CC cross section, affecting shape only.	$\pm 10\%$	Estimated in T2K studies?	•	
M_V – shape only (CC Resonance Production)	MvCCRESshape	Adjusts M_V in Rein-Sehgal CC cross section, affecting shape only.	$\pm 5\%$	Estimated in T2K studies?	•	

Uncertainty	GENIE knob name	Description	1 σ	Reference	Calc	Notes
M_A – shape only (NC Resonance Production)	MaNCRESshape	Adjusts M_A in Rein-Sehgal NC cross section, affecting shape only.	$\pm$ 10%	Estimated in T2K studies?	•	
M_V – shape only (NC Resonance Production)	MvNCRESshape	Adjusts M_V in Rein-Sehgal NC cross section, affecting shape only.	$\pm$ 5%	Estimated in T2K studies?	•	
M_A (Resonance Production)	MaRES	Adjusts M_A in Rein-Sehgal cross section, affecting shape and normalization.	$\pm$ 20%	[?]	•	GENIE has separate knobs for resonance CC (MaCCRES) and NC (MaNCRES), which we gang together
M_V (Resonance Production)	MvRES	Adjusts M_V in Rein-Sehgal cross section, affecting shape and normalization.	$\pm$ 10%	Estimated in T2K studies?	•	GENIE has separate knobs for resonance CC (MvCCRES) and NC (MvNCRES), which we gang together.
1π production from $\nu p/\bar{\nu} n$ non-resonant interactions	Rvp1pi	Affects NC and CC production of single pion final states from non-resonant inelastic (i.e. Bodek-Yang) scattering. $\nu p/\bar{\nu} n$ initial states.	$\pm$ 50%	[?], updated in T2K studies.	•	GENIE has separate knobs for resonance np and nubar-n which we gang together (isospin symmetry). Also gang together NC and CC channels. Value must be positive.

Uncertainty	GENIE knob name	Description	1 σ	Reference	Calc	Notes
1π production from $\nu n/\bar{\nu}p$ non-resonant interactions	Rvn1pi	Affects NC and CC production of single pion final states from non-resonant inelastic (i.e. Bodek-Yang) scattering. $\nu n/\bar{\nu}p$ initial states.	$\pm 50\%$	[?], updated in T2K studies.	•	GENIE has separate knobs for resonance nun and nubar-p which we gang together (isospin symmetry). Also gang together NC and CC channels. Value must be positive.
2π production from $\nu p/\bar{\nu}n$ non-resonant interactions	Rvp1pi	Affects NC and CC production of single pion final states from non-resonant inelastic (i.e. Bodek-Yang) scattering. $\nu p/\bar{\nu}n$ initial states.	$\pm 50\%$	[?], updated in T2K studies.	•	GENIE has separate knobs for resonance np and nubar-n which we gang together (isospin symmetry). Also gang together NC and CC channels. Value must be positive.
2π production from $\nu n/\bar{\nu}p$ non-resonant interactions	Rvn1pi	Affects NC and CC production of single pion final states from non-resonant inelastic (i.e. Bodek-Yang) scattering. $\nu n/\bar{\nu}p$ initial states.	$\pm 50\%$	[?], updated in T2K studies.	•	GENIE has separate knobs for resonance nun and nubar-p which we gang together (isospin symmetry). Also gang together NC and CC channels. Value must be positive.

Uncertainty	GENIE knob name	Description	1 σ	Reference	Calc	Notes
Bodek-Yang parameter A_{HT}	AhtBY	tweak the Bodek-Yang model parameter A_{ht} - incl. both shape and normalization effect	$\pm$ 25%			
Bodek-Yang parameter B_{HT}	BhtBY	tweak the Bodek-Yang model parameter B_{ht} - incl. both shape and normalization effect	$\pm$ 25%			
Bodek-Yang parameter C_{V1u}	CV1uBY	tweak the Bodek-Yang model parameter C_{V1u} - incl. both shape and normalization effect	$\pm$ 30%			
Bodek-Yang parameter C_{V2u}	CV2uBY	tweak the Bodek-Yang model parameter C_{V2u} - incl. both shape and normalization effect	$\pm$ 40%			
Bodek-Yang parameter A_{HT} – shape only	AhtBYshape	tweak the Bodek-Yang model parameter A_{ht} - shape only effect to d2sigma(DIS)/dxdy	$\pm$ 25%			
Bodek-Yang parameter B_{HT} – shape only	BhtBYshape	tweak the Bodek-Yang model parameter B_{ht} - shape only effect to d2sigma(DIS)/dxdy	$\pm$ 25%			
Bodek-Yang parameter C_{V1u} – shape only	CV1uBYshape	tweak the Bodek-Yang model parameter C_{V1u} - shape only effect to d2sigma(DIS)/dxdy	$\pm$ 30%			
Bodek-Yang parameter C_{V2u} – shape only	CV2uBYshape	tweak the Bodek-Yang model parameter C_{V2u} - shape only effect to d2sigma(DIS)/dxdy	$\pm$ 40%			
Nu/Nubar CC cross section ration	RnubarnuCC	Change the neutrino/antineutrino CC cross section ratio (r).	??	[?]		Defaults not defined? Not working in GENIE.
DIS CC Normalization	NormDISCC	Adjusts the overall normalization of the nonresonance inclusive cross section.	??	[?]		n/a Not working in GENIE

Uncertainty	GENIE knob name	Description	1 σ	Reference	Calc	Notes
Coherent model M_A	MaCOHpi	Adjusts M_A in the Rein-Sehgal Coherent model	$\pm$ 40%	Unknown		
Coherent model R_0	R0COHpi	Adjusts R_0 in the Rein-Sehgal Coherent model	$\pm$ 10%	unknown		
Nuclear modifications to DIS	DISNuclMod	Turn on/off nuclear modifications to parton distributions	On/off	n/a		A switch, not a knob.
Modfiy Pauli blocking (CCQE) at low Q^2	CCQEPauliSup-ViaKF	Adjusts Pauli blocking momentum cutoff.	$\pm$ 30%	Unknown	$\bullet$	
Fermi gas $\rightarrow$ spectral function	CCQEMomDistro-FGtoSF	Reweights incoming nucleon momentum distribution from Fermi Gas (Bodek-Ritchie) to a spectral function	On/off	n/a		A switch, not a knob.

Table 1.2: Hadronic system uncertainties

Uncertainty	GENIE knob name	Description	1 σ	Reference	Calc	Notes
Pion mean free path	MFP_pi	tweak mean free path for pions	± 20%	[?]	●	
Nucleon mean free path	MFP_N	tweak mean free path for nucleons	± 20%	[?]	●	100% correlated with nucleon elastic fates cross section
Pion fates – absorption	FrAbs_pi	tweak absorption probability for pions, for given total rescattering probability	± 30%	[?]	●	
Pion fates – charge exchange	FrCEx_pi	tweak charge exchange probability for pions, for given total rescattering probability	± 50%	[?]	●	
Pion fates – Elastic	FrElas_pi	tweak elastic probability for pions, for given total rescattering probability	± 10%	[?]	●	
Pion fates – Inelastic	FrInel_pi	tweak inelastic probability for pions, for given total rescattering probability	± 40%	[?]	●	
Pion fates – pion production	FrPiProd_pi	tweak pion production probability for pions, for given total rescattering probability	± 20%	[?]	●	
Nucleon fates – charge exchange	FrCEx_N	tweak charge exchange probability for nucleons, for given total rescattering probability	± 50%	[?]	●	
Nucleon fates – Elastic	FrElas_N	tweak elastic probability for nucleons, for given total rescattering probability	± 30%	[?]	●	100% correlated with nucleon mean free path

Uncertainty	GENIE knob name	Description	1 σ	Reference	Calc	Notes
Nucleon fates – Inelastic	FrInel_N	tweak inelastic probability for nucleons, for given total rescattering probability	$\pm 40\%$	[?]	•	
Nucleon fates – absorption	FrAbs_N	tweak absorption probability for nucleons, for given total rescattering probability	$\pm 20\%$	[?]	•	
Nucleon fates – pion production	FrPiProd_N	tweak pion production probability for nucleons, for given total rescattering probability	$\pm 20\%$	[?]	•	
AGKY hadronization model – x_F distribution	AGKYxF1pi	tweak xF distribution for low multiplicity (N + pi) DIS f/s produced by AGKY	$\pm 20\%$	[?]		
AGKY hadronization model –pion p_T distribution	AGKYpT1pi	tweak pT distribution for low multiplicity (N + pi) DIS f/s produced by AGKY	$\pm 3\%$	[?]		
Formation Zone	FormZone	Change formation length in formation zone model.	$\pm 50\%$	SKAT estimate		Did not seem to be working in earlier versions of GENIE.
Delta decay angular distribution	Theta_Delta2Npi	Change delta decay angular distribution	On/off	n/a	•	Reweight to more correct angular distribution (i.e. not isotropic).
Resonance decay branching ratio to photon	RDecBR1gamma	tweak Resonance → X + gamma branching ratio, eg Delta+(1232) → p gamma	$\pm 50\%$	Unknown	•	
Resonance decay branching ratio to eta	RDecBR1eta	tweak Resonance → X + eta branching ratio, eg N+(1440) → p eta	$\pm 50\%$	Unknown	•	

Appendix F

Planned Changes Before Publication

Several additional studies were done after the completion of this thesis, and these will be included in the publication based on the results of this thesis. None of these constitute major changes in the analysis method but they will improve the precision and reliability of the result. The studies include accounting for uncertainties in event reconstruction, including uncertainties in reconstruction efficiency, improving the rejection of muon induced events, accounting for biases in the angle and energy and the uncertainty in the energy resolution. An update to the sideband constraint method to the background will improve the reliability of the background prediction in the presence of multi-nucleon effects in ν_e CCQE, one of the main backgrounds.

Efficiency of event reconstruction in the real detector may be slightly lower than the efficiency in simulated events due to effects not implemented in the simulation. Muons positively identified in the MINOS near detector can be used to study this efficiency deficit in the MINERvA reconstruction of muons, but there is no anal-

ogous study that can be performed with electrons. The seeding of the electron reconstruction from tracks uses the same algorithm as the muon reconstruction, so it is plausible that a similar efficiency deficit applies to the electron reconstruction. However, a second seeding algorithm based on "blobs" is used as well, so this deficit may not be present. We take the entire size of the deficit correction in the track reconstruction as a systematic uncertainty.

After completion of this thesis, event scans located a small amount of muon induced background. These can be easily removed using an additional event selection. Since neutrino interactions from upstream of the detector, that cause the muon induced background, are not simulated, and therefore the data and simulated prediction will have a small difference unless the muon induced background is removed.

Electron energy reconstruction was characterized using comparisons of the Michel electron energy spectrum discussed in Section 2.3.8. Differences between the simulated spectrum and that found in data are used as measures of the systematic uncertainties in energy reconstruction.

Angle reconstruction can have a bias if the neutrino beam and the detector are not perfectly aligned, which is possible given the way the detector is internally aligned using straight tracks of particles. This is studied by using a selection of muon neutrino induced events with low measured recoil energy which should be strongly forward peaked. A small, few millirad, bias was found and corrected which is noticeable in the $E\theta^2$ variable.

The multi-nucleon effects in charged current quasi-elastic scattering are expected to distort the shape of $d\sigma/dQ^2$, cross-section function of momentum transfer squared. This effect has been measured by MINERvA in muon neutrinos [**?**, **?**], but it should

equally well effect that background events from ν_e CCQE distorts the shape of $d\sigma/dQ^2$. The effect fundamentally occurs because the sideband tuning uses relatively high Q^2 events to constrain the background, whereas the events that are background are very low Q^2. The sideband tuning for the background prediction will be modified to use only a smaller $E\theta^2$ region, which also implies lower Q^2, to mitigate the effect in the tuning. When the sideband region is restricted to smaller $E\theta^2$, sideband 4 will be omitted. The sideband 4 was defined from region mostly near smaller $E\theta^2$ to have coherent π^0 event rich sample, but the constraining power on coherent π^0 background from the tuning was not strong and this background is very small in the final sample.